OPERATIONAL MODAL ANALYSIS APPLIED TO CENTRIFUGAL COMPRESSORS

Leandro de Oliveira Zague

Dissertação de Mestrado apresentada ao Programa de Pós-graduação em Engenharia Mecânica, COPPE, da Universidade Federal do Rio de Janeiro, como parte dos requisitos necessários à obtenção do título de Mestre em Engenharia Mecânica.

Orientador: Daniel Alves Castello

Rio de Janeiro
Março de 2019

OPERATIONAL MODAL ANALYSIS APPLIED TO CENTRIFUGAL COMPRESSORS

Leandro de Oliveira Zague

DISSERTAÇÃO SUBMETIDA AO CORPO DOCENTE DO INSTITUTO ALBERTO LUIZ COIMBRA DE PÓS-GRADUAÇÃO E PESQUISA DE ENGENHARIA (COPPE) DA UNIVERSIDADE FEDERAL DO RIO DE JANEIRO COMO PARTE DOS REQUISITOS NECESSÁRIOS PARA A OBTENÇÃO DO GRAU DE MESTRE EM CIÊNCIAS EM ENGENHARIA MECÂNICA.

Examinada por:

Prof. Daniel Alves Castello, D.Sc.

Prof. Thiago Gamboa Ritto, D.Sc.

Prof. Carlos Frederico Trotta Matt, D.Sc.

RIO DE JANEIRO, RJ – BRASIL
MARÇO DE 2019

Zague, Leandro de Oliveira

Operational Modal Analysis Applied to Centrifugal Compressors/Leandro de Oliveira Zague. – Rio de Janeiro: UFRJ/COPPE, 2019.

XXV, 118 p.: il .; 29, 7cm.

Orientador: Daniel Alves Castello

Dissertação (mestrado) – UFRJ/COPPE/Programa de Engenharia Mecânica, 2019.

Bibliografia: p. 97 – 102.

1. Operational Modal Analysis. 2. Rotordynamics. 3. Stability Measurement. I. Castello, Daniel Alves. II. Universidade Federal do Rio de Janeiro, COPPE, Programa de Engenharia Mecânica. III. Título.

Agradecimentos

Acredito que o que somos é o resultado de características com as quais nascemos, combinadas com características que moldamos ou adquirimos através de aprendizado contínuo ao longo da caminhada da vida.

Assim, é inevitável que tenhamos em nosso ser, um pouco de cada pessoa que fez, faz ou fará parte de nossa vida.

Nesse sentido, os agradecimentos que aqui faço, são para os meus familiares, amigos de infância, de faculdade, de trabalho, professores e para minha companheira de jornada.

Gostaria de agradecer a meus pais Lucy Ap. de Oliveira Zague e Silvano Zague, por todo o carinho, amor, incentivo e por me ensinarem desde novo que devemos perseguir nossos sonhos, não importa quão grande ou improváveis eles pareçam ser. Agradeço por me ensinaram que na busca dos sonhos devemos ter como pilares a honestidade, perseverança e foco.

Agradeço a meu irmão Joel Zague pelo companheirismo e cumplicidade de sempre, pela grande amizade que vai além dos laços sanguíneos, nos fazendo também irmão de vida, mesmo com personalidades tão distintas.

Agradeço a minha sobrinha Luiza Fornazieri Zague, por tornar a minha vida e a de toda minha família ainda melhor. Por trazer esperança de que o trabalho e busca por conhecimento será continuado com maestria por uma nova geração que já nasce com fome pelo saber.

Agradeço a meus avós Ludgero de Oliveira, Leonor Literoni de Oliveira, Amadeu Zague e Élcia Gonçalves Zague por sua presença, exemplo e lembranças maravilhosas que me proporcionam do aconchego de estar com os avós, na época maravilhosa e despreocupada da minha infância.

Gostaria de agradecer aos amigos da minha cidade natal, que mesmo em diferentes lugares do país e com encontros esporádicos, não deixam os laços de amizade enfraquecer, mantendo a liberdade que temos entre nós. Em especial cito os amigos Daniel Piquê, Raphael Funchal, Thales Rangel, Diego Raone, Samuel Godinho, João Pedro Ozelim, Maria Betânia Lemos, Gleicy Oliveira Fidelis, Stella Colombaroli e Brenda Furtado.

Aos meus amigos do DAGEMP da UFU, agradeço pelo período excelente de nos-

sas vidas que passamos juntos e pela receptividade com a qual me acolheram. Não apenas aprendi o meu ofício ao lado de vocês, mas os tive como uma família adotiva no período em que vivi em Uberlândia. Encontrar alguns de vocês anualmente é sempre um prazer. Agradeço em especial ao Anderson Fagundes, Marcus Vinicius Queiroz, Gustavo Tressia, Bruno Guimarães, Pedro Oscar Mundim, Horlandi Violatti e Flávio Rosa.

Gostaria de agradecer aos amigos de Aerodesign, pelas noites acordados trabalhando, pelo desafio que enfrentamos juntos durante 3 anos, pelo aprendizado concentrado e profundo que carrego até hoje e que me tornou um engenheiro melhor, por me ensinarem o que é uma equipe e onde podemos chegar com uma boa equipe! Em especial agradeço a 3 irmãos que fiz no aero: Cássio Azevedo, Lucas Dias Lana e Raphael Platini.

Agradeço a meus professores do fundamental ao ensino médio, pela base que me deram, aos meus professores da UFU e da UFRJ, por passarem o conhecimento e as ferramentas para o exercício da minha profissão e para a caminhada independete, na busca contínua por conhecimento. Agradeço em especial ao meu orientador Daniel Castello, por seu exemplo e conduta como professor e pela importante bagagem de conhecimento transferida durante o mestrado, que vai desde Álgebra Linear, até Dinâmica de Estruturas e Identificação de Sistemas.

Agradeço a meus amigos do curso de formação da Petrobras, que fizeram os meus dias no Rio de Janeiro melhores durante e após a jornada do curso de formação, em especial ao Edson Valverde, Felipe Kich, Guilherme Dias e João Godoy.

Agradeço aos meus amigos de trabalho na Petrobras. Tenho orgulho de ter sido parte do time de equipamentos rotativos e de ter trabalhado em projetos desafiadores do Pré-Sal. Agradeço aos colegas de trabalho com quem tive a oportunidade de trabalhar e que sempre fizeram do ambiente de trabalho um lugar leve, alegre, sadio e prazeroso, em especial Rodrigo Paz, Matheus Vieira, Francisco Carlos Monteiro, Edmar Barbosa e Thiago Margoni.

Aos amigos André Varella, Leonardo Ishimoto, Raphael Timbó, Diogo Ujihara e Letícia Tapajoz, agradeço pelo companheirismo e pelos ensinamentos em turbomáquinas. Agradeço ainda aos professores da Petrobras Paulo Sérgio, Antônio Felipe Flutt e José Augusto Matias, por sempre estarem prontos a ensinar e o fazer com prazer, tendo contribuído bastante no meu aprendizado.

Agradeço à Petrobras por ter investido em minha capacitação durante todo o período que estive na empresa.

Agradeço ao amigo Marcelo Accorsi, por ter sido meu tutor durante o tempo de Petrobras e por ser hoje um parceiro e amigo em uma nova e desafiadora jornada. Agradeço ainda aos meus parceiros e amigos de trabalho atuais Plinio Porciuncula, Sterling Schmutz, Jean Abdo-Berndt e Daniela Caroline.

Agradeço novamente ao Leonardo Ishimoto, desta vez em relação a coleta de dados de vibração de um compressor de reciclo de hidrogênio analisado no presente trabalho e aos doutores Hunter Cloud e José Vázquez por sua sua valiosa contribuição no processamento desses dados.

Por fim, agradeço a minha companheira de vida Nayara Mariano, pelo amor e carinho, paciência, incentivo, compreensão e tranquilidade, especialmente no período do mestrado. Agradeço pela alegria que trouxe e trás a cada dia para minha vida.

Resumo da Dissertação apresentada à COPPE/UFRJ como parte dos requisitos necessários para a obtenção do grau de Mestre em Ciências (M.Sc.)

ANÁLISE MODAL OPERACIONAL APLICADA A COMPRESSORES CENTRÍFUGOS

Leandro de Oliveira Zague

Março/2019

Orientador: Daniel Alves Castello

Programa: Engenharia Mecânica

Dadas as incertezas associadas a análise de estabilidade através de modelagem rotodinâmica, um número crescente de operadores tem especificado testes de verificação de estabilidade para validar o modelo rotodinâmico e reduzir os riscos de instabilidade rotodinâmica durante operação, além de riscos de velocidades críticas com pouco amortecimento dentro da faixa de operação, em carga parcial ou plena. O presente trabalho examina métodos de Análise Modal Operacional aplicados a compressores centrífugos, como alternativa aos métodos utilizados em testes convencionais de estabilidade. Cinco métodos de análise modal serão avaliados através de sua aplicação a modelos de diferente complexidade, examinando a influência da taxa de amostragem, duração da aquisição de sinais, relação sinal ruído, processamento de sinais e parâmetros dos modelos de identificação utilizados para análise modal.

Abstract of Dissertation presented to COPPE/UFRJ as a partial fulfillment of the requirements for the degree of Master of Science (M.Sc.)

OPERATIONAL MODAL ANALYSIS APPLIED TO CENTRIFUGAL COMPRESSORS

Leandro de Oliveira Zague

March/2019

Advisor: Daniel Alves Castello

Department: Mechanical Engineering

Given the predictive uncertainties associated with rotor stability, more and more end-users are requiring stability verification tests to validate the rotordynamic models to reduce the risk of rotor instability issues during operation, as well as the risk of critical speeds with low damping inside the operational speed range at full or partial load conditions. The present work examines Operational Modal Analysis methods applied to centrifugal compressors, as an alternative to the methods applied to conventional stability tests. Five OMA methods will be evaluated through its application to models of different complexity, examining the influence of sampling rate, acquisition time span, signal to noise ratio, signal processing and identification model parameters in the modal analysis.

Contents

List of Figures

List of Tables

List of Symbols

C	Damping, p. 105
$D(s)$	Denominator, p. 108
E	Expected value, p. 12
G	Gyroscopic Effect, p. 105
$N(s)$	Numerator, p. 108
U_{Φ_r}	r-th modal force, p. 13
$\Delta \underline{u}$	Small increment of input's vector at the proximity of operational point, p. 111
$\boldsymbol{A}$	State matrix, p. 111
$\boldsymbol{B}$	Input matrix, p. 111
$\boldsymbol{G}$	Spectral density matrix, p. 12
$\boldsymbol{H}$	Impulse response function matrix, p. 12
$\boldsymbol{K}$	Stiffness, p. 103
$\boldsymbol{M}$	Mass, p. 103
$\boldsymbol{R}_y$	Outputs correlation matrix, p. 12
$\boldsymbol{R}_u$	Correlation matrix between inputs , p. 12
$\boldsymbol{R}_{yu}$	Cross correlation matrix between outputs and inputs, p. 12
$\mathbb{C}$	Observation Matrix, p. 16
$\tilde{\boldsymbol{H}}(i\boldsymbol{\Omega})$	Frequency response function matrix, p. 12
$\tilde{\boldsymbol{H}}(s)$	Transfer Function Matrix, p. 108
$\delta(t)$	Dirac' Delta, p. 109

γ	Kurtosis, p. 70
λ	State space eingenvalues, p. 113
$\mathbb{C}_a$	Acceleration observation matrix, p. 112
$\mathbb{C}_d$	Displacement observation matrix, p. 112
$\mathbb{C}_v$	Velocity observation matrix, p. 112
σ	singular values, p. 34
$\sigma^2_{u_n}$	Variance of input n, p. 13
τ	Time lag, p. 12
$\underset{\sim}{X}_r$	r-th state space eigenvector, p. 13
$\underset{\sim}{\Phi}_r$	r-th modeshape, p. 13
$\underset{\sim}{X}$	State space eingenvectors, p. 113
$\tilde{\underset{\sim}{U}}(s)$	System inputs vector in Laplace Domain, p. 108
$\tilde{\underset{\sim}{Y}}(s)$	System outputs vector in Laplace Domain, p. 108
$\underset{\sim}{\varepsilon}$	Small increment of state's vector at the proximity of operational point, p. 111
$\underset{\sim}{u}$	System inputs vector, p. 12
$\underset{\sim}{u}_{op}$	Input's vector at operational point, p. 111
$\underset{\sim}{x}$	State's vector, p. 111
$\underset{\sim}{x}_{op}$	State's vector at operational point, p. 111
$\underset{\sim}{y}$	System outputs vector, p. 12
h_r	r-th modal impulse response, p. 13
p	Pole, p. 108
q_r	r-th modal coordinate, p. 13
u	system input, p. 105
w_d	Damped natural frequency, p. 26
w_n	Natural frequency, p. 26

xi	Damping ratio, p. 26
z	Zero, p. 108
B	Inputs spectral bandwidth, p. 13

Abbreviations

4SID	Subspace state-space system identification, p. 7
AF	Amplification Factor, p. 8
CFD	Computational Fluid Dynamics, p. 104
CVA	Canonical Variate Analysis, p. 8
DE	Drive End, p. 3
EMA	Experimental Modal Analysis, p. 3, 4
ERA	Eigenystem Realization Algorithm, p. 16
FEM	Finite Element Model, p. 103
FRF	Frequency Response Function, p. 8, 110
HC	Hydrocarbons, p. 87
IRF	Impulse Response Function, p. 109
IRF	Impulse Response Functions, p. 9
MDOF	Multiple Degrees of Freedom, p. 9
MIMO	Multiple Inputs Multiple Outputs, p. 9
MOBAR	Multiple Output Backward Autoregressive, p. 7
NDE	Non Drive End, p. 3
OEM	Original Equipment Manufacturer, p. 1, 2
OMA	Operational Modal Analysis, p. 3, 4
PC	Principal Component, p. 8
PEM	Prediction Error Methods, p. 9

PSD	Power Spectral Densities, p. 14
SDOF	Single Degree of Freedom, p. 8
SIMO	Single Input Multiple Outputs, p. 9
SNR	Signal to Noise Ratio, p. 4
SSI	Stochastic Subspace Identification, p. 7, 18
SVD	Singular Value Decomposition, p. 8
UPC	Unweighted Principal Components, p. 8
Vx	Vibration in x direction, p. 105
Vy	Vibration in y direction, p. 105

Chapter 1

Introduction

This chapter presents the motivation of the present work, the dissertation goals and the dissertation outline.

1.1 Motivation

Process centrifugal compressors are a class of fluid machinery aimed at transport a certain amount of gas from a lower pressure to a higher pressure, being important elements for industries as oil and gas (upstream, midstream and downstream), chemical, petrochemical, fertilizer production, among others.

They are well known for their high reliability, being able to work in the range of mid to high mass flows with a wide range of pressures, achieving the needs of many applications of process industry.

These machines are tailor made, designed specifically to work with the process parameters of the plant where they are inserted, as: gas composition, mass flow, suction temperature and pressure and discharge pressure.

Usually a more agressive aero-thermodynamic design leads to a less robust rotordynamic behavior while a robust rotordynamic behavior leads to a lower thermodynamic performance. Thus, the design of a centrifugal compressor must be a compromise between aero-thermodynamic and rotordynamic goals.

Recently, applications such as reinjection of natural gas and carbon dioxide for the oil and gas upstream market, urea production and carbon capture and sequestration, are pushing centrifugal compressors Original Equipment Manufacturer (OEM) to the edge of their experience regarding the operation with working fluids of ultra-high densities.

The offshore platforms of Brazilian Pre-Salt are examples of such applications, requiring from reinjection compressors to work with discharge pressures up to 550 barA, and possibly higher pressure in the next projects.

Moreover, the OEMs are adopting more aggressive rotordynamic designs, following the downsizing philosophy, leading to thinner rotors and higher speeds. These attributes demand accurate rotordynamic models, aiming to achieve the following project goals:

- to guarantee adequate separation margin between operational speed range and natural frequencies of system;
- to verify the compatibility between vibration levels and internal clearance, to avoid rubbing and high tensions;
- to verify the rotordynamic sensitivity to unbalance;
- to verify the compressor stability in several operation conditions;

API 617 [4] requires three steps, as part of Lateral Rotordynamic Analysis, aiming to show that the project rotordynamic goals were achieved, being: Undamped Critical Speed Analysis, Unbalance Response Analysis and Stability Analysis. Appendix A shows a general description of Lateral Analysis, explaining each of these steps to the interested reader.

Between the project goals and analysis steps, stability assessment has a special place. This is due to the fact that rotor instability is an undesirable condition of operation in which various elements in the rotor system induce self-excited vibration that can cause severe failures, threatening personal and environment (CLOUD [5]).

Rotor stability is negatively affected by the increasing densities, speeds and thiner rotors resulting from the recent applications and downsizing design philosophy, and despite the fact that several advances are being reached in the rotordynamic modeling, there are still uncertainties on rotordynamic parameters of bearing, labyrinth seals, damper seals, oil seals (when applied), besides impellers aerodynamic cross coupling as shown by KOCUR *et al.* [6].

Therefore, performing stability tests to validate the models are being more and more required by end-users as a way to reduce risk of stability issues during operation, as well as the risk of critical speeds with low damping inside operational speed range in full or partial load conditions. It is unpractical to test all the possible operational scenarios, but a model validation/reconciliation increases the possibility of success, once these scenarios were evaluated in the stability analysis performed with the model.

Stability tests are mostly done just during shop acceptance tests in machines that have failed to meet the Level-I stability criteria, established by API 617 [4] and have presented low level of damping predicted by the detailed stability investigation carried in accordance with API 617 [4] Level-II stability analysis.

Nowadays, mostly stability testing in centrifugal compressors uses Experimental Modal Analysis (EMA) techniques. These tests generally require the assembling (temporarily) of an electromagnetic shaker on the non-drive end (NDE) of machine, through bolted extensions or tapered sleeve, to apply nonsynchronous excitation to the rotor, while the compressor is running at a pre-defined speed and operational condition at the OEM's test bench. Therefore, the project of the system should be done taking into account the need for the specific position where the shaker will be attached at. In this concern, the shaft and the end of the rotor needs to be modified in order to have sufficient space for the magnetic exciter. An additional limitation in the use of traditional stability test is the case of passing through machines, where the exciter can not be easily installed (GUGLIELMO *et al.* [7]).

It is important to minimize the influence of the shaker device on the rotordynamics of compressor and also in balance state. Furthermore, the power of the shaker and its operational frequency bandwidth should be able to excite the models of interest during machine operations.

A common issue is the addition of unbalance due to machining perpendicularity and misalignment, even inside tight tolerances, at interface between exciter rotating part and shaft end.

Thus, experimental assessment of turbomachinery stability by traditional methods is also a challenge. An alternative to the traditional EMA tests, that is the focus of the present work, is to adopt Operational Modal Analysis (OMA) methods.

OMA methods does not require the acknowledgment of excitation applied to a structural system, in order to allow the modal parameters extraction nor application of external excitation. Thus it eliminates the need of assembling an excitation device, making stability test a simpler task and allowing the extraction of modal parameters of an equipment during its field operation.

1.2 Dissertation Goals

The goals of this dissertation are to analyze OMA methods applied to centrifugal compressors, highlighting aspects of OMA that are specific to rotating machines. In particular, one is interested in signal processing, parameter setting, elimination of computational and excitation modes and finally the modal parameters extraction in each of analyzed methods.

This will be performed by applying OMA to models of different complexity, starting with a simple mass-spring-damper model (with three elements) and evolving to a complete rotordynamic Finite Element Model (FEM), allowing uncertainties quantification analysis through Monte Carlo simulation, considering different levels of damping, excitation and Signal to Noise Ratio (SNR) and its influence in the

modal parameters extraction.

A real application of OMA to a centrifugal compressor during field operation will be performed also, showing the necessary steps of signal processing needed prior to OMA analysis.

1.3 Dissertation Outline

At Chapter 2, a brief overview of OMA will be given, aiming to familiarize some readers from turbomachinery engineering community with the subject. The main focus of this chapter is to present a State of Art Literature Review with focus in traditional Modal Testing and OMA applied to centrifugal compressors, discussing the advances achieved in the last years in this field.

Chapter 3 presents the theoretical fundamentals of time domain OMA methods studied in this work. The interested reader will find basic concepts, necessary for understanding this chapter at Appendix B. The main focus of Chapter 3 is not to discuss in depth each of the methods, once the algorithms studied here are available at the literature, but to present the concepts of Stochastic Vibration and the bridge between traditional modal analysis and OMA methods.

At Chapter 4, the physical systems adopted to study time domain OMA methods and its application to centrifugal compressors will be presented, including computational models of systems and a real installation of a hydrogen recycle compressor, operating in a Brazilian refinery.

Results and Discussion of modal parameters identification through time domain OMA methods applied to the physical systems presented at Chapter 4, will be presented at Chapter 5, aiming to discuss about the challenges, advantages and disadvantages of OMA methods application to extract modal parameters of Centrifugal Compressor.

By last, the conclusion of this work will be presented at Chapter 6.

Chapter 2

State of the Art and Literature Review

In this section, a Literature Review focused on traditional Modal Testing and OMA applied to centrifugal compressors will be presented. Firstly, a brief overview of OMA will be given, aiming to familiarize some readers from turbomachinery engineering community with a subject not widely known by some of its members.

2.1 OMA Overview

The operational modal analysis methods are applied to identify the eigenvalues and eigenvectors of the system through the measurements of vibration, without the necessity of measuring the excitation forces (see diagram at figure 2.1). Thus, no additional device is necessary, making stability tests a simpler task and also making possible to assess compressors stability during its field operation, which can be a powerful vibration troubleshooting tool.

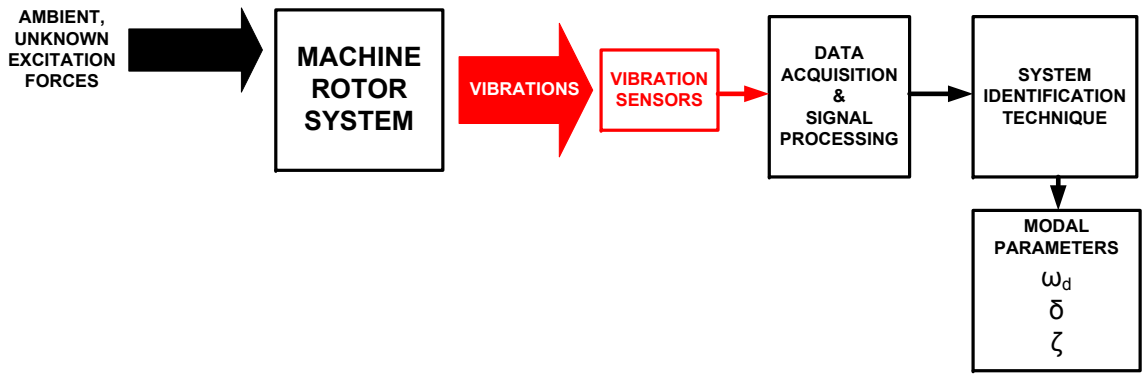

Figure 2.1: Diagram of OMA identification process

The basis of this theory is to consider that the excitation over the structure is a combination of stochastic excitation generated by natural means (like wind,

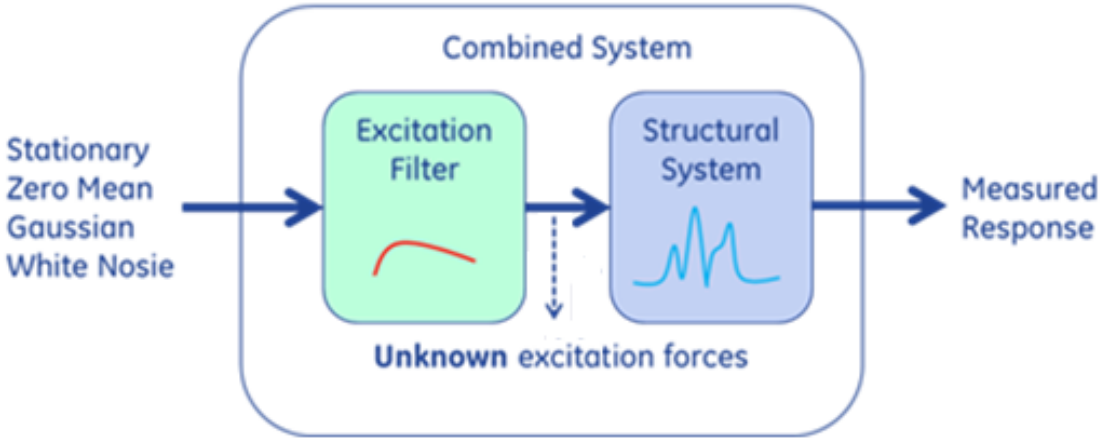

Figure 2.2: OMA theoretical background BRINCKER and VENTURA [1].

sea wave, or turbulence due to process gas flowing through internal channels of the compressor) and deterministic excitation (such as unbalance). This combined excitation force is unknown, but can be described by a filtered stationary, zero mean, Gaussian white noise excitation as described by BRINCKER and VENTURA [1]. Figure 2.2 shows a scheme of the OMA framework. With this framework, it will be shown in Chapter 3 that the poles of the excitation filter and the poles of structural system, along with correspondent eigenvectors (not scalable in OMA), will be estimated by the analyses of measured responses.

Thus the main challenge in OMA is to somehow distinguish the structural system, the excitation filter and computational eigenvalues and eigenvectors. It is important to highlight that the same sort of problems related with the process of modal parameters estimation is present in both OMA and EMA methods. Once the stochastic excitation is of major importance, the acquisition duration and sampling rate are parameters that can have a strong influence in results. Furthermore, stochastic excitation must have enough bandwidth, to cover the interest range of frequencies and be strong enough to provide a good signal to instrument noise ratio. The lack of control over the stochastic excitation can be an issue in OMA applications, mainly in low pressure machines.

2.2 Time Domain OMA methods

OMA has been applied in mechanics for on-the-road modal analysis of cars, in-flight modal analysis of airplanes, modal testing of spacecraft during launch, modal testing of engines during startup and shutdown and modal testing of wind turbines among others. In civil engineering, OMA has become the primary tool for modal testing and the number of reported case studies is abundant (REYNDERS [8]).

The origin of Time Domain OMA methods started in the 1970's. The basis for application of time domain methods to extract modal parameters from output only data was defined in 1974, by AKAIKE [9] and later by BENDAT and PIERSOL [10]. These works recognize that impulse responses and free decays of systems can be obtained by correlation functions between outputs of system, when a white noise excitation is applied.

After that, remarkable time domain techniques were developed and can be cited herein. Examples are Ibrahim Time Domain method (IBRAHAM [11]), developed in 1977, followed, in 1982, by the Polyreference method (VOLD *et al.* [12]) and in 1985 by the Eigenrealization Algorithm (JUANG and PAPPA [13]). Natural Excitation Technique (JAMES *et al.* [14]) was developed in 1995 and finally Stochastic Subspace Identification methods (VAN OVERSCHEE and DE MOOR [3]) were developed in 1996.

In 2000's, efforts were concentrated in uncertainty quantification in modal parameter estimation. A bayesian approach for time domain techniques was developed by YUEN and KATAFYGIOTIS [15], but a recent review in YUEN and KUOK [16] has indicated potential significant bias of this identifiation method. In REYNDERS *et al.* [17] a method to estimate variance of the estimates from a single ambient vibration test using using SSI estimation methods was provided.

Also in 2000's, some efforts were concentrated in harmonic signals elimination, once it is well known that harmonics coinciding with natural frequencies of system can bring challenges to OMA identification. Works as MODAK *et al.* [18], PEETERS *et al.* [19] and QI *et al.* [20] were focused on this subject.

Nowadays, efforts in harmonic signal elimination from the output response and uncertainty quantification of modal parameters identification still ongoing. As exemples, recently a new orthogonal projection-based method was proposed in GRES *et al.* [21] for harmonic signal removal and in REYNDERS *et al.* [22], a validation and application of the method to estimate variance of the estimates obtained from a single ambient vibration test using SSI was performed (together with the validation of an uncertainty quantification method using maximum likelihood, proposed in PINTELON *et al.* [23]).

Although many different OMA algorithms may be found in the literature, the present work focus on Data Driven Stochastic Subspace Identification (SSI), Covariance Driven SSI and Multiple Output Backward Autoregressive (MOBAR) methods.

According to ZHANG and BRINCKER [24], the data driven Stochastic Subspace Identification procedures are the sequence of the state-space system identification (4SID) developed in the nineties, and the advantages of SSI are that it makes direct use of stochastic response data without estimation of covariance as first stage and it can not only be employed for white noise excitation, but also for colored noise. The

SSI algorithm can be employed with 3 methods, Unweighted Principal Components (UPC), Principal Component (PC) and Canonical Variate Analysis (CVA) described in detail in VAN OVERSCHEE and DE MOOR [3]. SSI Covariance Driven are based on the Stochastic Realization algorithms and are defined as a Subspace System Identification method once the eigenvalues of the system are calculated via Singular Value Decomposition (SVD) of covariance matrix ZHANG and BRINCKER [24]. The Stochastic realization algorithm can also be employed in 3 methods, SSI-UPC, PC and CVA.

MOBAR is a time domain technique proposed in 2002 by HUNG and KO [25], aiming to reduce the problems related with spurious modes identified in forward Autoregressive models. This is an extension of the single output backward autoregressive model proposed by KUMARESAN and TUFTS [26]. MOBAR using Blocking Test excitation was successfully applied to extract modal parameters in a lab scale rotor in CLOUD [5] and CLOUD *et al.* [27], in Cage Induction Motors in HOLOPAINEN *et al.* [28] and than it was applied to multistage centrifugal compressors during factory stability tests in PETTINATO *et al.* [2] and NORONHA *et al.* [29]. Although the majority of the MOBAR applications in turbomachinery uses Blocking Test excitations, this technique can be applied to ambient excitation as in the present work.

Further details of each of these techniques will be presented in the Chapter 3.

2.3 Centrifugal Compressor Modal Testing using EMA methods

A complete bibliographic review of Modal Testing of Rotor Systems is given at CLOUD [5], thus the goal of the present review is to point out the current state of this field and advances occurred since the publication of that work.

Since that publication, the most common practice adopted to carry Stability Tests on Centrifugal Compressor is still to use magnetic exciter to apply nonsynchronous excitation to the rotor.

Until 2009, many stability tests were performed using magnetic exciter. It is common to consider sine sweep excitation, while compressor is in operational speed.This allows the computation of Frequency Response Functions (FRFs) and Single Degree of Freedom (SDOF) techniques such as Amplification Factor (AF) and log decrement were adopted to extract the damping ratio as performed in BAUMANN *et al.* [30], MOORE *et al.* [31], SOROKES *et al.* [32] and BIDAUT *et al.* [33] .

Although each term of a transfer function matrix (also valid for a FRF matrix) contains information of all the system's poles (see Appendix B), SDOF techniques

using simple methods as AF or log decrement to estimate damping ratio does not take into account the contribution of each mode. Even though a single peak is present within a sine sweep FRF, backward and forward modes can be participating in this peak response simultaneously (see PETTINATO *et al.* [2]). Many times, these closely space modes leads to meaningful errors in damping identification through simple SDOF based on AF or log decrement, as demonstrated by CLOUD *et al.* [34].

Nowadays, the SDOF methods using AF or log decrement techniques were widely replaced by Single Input Multiple Outputs (SIMO) or Multiple Inputs Multiple Outputs (MIMO) methods, that are both considered Multiple Degrees of Freedom (MDOF) methods, using sine sweep excitations to find FRFs or blocking excitation to find Impulse Response Functions (IRFs). Blocking excitations are performed by using the magnetic exciter to excite a mode of interest applying forward, backward or unidirectional excitation near the frequency of interest and then suddenly interrupting the excitation and capturing the response of the rotor system. After that, system identification techniques as Prediction Error Methods, Stochastic Subspace Identification, Multiple Output Backwards Auto Regressive models, among others, are applied to the obtained FRFs or IRFs in order to extract the modal parameters of the system.

Both, the sine sweep and blocking excitation techniques were applied in Shop Stability Verification Tests as reported in PETTINATO *et al.* [2] and NORONHA *et al.* [29], using Prediction Error Method (PEM) with SIMO and MOBAR methods to extract modal parameters, presenting high level of agreement among the methods.

Most recent publications in the field are related with increasing the accuracy of the modal parameters identification. Two recent examples of that can be cited. Firstly, the development a short-time Fourier transform filter proposed by LI *et al.* [35], aiming to increase the signal-to-noise ratio and improve the accuracy of the estimated stability parameters based on the time-varying characteristics of response vibration during the sine-swept process. Secondly, the method combining the rational polynomials method with the weighted instrumental variables estimator to fit the directional frequency response function (backward and forward FRFs, see [36]), presented at WANG *et al.* [37].

Once new design philosophies and challenging applications has been attracted attention of the academic and industrial communities that work with centrifugal compressors, one may expect new methodologies for the analyses of this type of system in the next years. Furthermore, in the author's vision, the incorporation of Stability Verification Tests in API 617 standard (as optional, with guidelines included) is really welcome and necessary to the industry as a whole, once today each end-user needs to specify or accept the OEM proposition for techniques applied,

acceptance criteria, operational conditions and results extrapolation methodology (to other operational conditions) of the stability test.

2.4 Time Domain OMA Applied to Centrifugal Compressors

Detailed investigation of OMA applied to rotor systems was performed in 1997, when output measurements only techniques as Random Decrement and Yule-Walker equation were modified by ZHONG [38]. Zhong applied these techniques to rotor-bearing system synthetic data for modal parameters and physical properties extraction, but since then it took a while for real applications to turbomachinery.

Recently, in QI *et al.* [20] a novel method were proposed for OMA applied to linear rotor systems, combined with correction technique of spectrum analysis, harmonic wavelet filtering, random decrement technique and Hilbert transform methods.

Application of OMA to centrifugal compressors are reported in GUGLIELMO *et al.* [39], GUGLIELMO *et al.* [7] and CARDEN *et al.* [40]. In GUGLIELMO *et al.* [39], OMA and EMA were applied to a low pressure LNG compressor in different load conditions during a Full Load Stability test, comparing the obtained results. In GUGLIELMO *et al.* [7], OMA and EMA were applied to a high pressure Reinjection compressor and also to a rotordynamic model, highlighting some aspects of OMA analysis that are specific to centrifugal compressors and comparing both techniques through a large span of damping. In CARDEN *et al.* [40], OMA was used to confirm that the first forward mode of an 500 kw compressor was actually stable and the measurements were reconciled with the predicted behavior.

In opposition to centrifugal compressors, in the past few years several works related with OMA application to wind turbines are found in the literature, as example of OZBEK and RIXEN [41], ALLEN *et al.* [42], CHAUHAN *et al.* [43], DEVRIENDT *et al.* [44] among others. In this sense, the present work analyses application of OMA to centrifugal compressors, aiming to incentive the increasing of its use for modal testing at shop, as alternative or complement of traditional EMA tests, and during field operation, as a troubleshooting and conditioning monitoring tool.

Chapter 3

Time Domain OMA Methods: Theoretical Basis

As stated before, the focus of the present work is the application of time domain OMA methods to extract modal parameters of turbomachinery during its field operation.

This chapter provides the theoretical basis of the data driven and covariance driven Stochastic Subspace Identification methods and MOBAR method studied in the present work.

Prior to read this chapter, the interested reader in encouraged to consult Appendix B, that contains the basic concepts necessary to understand OMA theoretical fundamentals contained herein.

3.1 Stochastic Vibrations

This section presents the concepts of Stochastic Vibration. Some concepts and details concerning this topic may be found in Appendix B. The reader may found complete information concerning this topic in BRINCKER and VENTURA [1] and VAN OVERSCHEE and DE MOOR [3].

3.1.1 OMA's Fundamental Theorem

This subsection presents OMA's Fundamental Theorem for Multiple Input Multiple Output (MIMO) systems, as described by BRINCKER and VENTURA [1]. This theorem is the basis of all existing OMA methods.

Let us consider that the set of measured data from a system in operation is organized in a vector $\underset{\sim}{y}$ (vectors defined herein are all column vectors). The outputs correlation matrix $\boldsymbol{R}_y$ is given by equation 3.1. It is worth notice that all the response

signals analyzed herein have its mean value subtracted from the raw signal, thus the correlation and covariance functions are the same.

$$\boldsymbol{R}_y(\tau) = E[\underset{\sim}{y}(t)\underset{\sim}{y}^T(t+\tau)] \tag{3.1}$$

Replacing $\underset{\sim}{y}^T(t+\tau)$ in equation 3.1, by $\underset{\sim}{y}$ calculated according to equation B.11, where $\boldsymbol{H}$ is the impulse response function matrix, using the convolution definition and taking into account that the expected value $E[\underset{\sim}{y}(t)\underset{\sim}{u}^T(t+\tau-\alpha)]$ is the cross correlation matrix $\boldsymbol{R}_{yu}(\tau-\alpha)$, the result is the equation 3.2.

$$\boldsymbol{R}_y(\tau) = \int_{-\infty}^{+\infty} E[\underset{\sim}{y}(t)\underset{\sim}{u}^T(t+\tau-\alpha)]\boldsymbol{H}^T(\alpha)d\alpha = \boldsymbol{R}_{yu}(\tau) * \boldsymbol{H}^T(\tau) \tag{3.2}$$

The cross correlation matrix $\boldsymbol{R}_{yu}(\tau)$, between outputs and inputs, can be represented by equation 3.3.

$$\boldsymbol{R}_{yu}(\tau) = \int_{-\infty}^{+\infty} \boldsymbol{H}(\alpha)E[\underset{\sim}{u}(t-\alpha)\underset{\sim}{u}^T(t+\tau)]d\alpha \tag{3.3}$$

The expected value $E[\underset{\sim}{u}(t-\alpha)\underset{\sim}{u}^T(t+\tau)]$, that appears in equation 3.3 is the correlation matrix $\boldsymbol{R}_u(\tau+\alpha)$ of the inputs. By changing the integration variable of equation 3.3 to $\beta = -\alpha$, equation 3.4 is obtained.

$$\boldsymbol{R}_{yu}(\tau) = \boldsymbol{H}(-\tau) * \boldsymbol{R}_u(\tau) \tag{3.4}$$

Combining equations 3.2 and 3.4, the fundamental theorem arises, as per equation 3.5.

$$\boldsymbol{R}_y(\tau) = \boldsymbol{H}(-\tau) * \boldsymbol{R}_u(\tau) * \boldsymbol{H}^T(\tau) \tag{3.5}$$

The Fourier transform of equation 3.5, leads to fundamental theorem in frequency domain, according to equation 3.6, where $\boldsymbol{G}$ is called spectral densities matrix and $\boldsymbol{H}(\tilde{\boldsymbol{i}}\boldsymbol{\Omega})$ frequency response function matrix.

$$\boldsymbol{G}_y(\Omega) = \tilde{\boldsymbol{H}}(-i\Omega)\boldsymbol{G}_u(\Omega)\tilde{\boldsymbol{H}}^T(i\Omega) \tag{3.6}$$

Considering white noise input, inputs correlation matrix can be written according to equation 3.7 and inputs spectral densities matrix can be written according to equation 3.8, where B is the inputs spectral bandwidth and $\sigma^2_{u_n}$ is the variance of input n.

$$\boldsymbol{R}_u(\tau) = 2\pi\frac{\delta(\tau)}{2B}\begin{bmatrix}\sigma^2_{u_1} & & \\ & \ddots & \\ & & \sigma^2_{u_n}\end{bmatrix} \tag{3.7}$$

$$\boldsymbol{G}_u(\Omega) = \frac{1}{2B}\begin{bmatrix}\sigma_{u_1}^2 & & \\ & \ddots & \\ & & \sigma_{u_n}^2\end{bmatrix} \tag{3.8}$$

Substituting equation 3.7 into equation 3.5, considering the convolution property of Dirac's δ, the output correlation matrix is given by equation 3.9. This equation shows that the outputs correlation matrix contains all the information about the system dynamics, since it is simply the convolution of impulse response functions multiplied by constants.

A similar result is obtained for spectral density matrix, as per equation 3.10, showing that the outputs spectral density matrix is a frequency response function matrix operation, multiplied by constants.

$$\boldsymbol{R}_y(\tau) = \frac{\pi}{B}\begin{bmatrix}\sigma_{u_1}^2 & & \\ & \ddots & \\ & & \sigma_{u_n}^2\end{bmatrix} \boldsymbol{H}(-\tau) * \boldsymbol{H}^T(\tau) \tag{3.9}$$

$$\boldsymbol{G}_y(\Omega) = \frac{1}{2B}\begin{bmatrix}\sigma_{u_1}^2 & & \\ & \ddots & \\ & & \sigma_{u_n}^2\end{bmatrix} \tilde{\boldsymbol{H}}(-i\Omega)\tilde{\boldsymbol{H}}^T(i\Omega) \tag{3.10}$$

3.1.2 Correlation Functions as Impulse Response or Free Decays

Considering a system with n-degrees of freedom, represented at state space, the system's response can be written as a linear combination of $2n$ complex conjugate modeshapes (given by the first n elements of state space eigenvector X_r, as per equation 3.11), according to equation 3.12.

$$\underset{\sim}{\Phi}_r = \underset{\sim}{X}_{r_{(1:n)}} \tag{3.11}$$

$$\underset{\sim}{x}_{(1:n)}(t) = \boldsymbol{\Phi}\underset{\sim}{q}(t) = \sum_{r=1}^{2n} \underset{\sim}{\Phi}_r q_r(t) \tag{3.12}$$

Thus, the modal coordinates $q_r(t)$, represents the influence of each mode on the system's response. The modal coordinates can be calculated through the convolution of modal impulse responses $h_r(t)$ and modal force $U_{\Phi_r}(t)$, as shown in equation 3.13.

$$q_r(t) = h_r(t) * U_{\Phi_r}(t) = \int_{-\infty}^{t} h_r(t-\tau)U_{\Phi_r}(\tau)d\tau \tag{3.13}$$

The modal force is given by equation 3.14 and the modal impulse response $h_r(t)$ is given by equation 3.15. The term a_r represents the norm of modeshape r, as per equation 3.16.

$$U_{\Phi_r}(t) = \underset{\sim}{\Phi}_r^T \underset{\sim}{u}(t) \tag{3.14}$$

$$h_r(t) = \frac{1}{a_r} e^{\lambda_r t} \tag{3.15}$$

$$a_r = \underset{\sim}{\Phi}_r^T \underset{\sim}{\Phi}_r \tag{3.16}$$

Combining equations 3.12, 3.13, 3.14, leads to the expression 3.17.

$$\underset{\sim}{x}_{(1:n)}(t) = \sum_{r=1}^{2n} \underset{\sim}{\Phi}_r \underset{\sim}{\Phi}_r^T \int_{-\infty}^{t} h_r(t-\tau) \underset{\sim}{u}(\tau) d\tau \tag{3.17}$$

Evaluating the response in position i, due to the application of an unitary impulse at position j, the impulse response function $h_{i,j}$ is found in accordance with equation 3.18.

$$h_{i,j}(t) = \sum_{r=1}^{n} \frac{\Phi_{r_i} \Phi_{r_j}}{a_r} e^{\lambda_r t} + \frac{\Phi_{r_i}^* \Phi_{r_j}^*}{a_r} e^{\lambda_r^* t} \tag{3.18}$$

Moreover, for white noise inputs it can be demonstrated that each element $R_{y_i y_j}$ of the output's correlation function matrix is given according with equation 3.19. This means that each correlation function is a sum of decaying sinusoids of the same form as the corresponding impulse response function of the original system (JAMES *et al.* [14]).

$$R_{y_i y_j}(\tau) = \sum_{r=1}^{n} \Phi_{r_i} \gamma_{r_j} e^{\lambda_r t} + \Phi_{r_i}^* \gamma_{r_j} e^{\lambda_r^* t} \tag{3.19}$$

This fact allows a close relation between EMA and OMA methods, where the outputs Correlation Functions in OMA, are related with the Impulse Response Functions (IRF) that are the basis of the identification performed in many time domain EMA methods and the Fourier transform of outputs Correlation function, known as Power Spectral Densities (PSD), are related with the Frequency Response Functions, that are the basis of identification performed in frequency domain EMA methods. This relations are represented in figure 3.1.

Free decays and impulse responses are closely related entities, once an impulse is equivalent to a free decay with non null velocities as initial conditions.

Thus, another interpretation frequently given is that the outputs correlation elements are proportional to free decays, with initial condition that can be found

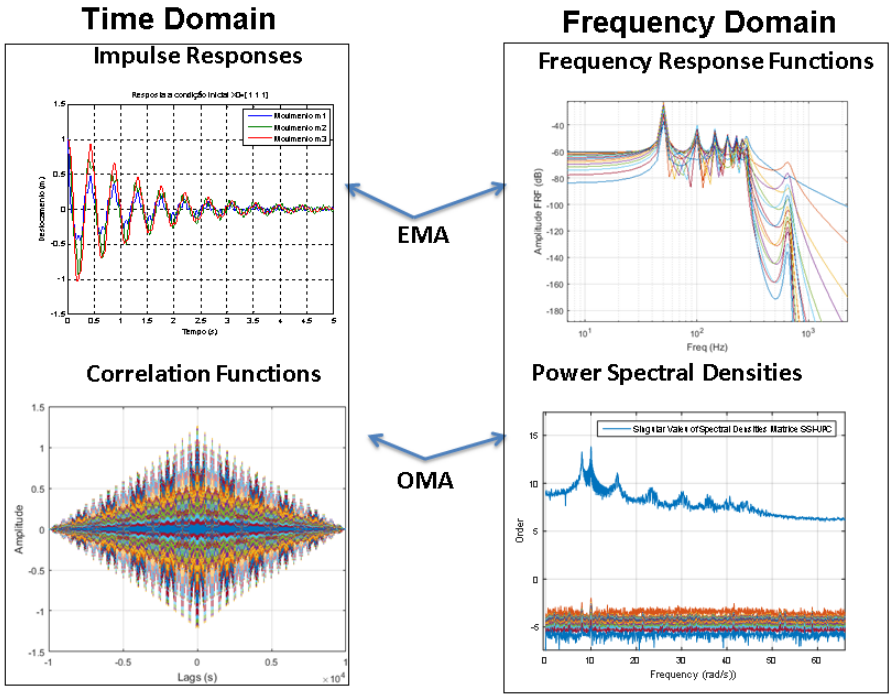

Figure 3.1: EMA vs OMA

through OMA methods (see BRINCKER and VENTURA [1]). In the author's vision, this is a better physical interpretation of correlation functions, once allows to interpret the modal participation vector γ_r as a result of a non null initial condition, to be determined through OMA process.

It also can be demonstrated, that for small damping, the modal participation vector is proportional to the modeshape vector. Moreover, special care must be taken in relation with the correlation function definition. Using the definition adopted in the present work (equation 3.1), only the rows of correlation function are proportional to the modeshapes and considering a wrong form of correlation function, can lead to modeshape bias (see BRINCKER and VENTURA [1]).

3.2 The Eigensystem Realization Algorithm

3.2.1 Impulse

Considering the discrete representation given by equations B.53 and B.56, for a system at rest for $t < 0$, the application of an unitary impulse at time t=0 leads to the representation of impulse response function matrix given by equations 3.20 and 3.21, where k is the $k-th$ discrete time step.

$$\boldsymbol{h}(0) = \boldsymbol{D} \tag{3.20}$$

$$\boldsymbol{h}(k) = \begin{bmatrix} h_{1,1}(k) & h_{1,2}(k) & \dots & h_{1,na}(k) \\ h_{2,1}(k) & h_{2,2}(k) & \dots & h_{2,na}(k) \\ \vdots & \vdots & \ddots & \vdots \\ h_{ns,1}(k) & h_{ns,2}(k) & \dots & h_{ns,na}(k) \end{bmatrix} = \mathbb{C}\boldsymbol{A}_d^{k-1}\boldsymbol{B_d} = \boldsymbol{Y_{m_k}} \tag{3.21}$$

The element $h_{i,j}(k)$ is the response at position i due to an unitary impulse at position j, na is the number of inputs and ns is the number of measured outputs.

One of the main steps on Eigenystem Realization Algorithm (ERA), presented by JUANG and PAPPA [13] is to assemble a Hankel matrix according to equation 3.22, where the number of block rows s is user defined, being related with the order of problem, and np is the number of discrete time samples.

$$\boldsymbol{H_1} = \begin{bmatrix} \boldsymbol{h_1} & \boldsymbol{h_2} & \dots & \boldsymbol{h_{np-s+1}} \\ \boldsymbol{h_2} & \boldsymbol{h_3} & \dots & \boldsymbol{h_{np-s+2}} \\ \vdots & \vdots & \ddots & \vdots \\ \boldsymbol{h_{s+1}} & \boldsymbol{h_{s+2}} & \dots & \boldsymbol{h_{np+1}} \end{bmatrix} \tag{3.22}$$

Using equation 3.21, it is easy to see that the Hankel matrix can be decomposed according to equation 3.23, where Γ is the observability matrix given by equation 3.24, and Δ is the controllability matrix given by equation 3.25.

$$\boldsymbol{H_1} = \boldsymbol{\Gamma\Delta} \tag{3.23}$$

$$\boldsymbol{\Gamma} = \begin{bmatrix} \mathbb{C} \\ \mathbb{C}\boldsymbol{A_d} \\ \mathbb{C}\boldsymbol{A_d}^2 \\ \vdots \\ \mathbb{C}\boldsymbol{A_d}^s \end{bmatrix} \tag{3.24}$$

$$\Delta = \begin{bmatrix} \boldsymbol{B_d} & \boldsymbol{A_d B_d} & \dots & \boldsymbol{A_d}^{np-s-1}\boldsymbol{B_d} & \boldsymbol{A_d}^{np-s}\boldsymbol{B_d} \end{bmatrix} \tag{3.25}$$

Performing a Singular Value Decomposition (SVD) of the Hankel matrix (equation 3.26), allows one to calculate the observability matrix, according to equation 3.27.

$$\boldsymbol{H_1} = \boldsymbol{USV}^T \tag{3.26}$$

$$\hat{\boldsymbol{\Gamma}} = \boldsymbol{US}^{1/2} \tag{3.27}$$

After estimating the observability matrix, the discrete state space matrix $\boldsymbol{A_d}$ can be estimated by equation 3.28, where † is the pseudo-inverse, $\hat{\mathbf{\Gamma}}_{1:s}$ is the estimator of observability matrix removing the last block, while in $\hat{\mathbf{\Gamma}}_{2:s+1}$ the first block is removed.

$$\hat{\boldsymbol{A_d}} = \hat{\mathbf{\Gamma}}^{\dagger}_{1:s}\hat{\mathbf{\Gamma}}_{2:s+1} \tag{3.28}$$

The estimator for the matrix $\mathbb{C}$ is given by the first block of observability matrix as per equation 3.29.

$$\hat{\mathbb{C}} = \hat{\mathbf{\Gamma}}_{1:1} \tag{3.29}$$

After finding the system matrix $\hat{\boldsymbol{A_d}}$, the discrete eigenvalues $\boldsymbol{\mu}$ are identified through a spectral decomposition, as shown in Equation 3.30 and then the continuous eigenvalue λ_i can be calculated through 3.31, where Δt is sampling interval.

$$\hat{\boldsymbol{A_d}} = \boldsymbol{\Psi\mu\Psi}^{-1} \tag{3.30}$$

$$\lambda_i = \frac{ln\mu_i}{\Delta t} \tag{3.31}$$

The mode shapes are found using the observation matrix $\mathbb{C}$ and the eigenvectors matrix Ψ, through equation 3.32.

$$\boldsymbol{\phi} = \hat{\mathbb{C}}\boldsymbol{\psi} \tag{3.32}$$

3.2.2 Free Decays

Considering that, instead of an unitary impulse applied at time t=0, the system is submitted to a set of non null initial conditions, the discrete state space formulation leads to equation 3.33.

$$\underset{\sim}{y}(k) = \mathbb{C}\boldsymbol{A_d}^k\underset{\sim}{x}_0 \tag{3.33}$$

Assembling a matrix of initial conditions $\boldsymbol{X_0}$, a free decay response matrix corresponding to the discrete time k can be built according to equation 3.34.

$$\boldsymbol{Y}(k) = \mathbb{C}\boldsymbol{A_d}^k\boldsymbol{X_0} \tag{3.34}$$

A Hankel matrix of free decays can be built, as per equation 3.35.

$$\boldsymbol{H_0} = \begin{bmatrix} \boldsymbol{Y_0} & \boldsymbol{Y_1} & \dots & \boldsymbol{Y_{np-s}} \\ \boldsymbol{Y_1} & \boldsymbol{Y_2} & \dots & \boldsymbol{Y_{np-s+1}} \\ \vdots & \vdots & \ddots & \vdots \\ \boldsymbol{Y_s} & \boldsymbol{Y_{s+1}} & \dots & \boldsymbol{Y_{np}} \end{bmatrix} \tag{3.35}$$

This Hankel matrix can be decomposed into an observability and an controllability matrix as per equations 3.36 and 3.37.

$$\boldsymbol{\Gamma} = \begin{bmatrix} \mathbb{C} \\ \mathbb{C}\boldsymbol{A_d} \\ \mathbb{C}\boldsymbol{A_d}^2 \\ \vdots \\ \mathbb{C}\boldsymbol{A_d}^{s-1} \end{bmatrix} \tag{3.36}$$

$$\boldsymbol{\Delta} = \begin{bmatrix} \boldsymbol{X_0} & \boldsymbol{A_d X_0} & \boldsymbol{A_d}^2\boldsymbol{X_0} & \dots & \boldsymbol{A_d}^{np-s-2}\boldsymbol{X_0} & \boldsymbol{A_d}^{np-s-1}\boldsymbol{X_0} \end{bmatrix} \tag{3.37}$$

Performing a SVD of the Hankel matrix, allows to calculate the observability matrix and then extract the modal parameters, in the same manner shown for ERA considering impulse.

For free decays, the controllability matrix estimated as per equation 3.38, allows to estimate the non null initial conditions contained in matrix $\boldsymbol{X_0}$, according to equation 3.39.

$$\hat{\boldsymbol{\Delta}} = \boldsymbol{S}^{1/2}\boldsymbol{V}^T \tag{3.38}$$

$$\hat{\boldsymbol{X_0}} = \hat{\boldsymbol{\Delta}}_{1:1} \tag{3.39}$$

3.3 Stochastic Subspace Identification Methods

The OMA Stochastic Subspace Identification (SSI) are time domain methods that uses the discrete time state spaces to find the eigenvalues and eigenvectors of the system.

There are two main kinds of SSI methods, the covariance driven and data driven. The covariance driven methods rely on covariance of system's outputs to build a Hankel matrix as in equation 3.40.

$$\boldsymbol{H} = \begin{bmatrix} \boldsymbol{R_0} & \boldsymbol{R_1} & \dots & \boldsymbol{R_{np-s}} \\ \boldsymbol{R_1} & \boldsymbol{R_2} & \dots & \boldsymbol{R_{np-s+1}} \\ \vdots & \vdots & \ddots & \vdots \\ \boldsymbol{R_s} & \boldsymbol{R_{s+1}} & \dots & \boldsymbol{R_{np}} \end{bmatrix} \tag{3.40}$$

Once correlation matrix represents free decays, this Hankel Matrix can be decomposed into a stochastic observability matrix $\boldsymbol{\Gamma_s}$ and a stochastic controllability matrix $\boldsymbol{\Delta_s}$, and the modal parameters can be extracted in the same manner shown for the ERA's method. Such method is know as Covariance Driven Unweighted Principal Component.

In data driven SSI methods, a Block Hankel Matrix $\boldsymbol{Y_h}$, defined by a set of responses in past times $\boldsymbol{Y_{hp}}$ and a set of responses in future times $\boldsymbol{Y_{hf}}$ is the key element, being defined through equation 3.41.

The discrete response data matrix $\boldsymbol{y}$ is defined according to equation 3.42 and $\boldsymbol{y}_{1:np-k}$ is defined as a data matrix where we have removed the last k lags and similarly, $\boldsymbol{y}_{k:np}$ is the data matrix where we have removed the first k lags.

$$\boldsymbol{Y_h} = \begin{bmatrix} \boldsymbol{y}_{1:np-2s} \\ \boldsymbol{y}_{2:np-2s+1} \\ \vdots \\ \boldsymbol{y}_{2s:np} \end{bmatrix} = \begin{bmatrix} \boldsymbol{Y_{hp}} \\ \hdashline \boldsymbol{Y_{hf}} \end{bmatrix} \tag{3.41}$$

$$\boldsymbol{y} = \begin{bmatrix} \underset{\sim}{y}_1 & \underset{\sim}{y}_2 & \dots & \underset{\sim}{y_{np}} \end{bmatrix} \tag{3.42}$$

The user-defined variable s, as well as the amount of measurement channels defines the maximum order of model and must be adjusted by choosing a reasonable level to incorporate the needed range of models BRINCKER and ANDERSEN [45].

The key element of data driven methods is the projection of $\boldsymbol{Y_{hp}}$ rows space, into the $\boldsymbol{Y_{hf}}$ rows space (equation 3.43). According to BRINCKER and ANDERSEN [45], when dealing with stochastic response, this projection is defined as the expected values of future, once the past is known (conditional mean).

$$\boldsymbol{O} = E(\boldsymbol{Y_{hf}} \mid \boldsymbol{Y_{hp}}) = \boldsymbol{Y_{hf}}\boldsymbol{Y_{hp}}^T(\boldsymbol{Y_{hp}}\boldsymbol{Y_{hp}}^T)^{-1}\boldsymbol{Y_{hp}} \tag{3.43}$$

It is worth notice that the first two terms in equation 3.43 are equivalent to the Hankel matrix used in covariance driven methods (thus decomposed into observability and controllability matrix), the next term is the inverse a block Toeplitz matrix constructed from outputs correlation functions, named $\boldsymbol{L}$. The product of controllability matrix, inverse of block Toeplitz matrix $\boldsymbol{L}$ and $\boldsymbol{Y_{hp}}$, defines the Kalman filter states $\boldsymbol{X_0}$ (equation 3.44), thus this projection leads to a matrix that can be

decomposed into the observability matrix and the Kalman states matrix (equation 3.45).

$$\boldsymbol{X_0} = \boldsymbol{\Delta} \boldsymbol{L}^{-1} \boldsymbol{Y_{hp}} \tag{3.44}$$

$$\boldsymbol{O} = \boldsymbol{\Gamma} \boldsymbol{X_0} \tag{3.45}$$

The columns of this matrix represents free decays, given by different initial conditions specified by the Kalman states (BRINCKER and ANDERSEN [45]).

From the exposition made so far, it is clear that the main difference between covariance driven and data driven method is in the matrices $\boldsymbol{H}$ and $\boldsymbol{O}$. In the first, the matrix $\boldsymbol{H}$ is decomposed in observability and controllability matrix and in the last, matrix $\boldsymbol{O}$ is decomposed in observability and Kalman states matrix.

Moreover, the matrix $\boldsymbol{O}$ from data driven methods can be seen as a weighted covariance driven Hankel matrix, with weight $(\boldsymbol{Y_{hp}} \boldsymbol{Y_{hp}}^T)^{-1} \boldsymbol{Y_{hp}}$.

The next step of the Data Driven methods is to left multiply the matrix $\boldsymbol{O}$ by a weight matrix $\boldsymbol{W_1}$ and right multiply the matrix $\boldsymbol{O}$ by a weight matrix $\boldsymbol{W_2}$.

Three different manners to define these weight matrices were adopted herein, representing the different Data Driven SSI algorithms studied: UPC, PC and CVA. Table 3.1 presents the definition of the weight matrices for each of these methods, where $\boldsymbol{I_s}$ is an identity matrix with size compatible with $\boldsymbol{\Gamma}$ rows and $\boldsymbol{I_{np}}$ is an identity matrix with size compatible with $\boldsymbol{X_0}$ columns. Additional information can be find in VAN OVERSCHEE and DE MOOR [3].

Table 3.1: Definition of weight matrices $\boldsymbol{W_1}$ and $\boldsymbol{W_2}$ according to different SSI algorithms (see VAN OVERSCHEE and DE MOOR [3])

	$\boldsymbol{W_1}$	$\boldsymbol{W_2}$
PC	$\boldsymbol{I_s}$	$\boldsymbol{Y_{hp}}^T \boldsymbol{L}^{-1/2} \boldsymbol{Y_{hp}}$
UPC	$\boldsymbol{I_s}$	$\boldsymbol{I_{np}}$
CVA	$(\boldsymbol{Y_{hf}} \boldsymbol{Y_{hf}}^T)^{-1/2}$	$\boldsymbol{I_{np}}$

.

After that, the steps of OMA data driven methods are the same then the described for covariance driven methods, thus the Kalman States and observability matrix can be estimated through the SVD of the weighted matrix $\boldsymbol{W_1 O W_2}$, the estimators $\hat{\boldsymbol{A}}_{\boldsymbol{d}}$ and $\hat{\mathbb{C}}$ can be found from observability matrix (through linear regression) and the eigenvalues and eigenvectors can be calculated from the $\hat{\boldsymbol{A}}_{\boldsymbol{d}}$.

The model order can be varied by varying the number of singular value taken into account when performing the singular value decomposition of the weighted matrix $\boldsymbol{W_1 O W_2}$. It is a common practice to vary the order and extract the modal parameters, creating a stabilization diagram, allowing separation between physical

and numerical (generated by noise) modes, once the physical modes are repeated for multiple orders of the model.

More details of SSI methods are found VAN OVERSCHEE and DE MOOR [3] and in BRINCKER and ANDERSEN [45].

3.4 MOBAR

The ARMA model presented in Appendix B have direct relation with the discrete state space model given by equation B.53. By multiplying both sides of equation B.53 by $\boldsymbol{A_d}^{-1}$ and solving for $\underset{\sim}{x}(k)$, equation 3.46 arises.

$$\underset{\sim}{x}(k) = \boldsymbol{A_d}^{-1}\underset{\sim}{x}(k+1) - \boldsymbol{A_d}^{-1}\boldsymbol{B_d}\underset{\sim}{u}(k) \tag{3.46}$$

This is a backward time model that can be very useful for modal parameters identification of a system model [46].

Regarding free decays, the state space model is closely related with the AR model, once B_d is zero. In the same manner, for free decays a backward auto-regressive model can be built as per equation 3.47, where b_{c_k} are the backward auto-regressive coefficients, being close related with the backward time model with B_d zero.

$$y(1) = \sum_{k=1}^{s} b_{c_k} y(k+1) + \epsilon \tag{3.47}$$

An expansion of this model to consider multiple outputs can be performed by replacing the coefficients b_{c_k} by the backward auto-regressive matrices $\boldsymbol{B_{c_k}}$, as per equation 3.48.

$$\underset{\sim}{y}(1) = \sum_{k=1}^{s} \boldsymbol{B_{c_k}}\underset{\sim}{y}(k+1) + \underset{\sim}{\epsilon} \tag{3.48}$$

Then, in the same manner that Poly Reference time domain method [12] presented in Appendix B, the Multiple Output Backward Auto-Regressive matrices can be found by building a Hankel matrix with the free decays response, as per equation 3.49 and a block Hankel matrix with only a single block row as per equation 3.50, and solving the overdetermined system of equation 3.51 by least squares or singular value decomposition. In the same manner as for Covariance Driven SSI methods, for Operational Modal Analysis through MOBAR, instead of free decays or impulse response functions, the correlation function of the response are the inputs of the method.

$$\boldsymbol{H_1} = \begin{bmatrix} \underline{y}(2) & \underline{y}(3) & \cdots & \underline{y}(np-s+1) \\ \underline{y}(3) & \underline{y}(4) & \cdots & \underline{y}(np-(s)) \\ \vdots & \vdots & \ddots & \vdots \\ \underline{y}(s+1) & \underline{y}(s+2) & & \underline{y}(np) \end{bmatrix} \tag{3.49}$$

$$\boldsymbol{H_2} = \begin{bmatrix} \underline{y}(1) & \underline{y}(2) & \cdots & \underline{y}(np-s) \end{bmatrix} \tag{3.50}$$

$$\boldsymbol{B_c H_1} = \boldsymbol{H_2} \tag{3.51}$$

$\boldsymbol{B_c}$ is given by equation 3.52.

$$\boldsymbol{B_c} = \begin{bmatrix} \boldsymbol{B}_{c_1} & \boldsymbol{B}_{c_2} & \cdots & \boldsymbol{B}_{c_s} \end{bmatrix} \tag{3.52}$$

Although the work of HUNG and KO [25] is related to one degree of freedom, it makes statements about the ill conditioned solution of least square problem of MOBAR, thus suggesting a solution by SVD with elimination of the less meaningful singular values. This approach is adopted in the present work.

After finding the backward auto-regressive matrices, the backward companion matrix must be build, in accordance with equation 3.53. This matrix is close related with $\boldsymbol{A_d}^{-1}$ of the backward time model.

$$\boldsymbol{B_{comp}} = \begin{bmatrix} \boldsymbol{B_{c_1}} & \boldsymbol{B_{c_2}} & \cdots & \boldsymbol{B_{c_s}} \\ \boldsymbol{I} & \boldsymbol{0} & \boldsymbol{0} & \boldsymbol{0} \\ \vdots & \boldsymbol{0} & \ddots & \vdots \\ \boldsymbol{0} & \vdots & \boldsymbol{I} & \boldsymbol{0} \end{bmatrix} \tag{3.53}$$

The main advantage of MOBAR over AR models is that computational modes are automatically eliminated once stable modes are outside the unit circle of discrete time as shown in KUMARESAN and TUFTS [26].

Chapter 4

Physical Systems

The OMA algorithms analyzed in the present work will be applied to problems of different complexity. This chapter describes these physical systems.

First a model with three masses, springs and dampers will be adopted.

Secondly, a finite element rotor model was chosen.

Finally, OMA will be applied to a real centrifugal compressor during its field operation.

4.1 Mass Spring Damper Model

In this section a simple system composed of three masses, three springs and three dampers, with configuration shown in figure 4.1, will be modeled.

Different load excitation will be applied to this model and the vibration response will be the input of OMA methods, aiming to extract the modal parameters under these different loads and compare the results with reference parameters of the model.

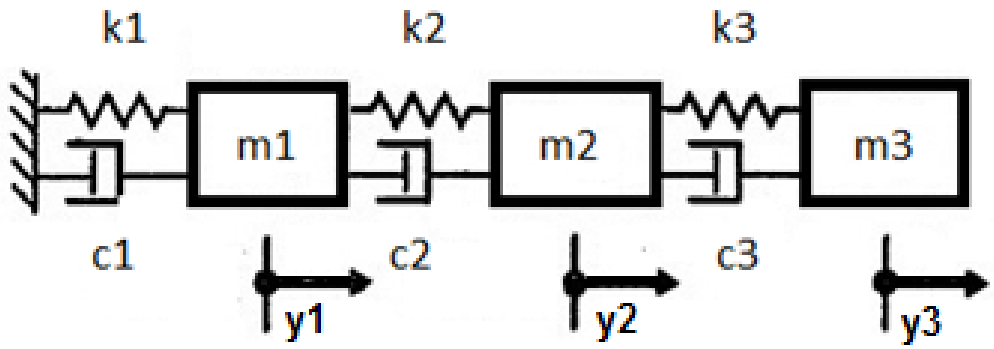

Figure 4.1: Mass Spring Damper Model.

The governing equation of this system is given as by equation 4.1.

$$\begin{bmatrix} m_1 & 0 & 0 \\ 0 & m_2 & 0 \\ 0 & 0 & m_3 \end{bmatrix} \begin{bmatrix} \ddot{y_1} \\ \ddot{y_2} \\ \ddot{y_3} \end{bmatrix} + \begin{bmatrix} c_1 + c_2 & -c_2 & 0 \\ -c_2 & c_2 + c_3 & -c_3 \\ 0 & -c_3 & c_3 \end{bmatrix} \begin{bmatrix} \dot{y_1} \\ \dot{y_2} \\ \dot{y_3} \end{bmatrix} + \begin{bmatrix} k_1 + k_2 & -k_2 & 0 \\ -k_2 & k_2 + k_3 & -k_3 \\ 0 & -k_3 & k_3 \end{bmatrix} \begin{bmatrix} y_1 \\ y_2 \\ y_3 \end{bmatrix} = \begin{bmatrix} u_1 \\ u_2 \\ u_3 \end{bmatrix} \tag{4.1}$$

The configuration chosen for the system parameters is shown is table 4.1.

Table 4.1: System parameters.

Parameter	Value	Parameter	Value	Parameter	Value
m_1	1 kg	c_1	2 $N/(m.s)$	k_1	1600 N/m
m_2	1 kg	c_2	2 $N/(m.s)$	k_2	1600 N/m
m_3	1 kg	c_3	2 $N/(m.s)$	k_3	1600 N/m

The modal parameters of this system can be extracted by vanishing the force term in the right side of equation 4.1, rewriting the resulting equation in state space as per equation B.26 and solving the eigenproblem for state matrix $\boldsymbol{A}$. The extracted parameters are shown in Table 4.2.

The difference between the modal parameters that will be identified by OMA and the modal parameters extracted in table 4.2, can give insights about the quality of identification regarding the influence of the applied load (colored noise, white noise, harmonics), Signal to Noise Ratio, sampling rate, sampling time, model orders among others.

Table 4.2: System eigenvalues and eigenvectors.

Mode	First	Second	Third
w_n (Hz)	2.8332	7.9385	11.4715
w_d (Hz)	2.8330	7.9347	11.4598
ξ	0.0111	0.0312	0.0450
Φ	$[0.445\ 0.802\ 1]^T$	$[1\ 0.445\ -0.802]^T$	$[-0.802\ 1\ -0.445]^T$

4.2 Finite Element Rotor Model

Rotating equipment present some dynamic aspects that differ from general structural system's dynamics. Examples of characteristics that are intrinsic to these equipments are:

- rotordynamic coefficients of components such as bearings, labyrinth seals, damper seals and impellers (aerodynamic cross-coupling) are both speed and process dependent;

- these elements can present anisotropic stiffness and damping coefficients;
- gyroscopic and cross coupling stiffness matrices are skew symmetric, coupling the movement in horizontal and vertical directions;
- cross coupling stiffness signs for horizontal and vertical direction produces feedback forces which helps to destabilize the forward whirling mode (CLOUD [5]);

Besides these characteristics, rotating equipment present backward and forward precession modes that are closely spaced, increasing the challenges related with the modal parameters identification of these systems.

Thus, to verify aspects of modal parameters identification through OMA methods that are specific for rotating equipment applications, a FEM rotordynamic model was implemented.

This model consist of three key elements:

(i) shaft elements, implemented using Euler beam model, with its gyroscope influence added, contributing to the global stiffness, mass and gyroscope matrices;

(ii) built-on parts elements (impellers, gears, fans, disk, couplings) considered to have just inertia contribution, thus affecting the global gyroscope and mass matrices;

(iii) support system, labyrinth seals and damper seal elements, with its contribution in global stiffness and damping matrices. The coefficients of bearing are calculated by thermo-elasto-hidrodynamic analysis using the finite element method as performed by HE [47] and the seal coefficients are calculated by bulk-flow models described in KLEYNHANS [48];

The methodology followed in the implemented model is described in details in FRISWELL [49], SILVA [50] and its full description will be omitted here once it is out of the scope of the present work.

The geometry of the analyzed rotor is shown in figure 4.2.

To validate the implemented model, the same rotor was modeled in a benchmark FEM software from Texas A&M University, named XLTRC2. The Undamped Critical Speed Maps obtained from the implemented algorithm and from XLTRC2 are shown in figure 4.3. One may observe a high level of agreement between the predictions provided the two models. This is an indication in favor of the model implemented for this work.

Three variations of the implemented model will be used to generate synthetic data for application of OMA methods, being: rotor-bearing system (with no cross-coupling added), rotor at threshold of stability (obtained by increasing the cross

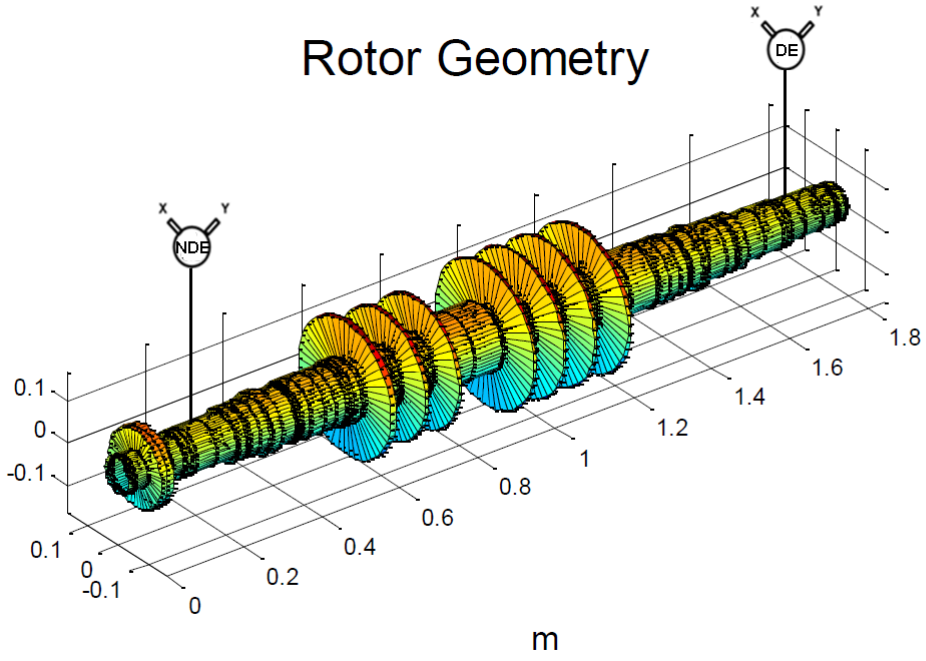

Figure 4.2: Rotor Geometry.

coupling stiffness in the middle of rotor, until threshold was reached) and finally, by a model with high damping (obtained by applying squeeze film damper element in series with the bearing element).

As a basis of comparison to the OMA identification, the modal parameters of the FEM were extracted by writing equation A.1 in state space and solving the eigenproblem for state matrix A in the same manner performed for mass-spring-damper model. The eigenvalues obtained from the model for the first and second under damped modes with backward and forward precession for rotor-bearing model, rotor-bearing with cross coupling stiffness added (stability threshold model) and rotor-bearing-squeeze film damper model are summarized in tables 4.3, 4.4 and 4.5 respectively, where w_n, w_d and ξ are the natural frequency, damped natural frequency and damping ratio respectively.

Table 4.3: Rotor-bearing model eigenvalues.

Mode	First Backward	First Forward	Second Backward	Second Forward
w_n (Hz)	101.8	103.43	361.17	372.66
w_d (Hz)	101.63	103.24	361.11	372.61
ξ	0.05816	0.06127	0.0176	0.0165

Figures 4.4 and 4.5 shows the backward and forward modeshapes for the first and second underdamped modes of the rotor-bearing model, exemplifying modal parameters extraction from the implemented FEM.

To generate synthetic data and apply OMA methods to this data, forced response analysis of the FEM models will be performed, applying different loads excitations

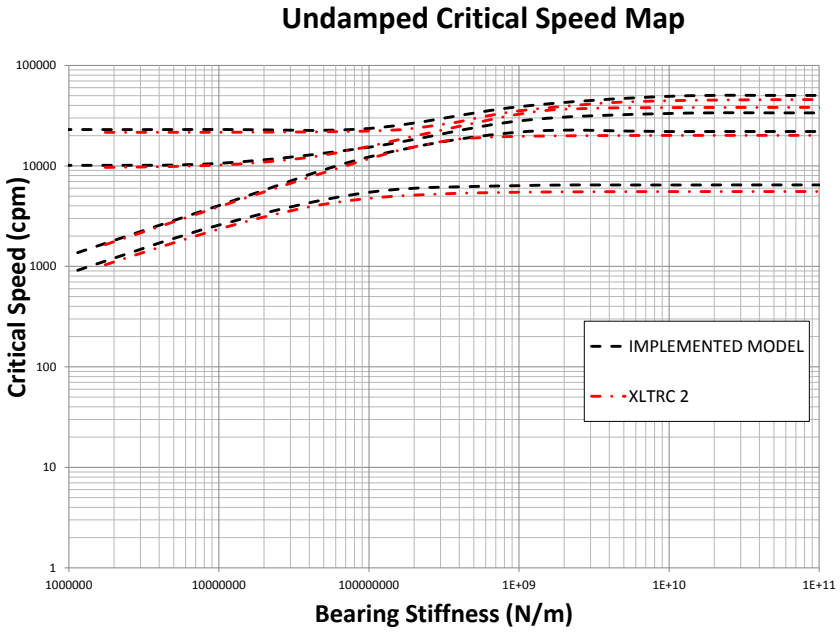

Figure 4.3: Comparison of Undamped Critical Speed Map obtained from the implemented model and from XLTRC2

Table 4.4: Rotor-bearing stability threshold model eigenvalues.

Mode	First Backward	First Forward	Second Backward	Second Forward
w_n (Hz)	102.88	103.146	361.15	372.68
w_d (Hz)	102.178	103.146	361.09	372.625
ξ	0.117	0.0015	0.0189	0.0153

Table 4.5: Rotor-bearing-squeeze film damper model eigenvalues.

Mode	First Backward	First Forward	Second Backward	Second Forward
w_n (Hz)	104.60812	106.4125	367.5315	378.789
w_d (Hz)	102.4372	104.0722793	367.4147	378.6879
ξ	0.2027	0.2086	0.0252	0.023080463

to the models. The goal of the forced response analysis is to simulate the behavior of a compressor in the field, running at its operational speed and subject to fluid flow excitations.

Displacement vibration response at directions named X and Y, with and angle of 90 degrees between them, near the bearing positions (at location where proximity probes would be installed in a real machine) will be the input of OMA methods, aiming to extract the modal parameters under these loads and compare the results with the modal parameters of the FEM. Figure 4.2 shows the position and directions of the displacement vibration responses X and Y for the Drive End (DE) and Non Drive End (NDE) bearings of the compressor model.

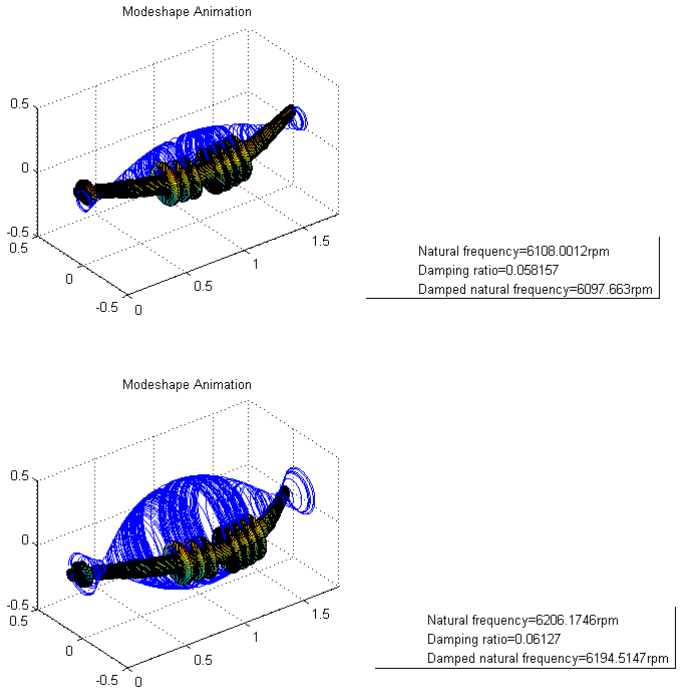

Figure 4.4: Rotor Bearing model. Top: First backward mode shape. Down: First forward mode shape.

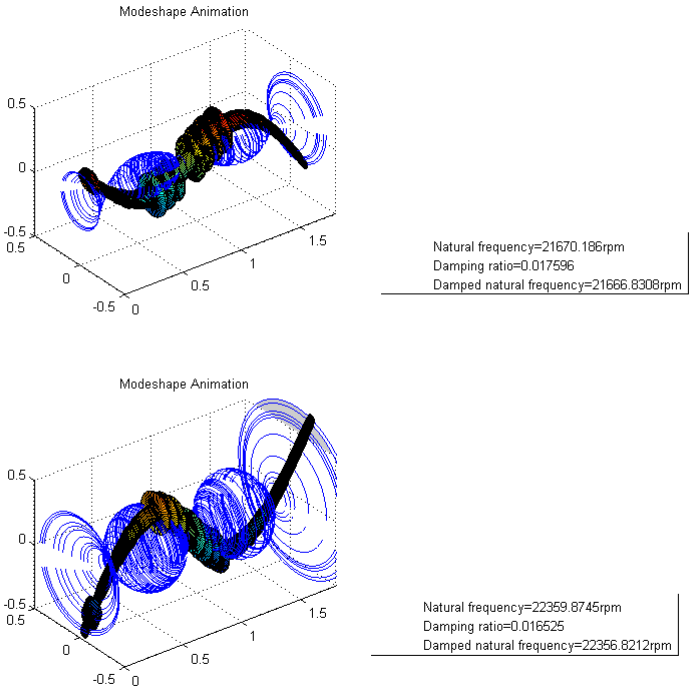

Figure 4.5: Rotor Bearing model. Top: Second backward mode shape. Down: Second forward mode shape.

4.3 Centrifugal Compressor - Machine Overview

Data from four proximity probes located at the bearings of the centrifugal compressor shown in figures 4.6 and 4.7, was collected during 25 minutes in field, with sampling frequency of 128 kHz. This centrifugal compressor recycles a mixture of predominantly hydrogen gas within a Brazilian refinery's URC catalyst reformer unit. This gas is pressurized from approximately 1200 to 2350 kPaG using nine impeller stages with a maximum continuous speed (MCS) of 13,660 rpm, and requiring a 1.6 MW (2,145 hp) electric motor driver. Tilting pad journal bearings with offset pivots support the 300 kg (661 lb_m) rotor assembly. Labyrinth seals are located at the impeller eye, interstage and balance piston locations, while dry gas seals are used for the casing end seals. Additional design information can be found in PETTINATO *et al.* [2].

Figure 4.6: Compressor photo

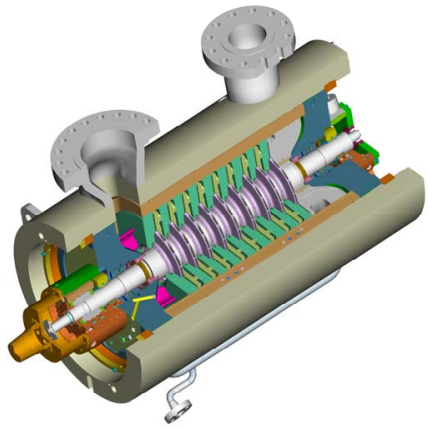

Figure 4.7: Compressor sectional rendering [2]

To avoid any potential shaft whip rotor instability problems in the field, the compressor underwent stability verification testing (SVT) at the manufacturer's facility prior to shipment. This stability testing was required by the end-user's specifications due to the first forward (1F) mode's log decrement being predicted to be below a minimum level. Because the need for an SVT was identified early in the procurement phase, the compressor's outboard, non-drive shaft end was designed with an extension to accommodate a temporarily mounted, electromagnetic shaker for non-synchronous excitation. This shaft extension can be seen at the left of the rotor assembly in Figure 4.7.

High confidence in the resulting stability measurements was obtained through the close correlation between two different excitation/identification processes. One process followed conventional experimental modal analysis methods using an identification technique based on measured frequency response functions. These frequency response functions were acquired by applying stepped-sine excitation from the elec-

tromagnetic shaker.

The second SVT excitation/identification process was performed using the transient free decay of the vibrations as a result of blocking excitation. Originally used for stability testing on a machine by Kanki *et al.* [51], blocking excitation involved tuning the shaker's frequency to excite and isolate the 1F mode (or other), and then suddenly turning the shaker off. Identification was accomplished using a time domain, output-only technique that was originally developed for speech processing applications [26], and later for operational modal analysis HUNG and KO [25]. This technique, multiple output backward autoregression (MOBAR), when used in combination with blocking excitation, had been found to be very reliable and accurate for rotordynamic stability measurements [27].

Four operating conditions were selected for the shop SVTs. To examine the compressor's base stability, where no internal labyrinth seal or impeller aerodynamic dynamic effects would be present, SVTs were conducted under vacuum at 7,900 rpm and MCS. 7,900 rpm was chosen because this was the same speed where an ASME PTC-10 Type II performance test of the compressor was required, using nitrogen (N_2) gas. Stability was measured at two operating conditions during this performance test, one at maximum power and the second near surge. Test stand and project budgetary limitations precluded an ASME PTC-10 Type I test at maximum continuous speed, maximum pressure and power.

Figure 4.8 presents the 1F mode's measured parameters, obtained via blocking and MOBAR, for the four shop SVT operating conditions. Vacuum conditions show a clear decrease in the 1F mode's log decrement going from the performance test speed (7,900 rpm) to maximum continuous speed. The slight increase in the 1F mode's stability going from vacuum to nitrogen gas was a somewhat unexpected outcome for the 7,900 rpm tests. This increase was attributed to either an increase in bearing oil inlet temperature during the course of the test and/or effective damping from the labyrinth seals. However, it was not possible to confirm their relative influence.

The shop SVT measurements and their resulting modeling corrections provided confidence that the compressor would be stable once it reached the field. Under design conditions at MCS, the machine's δ_{1F} was predicted to be 0.12–0.14 using a particular, simplified model correction approach. Therefore, relative to the base stability measured the shop, the 1F stability was expected to remain the same, or slightly increase, when operating in the field. However, another simplified model correction method predicted the δ_{1F} to decrease, but remain stable. Details of the entire shop SVT process, including modeling predictions and corrections, are provided in [2].

Startup of the compressor in 2012 confirmed a stable compressor with no sign

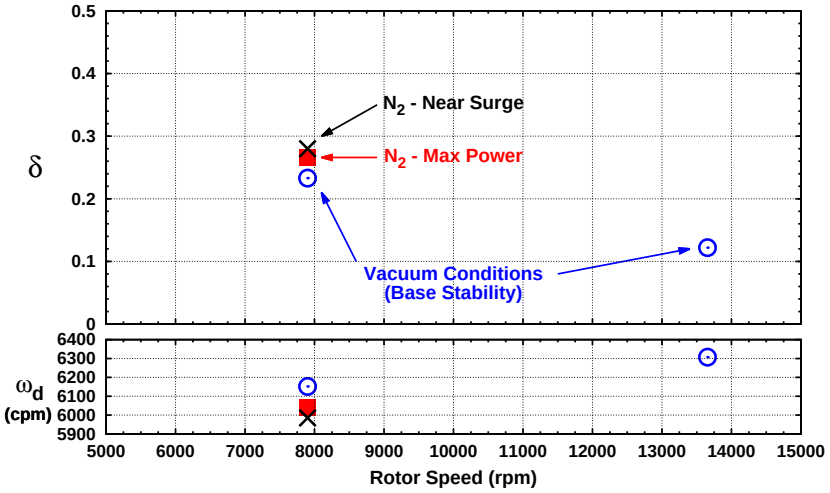

Figure 4.8: 1F mode's measured parameters during shop SVT

of subsynchronous vibration in the proximity displacement probes spectra, except for the electric motor harmonic frequency, an example of which is shown in Figures 4.9 and 4.10.

The absence of any significant subsynchronous vibration does not provide any quantitative measure of the 1F mode's log decrement. It could simply be the result of low ambient gas excitations being present in this hydrogen service, where the average gas density in the compressor is only 5.43 kg/m^3 (0.339 lb$_m$/ft^3). This gas density is understood to be significantly lower than many of the previous investigations when ambient excitations were relied upon for OMA of centrifugal compressors in natural gas services.

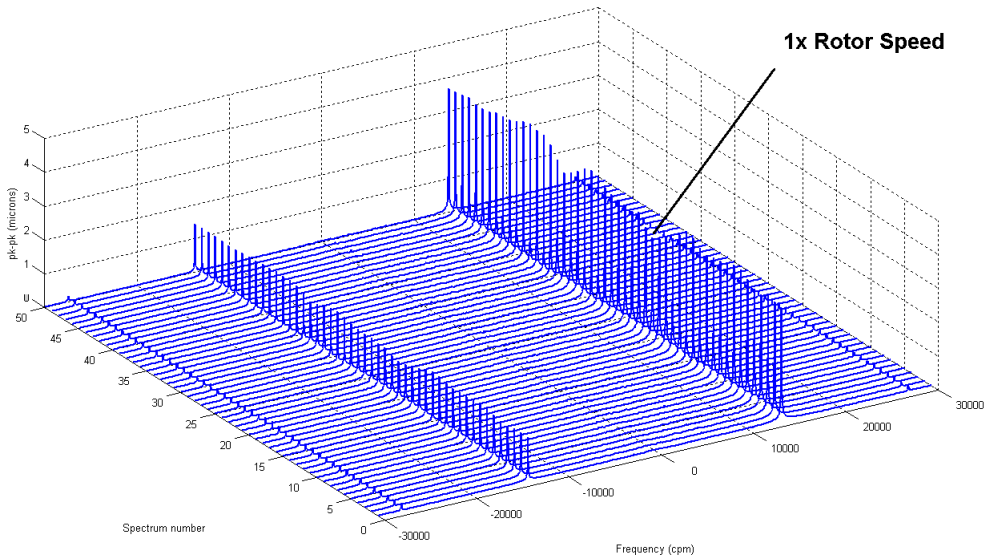

Figure 4.9: Compressor vibrations during field operation at MCS, Non Drive End full spectrum

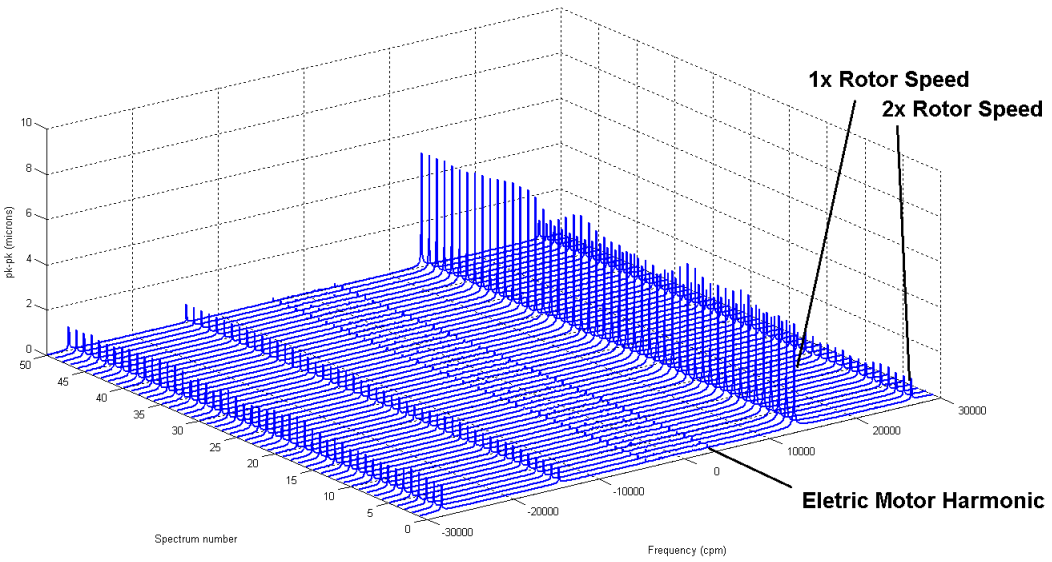

Figure 4.10: Compressor vibrations during field operation at MCS, Drive End full spectrum

Chapter 5

Results and Discussions

5.1 Identification Results

The modal identification was performed using SSI Data Driven (UPC, CVA and PC), SSI Covariance Driven (UPC) and MOBAR methods.

5.1.1 Mass-Spring-Damper model: white noise excitation

White noise excitation was applied to the three masses and uncorrelated noise was added to the obtained response signal. The input of OMA methods was the response in the three masses positions.

The process was repeated several times, each time with a new white noise excitation being applied and a new uncorrelated white noise being added to the obtained system response, in order to allow a Monte Carlo analysis of the damping ratio and natural frequencies identification using different OMA methods (Data Driven SSI-UPC, SSI-CVA, SSI-PC, Covariance Driven SSI-UPC and MOBAR).

The sampling frequency adopted in this discrete model was 400 Hz and each Monte Carlo run was performed with 2 minutes of response data obtained from the Mass-Spring-Damper model. Two levels of SNR were adopted for the mass-spring-damper model, being SNR 10 and SNR 2, aiming to verify the influence of uncorrelated noise in modal parameters extraction with different methods.

Figure 5.1 shows an example of time domain response for node 1 with uncorrelated noise added resulting in a SNR of 10 and without uncorrelated noise added, while figure 5.2 shows the same example for SNR 2.

As stated at Chapter 3, the spectral densities matrix of responses is closely related with the system frequency response function matrix, containing the information about the system dynamics.

Performing a singular value decomposition of the outputs spectral densities matrix, can bring some useful information about the natural frequencies from the sys-

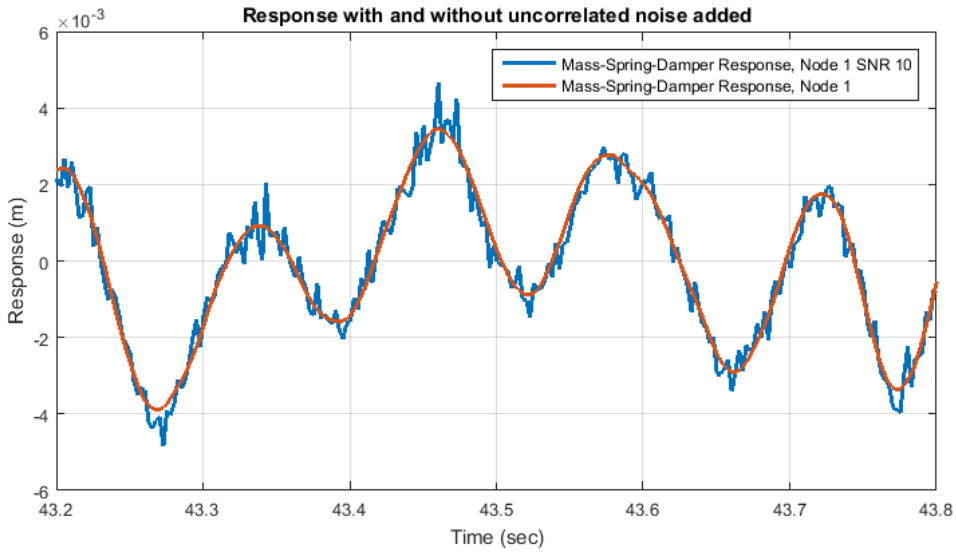

Figure 5.1: Response at Node 1 with and without uncorrelated noise added, SNR 10.

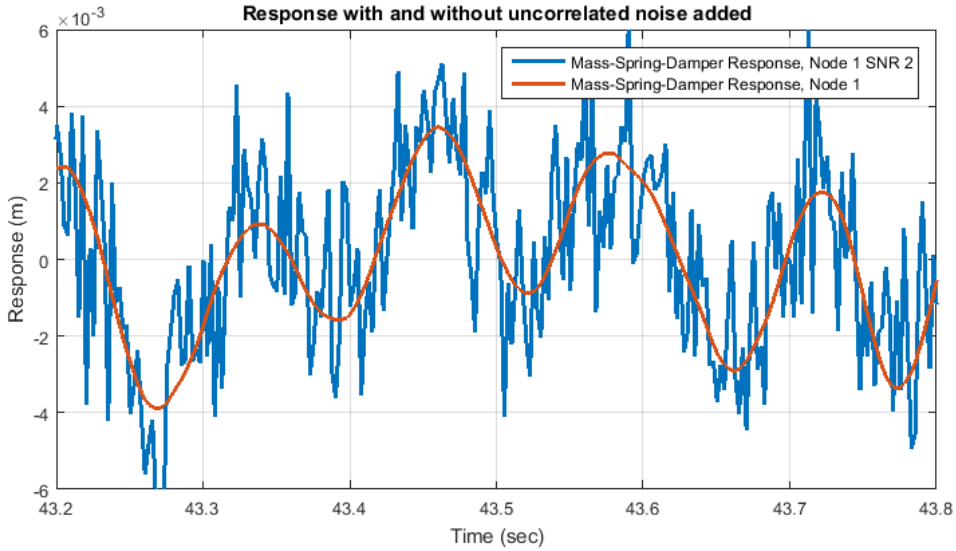

Figure 5.2: Response at Node 1 with and without uncorrelated noise added, SNR 2.

tem, prior to perform modal parameters extraction through the analyzed methods. It is a common practice to plot the resulting singular values and to compare the frequencies where these singular values present peaks, with the natural frequencies identified by OMA methods.

Figure 5.3 shows singular values (σ) of spectral densities plot, generated with one realization of response data from the mass-spring-damper model, with SNR 10.

From this figure, the modulation of first singular value in the damped natural frequencies of the three modes of the model can be clearly observed. This singular value contain information about the mode with higher energy in each frequency. The dashed lines shown in this figure, allows one to observe how each mode is

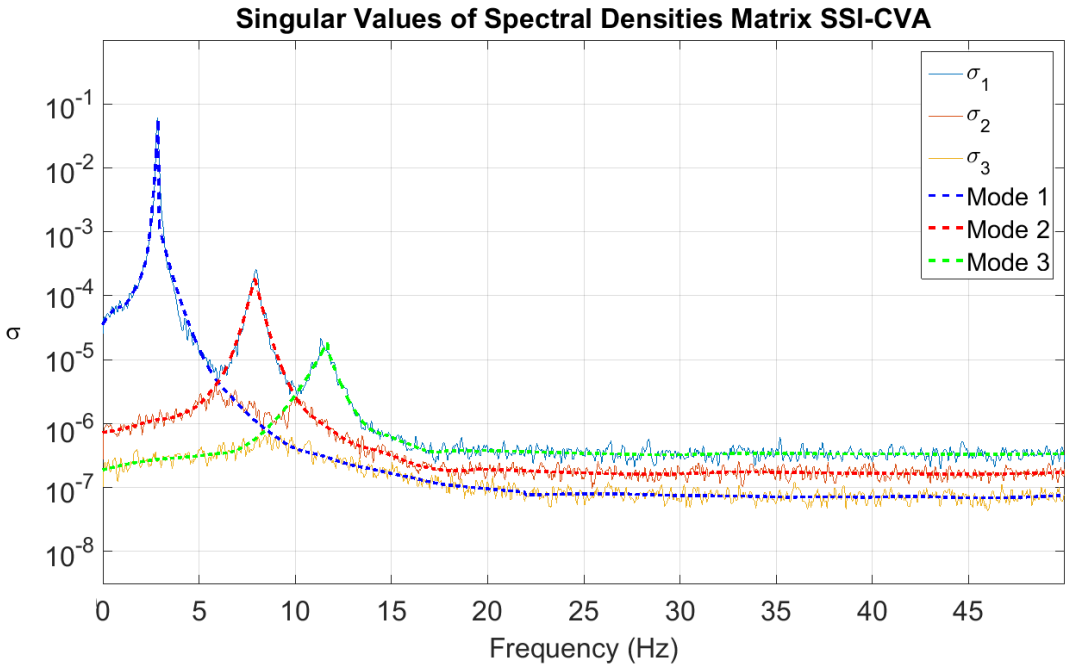

Figure 5.3: Singular values of spectral densities matrix, SNR 10.

distributed from the first to the last singular value, according to its participation in the responses at each frequency.

First singular value present a modulation from 0 to 7 Hz, with a peak near to 3 Hz, containing the information about the first mode in this range.

It can be observed that the modulation of second singular value increases when frequency is increased from 0 to 7 Hz. In this range the second singular value contains the information of the second mode. After this frequency the second mode has more energy than the first mode, thus the first singular value starts to reflect the second mode while the first mode influence begins to be reflected by the second singular value.

The third mode moves from the third singular value to the second near to 8 Hz and moves from the second singular value to the first after the frequency of 10 Hz, while the first mode moves from the second to the third singular value in 8 Hz.

This is a physical interpretation of singular values of spectral densities matrix plot, that can be observed when damping is low or moderate. The dashed lines in figure 5.3 were drawn to better illustrate this interpretation.

Figure 5.4 shows a stabilization diagram over the singular values plot shown in figure 5.3. This stabilization diagram allows one to observe the damped natural frequencies identified by applying the method SSI-CVA with model order varying from 5 to 50. The input dataset used was the same adopted to calculate the singular values plot already discussed. A match between the first singular values peaks and the identified damped natural frequencies can be clearly noted.

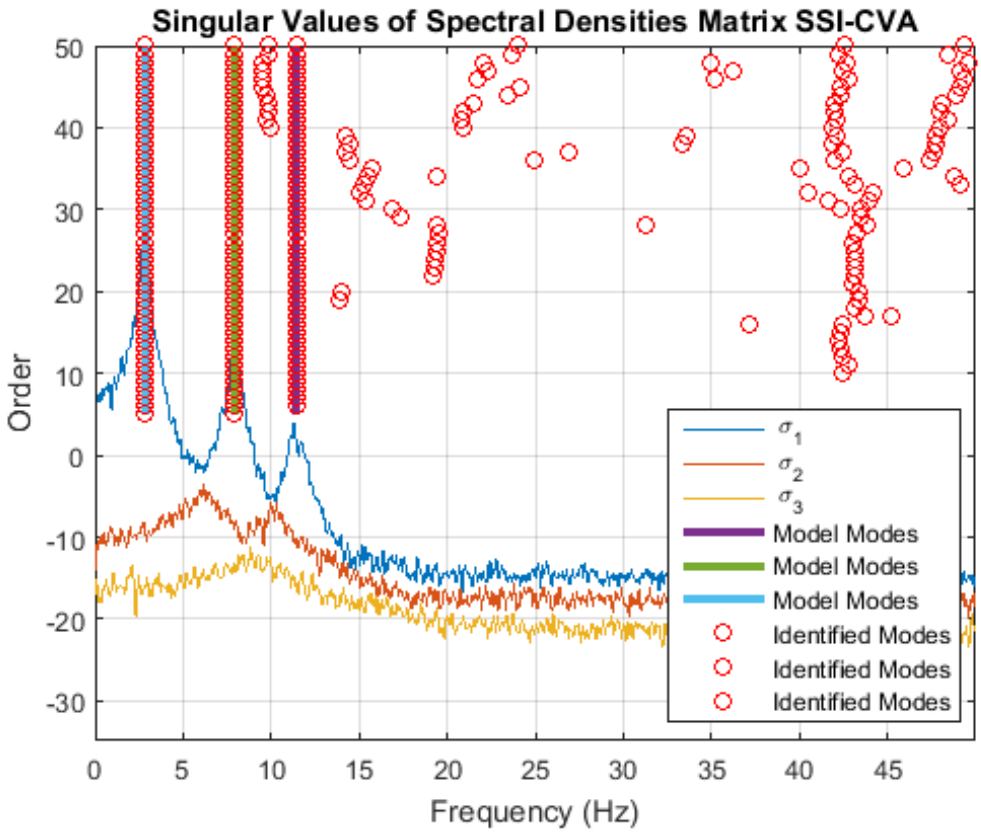

Figure 5.4: Singular Values of Spectral Densities and stabilization diagram.

It can be observed in this stabilization diagram, that even for white noise excitation, computational modes can be identified and should be recognized. A common practice to eliminate computational modes, adopted in the present work is to verify if the identified mode has stable frequencies, damping ratio and modeshapes (by using Modal Assurance Criteria MAC) between the different model orders. For the mass-spring-damper identification, modes with a deviation of more than 0.5 percent at the identified frequencies, a deviation of more than 5 percent at the identified damping ratio or a MAC lower than 0.98 between the orders, were considered unstable. Figure 5.5 shows the stabilization diagram after applying these filters. It can be observed that all the computational modes shown in Figure 5.4 were eliminated. Further discussion on this subject will be presented at the Identification from the FEM model.

Figures 5.6 and 5.7 presents box plots with damped natural frequencies and damping ratio respectively, identified from the 100 Monte Carlo runnings for a SNR of 10, using SSI-CVA, SSI-PC, SSI-UPC, MOBAR and SSI-UPC Cov.

On each box, the central mark indicates the median, and the bottom and top edges of the box indicate the 25^{th} and 75^{th} percentiles, respectively. The whiskers extend to the most extreme data points not considered outliers, and the outliers are plotted individually using the '+' symbol.These box plots allows a better comparison

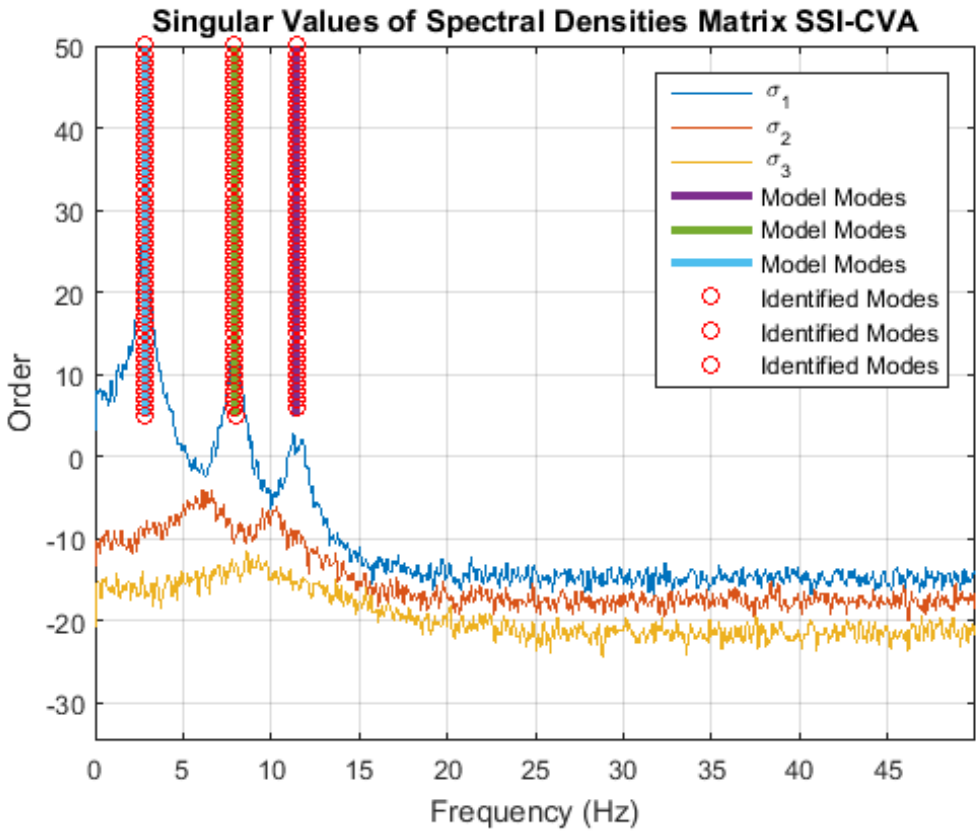

Figure 5.5: Singular Values of Spectral Densities and stabilization diagram showing stable modes.

between the estimation provided by the methods analyzed in this work.

Tables 5.1, 5.2, 5.3, 5.4 and 5.5 summarizes the modal parameters extracted, from the 100 Monte Carlo runnings for a SNR of 10, as the mean values (μ) and also presents the standard deviation σ of the identified parameters as a percentage of its mean values, without excluding the outliers. It is worth notice that the same symbol σ is being used to represent singular values and standard deviation, but the reader can easily identify which one is being referred to, along the text.

It is possible to observe a good agreement in the mean and median values of damped natural frequency and damping ratio identified for the three modes, with all the studied methods.

The standard deviation for the natural frequencies is very low, but is considerable for damping ratio estimation.

This meaningful standard deviation for damping ratio allied to a mean value that tend to the real value suggests that many realizations of damping estimation or a higher time span are necessary in order to have good confidence. This can be performed by acquiring data from a long period and splitting the data to perform several identifications or using the long period data to perform one identification run. Some applications can lead to computational limitations when choosing the

last option, once the Hankel matrices will present considerable size, thus splitting the data and performing several identifications is a good solution if computational resources are limited.

Figures 5.8, 5.9, 5.10, 5.12 and 5.11, allows a visual inspection of the spread of natural frequencies and damping ratio obtained from the Monte Carlo runnings for SSI-UPC, CVA, PC, MOBAR and Cov-SSI with SNR 10 respectively. It is worth notice that the outliers were not eliminated in these figures.

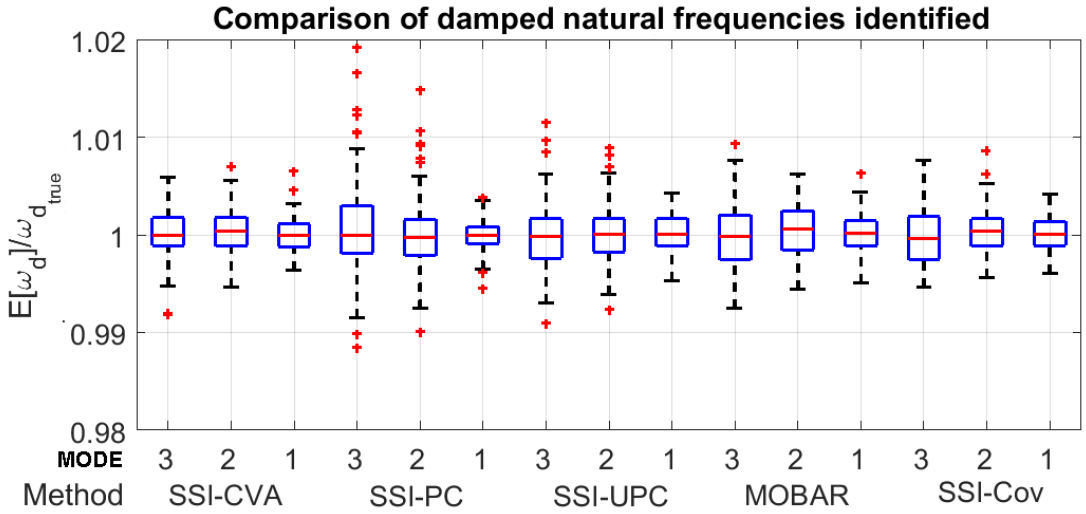

Figure 5.6: Box plot of identified damped natural frequencies for the mass-spring-damper model with SNR 10.

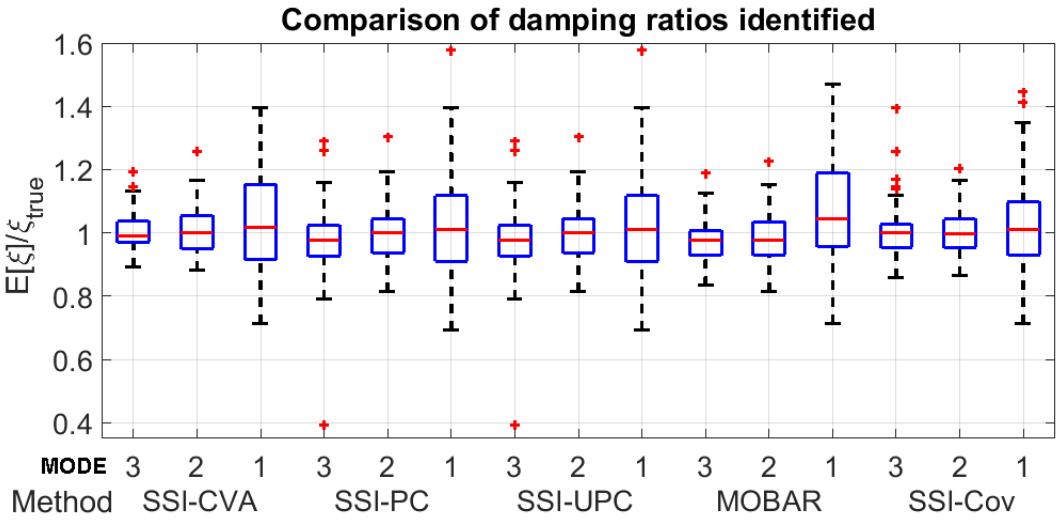

Figure 5.7: Box plot of identified damping ratios for the mass-spring-damper model with SNR 10.

Table 5.1: System eigenvalues identified by SSI-UPC method, SNR 10.

Mode	First	Second	Third
$\mu(w_n)$ (Hz)	2.8337	7.9402	11.4677
$\sigma(w_n)$ (%)	0.1834	0.2742	0.3468
$error(\mu(w_n))$ (%)	0.02	0.02	-0.03
$\mu(w_d)$ (Hz)	2.8335	7.9363	11.4565
$\sigma(w_d)$ (%)	0.1831	0.2748	0.3418
$error(\mu(w_d))$ (%)	0.02	0.02	-0.03
$\mu(\xi)$	0.0113	0.0311	0.0439
$\sigma(\xi)$ (%)	15.51	8.44	10.59
$error(\mu(\xi))$ (%)	2.14	-0.3	-2.47

Table 5.2: System eigenvalues identified by SSI-PC method, SNR 10.

Mode	First	Second	Third
$\mu(w_n)$ (Hz)	2.8329	7.9381	11.4799
$\sigma(w_n)$ (%)	0.1690	0.3829	0.4960
$error(\mu(w_n))$ (%)	-0.01	-0.01	0.07
$\mu(w_d)$ (Hz)	2.8327	7.9340	11.4684
$\sigma(w_d)$ (%)	0.1687	0.3853	0.4939
$error(\mu(w_d))$ (%)	-0.01	-0.01	0.07
$\mu(\xi)$	0.0113	0.0317	0.0448
$\sigma(\xi)$ (%)	13.01	11.82	12.28
$error(\mu(\xi))$ (%)	1.55	1.58	-1.15

Table 5.3: System eigenvalues identified by SSI-CVA method, SNR 10.

Mode	First	Second	Third
$\mu(w_n)$ (Hz)	2.8333	7.9419	11.4717
$\sigma(w_n)$ (%)	0.1717	0.2176	0.2446
$error(\mu(w_n))$ (%)	0.00	0.04	0.00
$\mu(w_d)$ (Hz)	2.8331	7.9379	11.46
$\sigma(w_d)$ (%)	0.1711	0.2159	0.2468
$error(\mu(w_d))$ (%)	0.00	0.04	0.00
$\mu(\xi)$	0.0115	0.0314	0.0451
$\sigma(\xi)$ (%)	15.53	6.89	5.66
$error(\mu(\xi))$ (%)	3.38	0.76	0.27

Table 5.4: System eigenvalues identified by Covariance Driven SSI-UPC method, SNR 10.

Mode	First	Second	Third
$\mu(w_n)$ (Hz)	2.8339	7.9374	11.4670
$\sigma(w_n)$ (%)	0.1842	0.2523	0.2769
$error(\mu(w_n))$ (%)	0.02	-0.01	0.04
$\mu(w_d)$ (Hz)	2.8334	7.9336	11.4555
$\sigma(w_d)$ (%)	0.1845	0.2534	0.2786
$error(\mu(w_d))$ (%)	0.01	-0.01	0.04
$\mu(\xi)$	0.0114	0.0310	0.0448
$\sigma(\xi)$ (%)	14.09	7.07	5.97
$error(\mu(\xi))$ (%)	2.70	-0.64	-0.44

Table 5.5: System eigenvalues identified by MOBAR method, SNR 10.

Mode	`First`	`Second`	`Third`
$\mu(w_n)$ (Hz)	2.8335	7.9425	11.4715
$\sigma(w_n)$ (%)	0.2055	0.2712	0.3347
$error(\mu(w_n))$ (%)	0.01	0.05	-0.03
$\mu(w_d)$ (Hz)	2.833	7.9347	11.4598
$\sigma(w_d)$ (%)	0.2056	0.2711	0.3363
$error(\mu(w_d))$ (%)	0.01	0.05	-0.02
$\mu(\xi)$	0.01192	0.0306	0.0437
$\sigma(\xi)$ (%)	14.08	7.6	6.69
$error(\mu(\xi))$ (%)	7.42	-1.76	-2.88

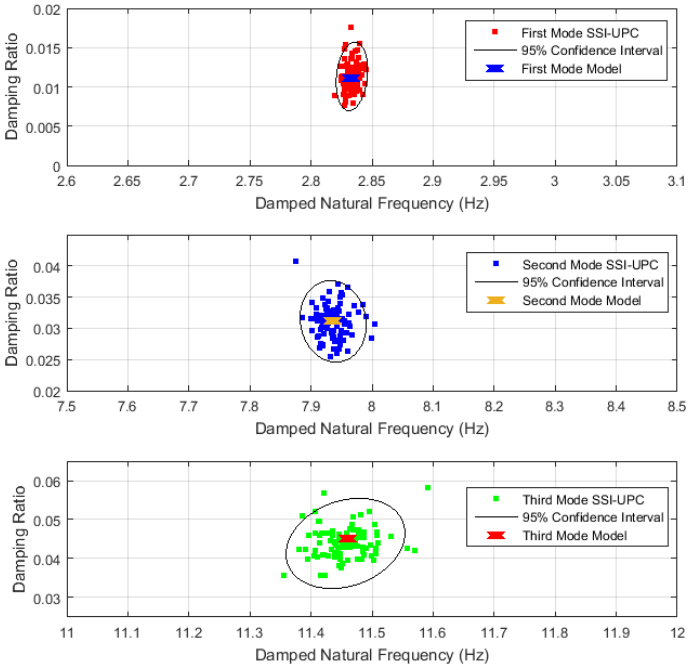

Figure 5.8: Damped Natural Frequency and Damping Ratio identification through SSI-UPC method in 100 Monte Carlo runnings with SNR 10.

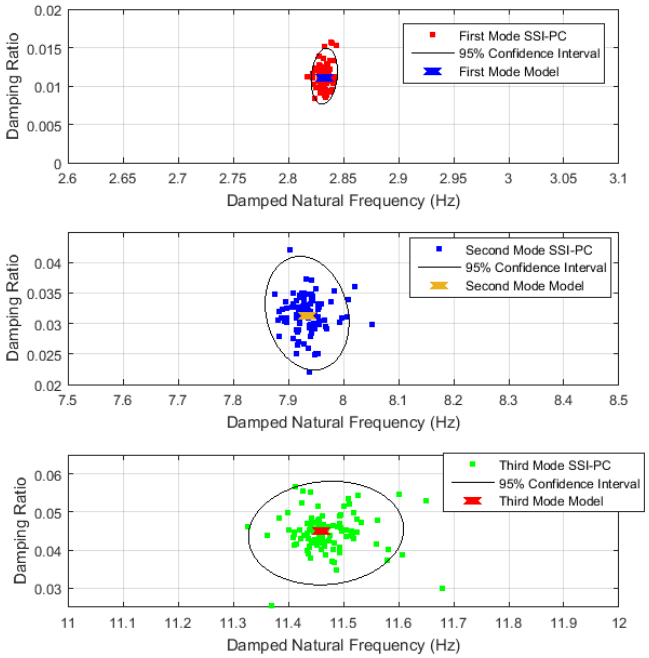

Figure 5.9: Damped Natural Frequency and Damping Ratio identification through SSI-PC method in 100 Monte Carlo runnings with SNR 10.

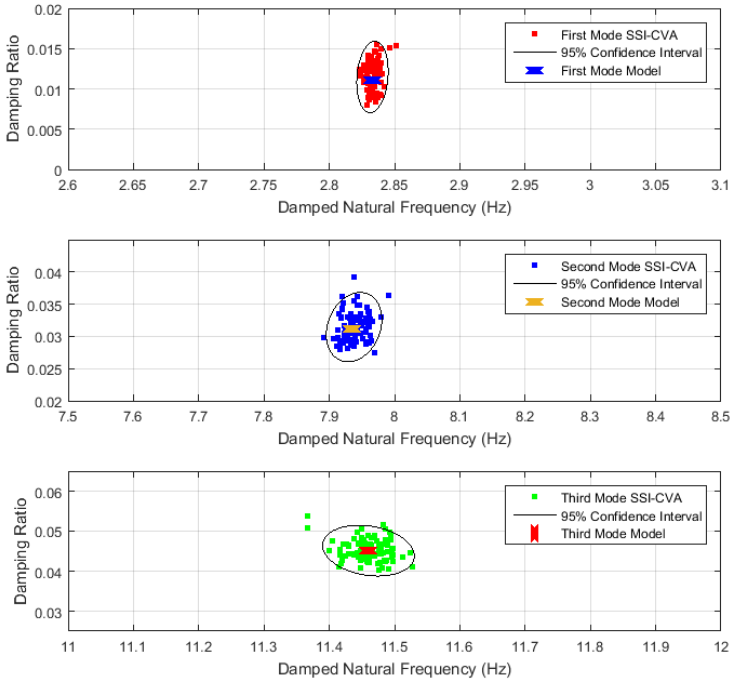

Figure 5.10: Damped Natural Frequency and Damping Ratio identification through SSI-CVA method in 100 Monte Carlo runnings with SNR 10.

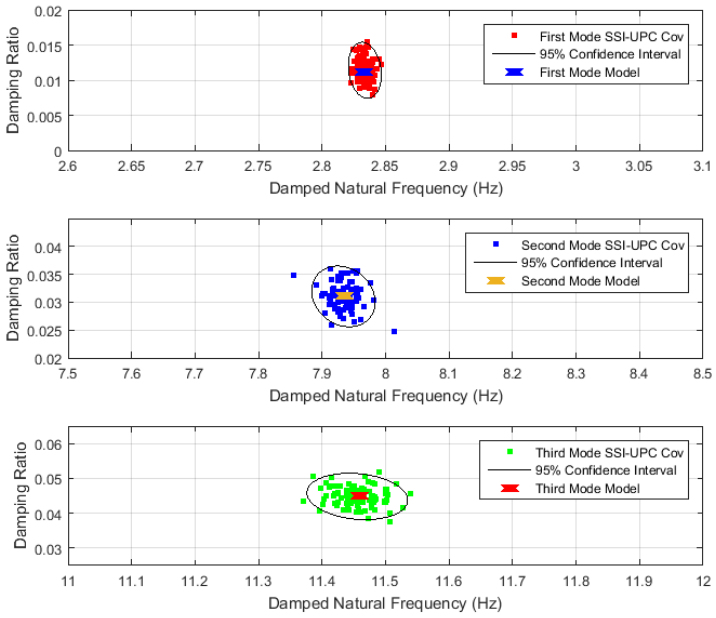

Figure 5.11: Damped Natural Frequency and Damping Ratio identification through SSI-UPC cov method in 100 Monte Carlo runnings with SNR 10.

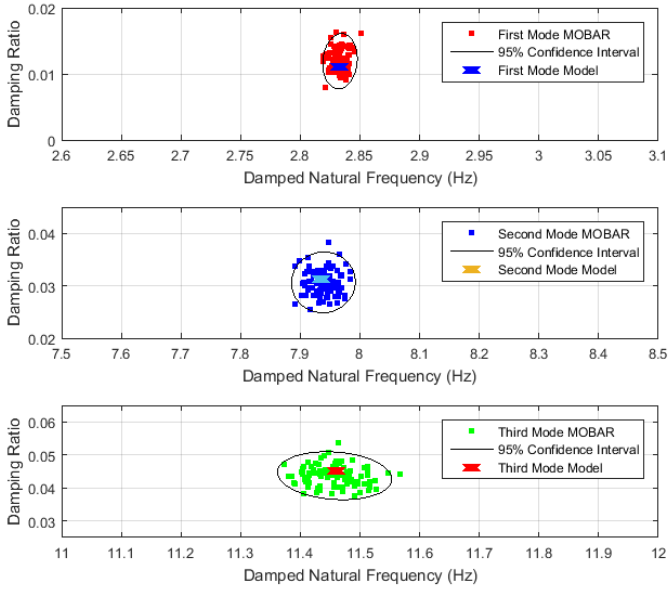

Figure 5.12: Damped Natural Frequency and Damping Ratio identification through MOBAR method in 100 Monte Carlo runnings with SNR 10.

Regarding the Monte Carlo runs with SNR 2, figures 5.13 and 5.14 presents box plots with damped natural frequencies and damping ratio respectively.

To allow a better comparison between the identification performed with synthetic data generated with SNR 10 and SNR 2, the box plots already presented were

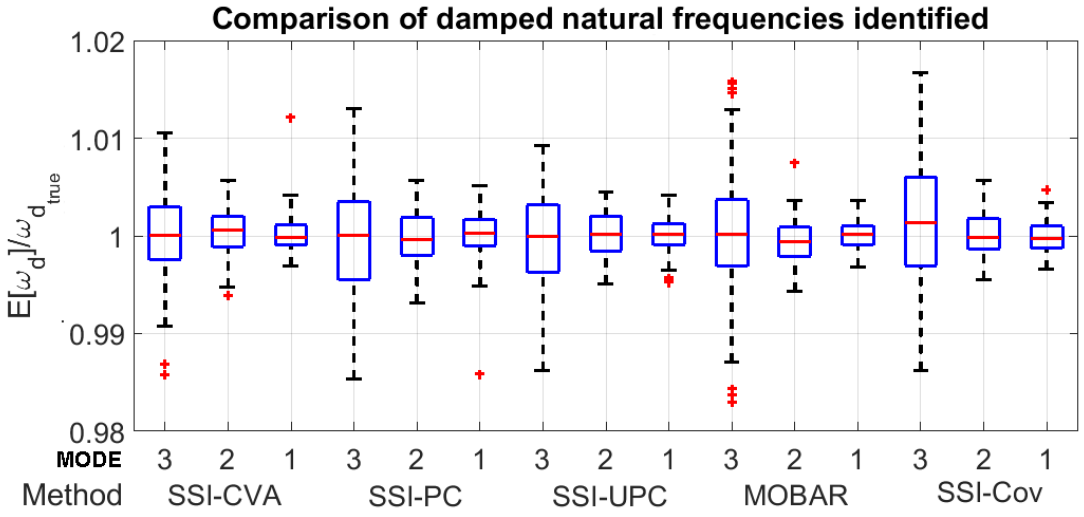

Figure 5.13: Box plot of identified damped natural frequencies for the mass-spring-damper model with SNR 2.

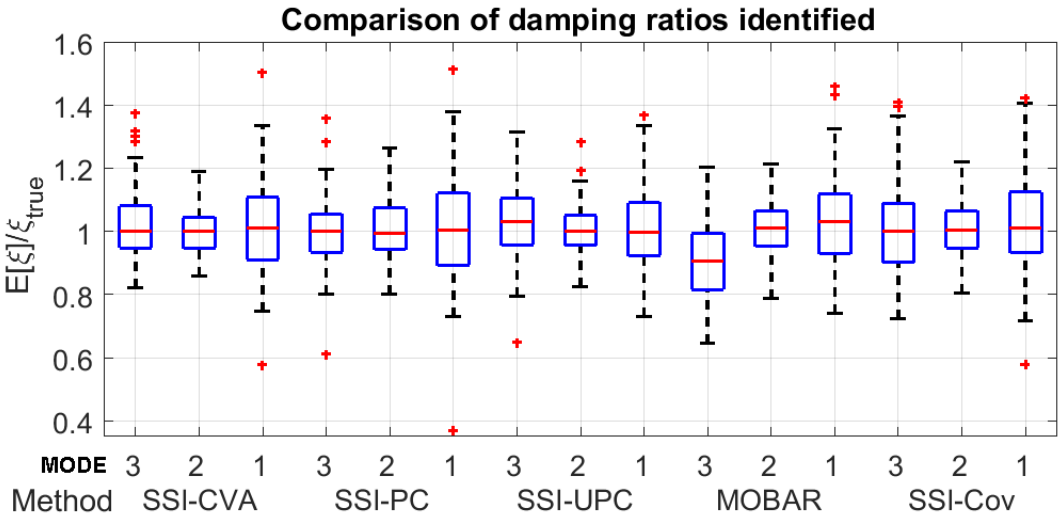

Figure 5.14: Box plot of identified damping ratios for the mass-spring-damper model with SNR 2.

compiled side by side in figures 5.15, 5.16, 5.17 and 5.18.

From these figures, it can be clearly observed that reducing the SNR to 2, has not affected meaningfully the median value and the spread of natural frequencies and damping ratio identified by the analyzed methods. This fact shows the robustness of studied methods to deal with noisy signals.

Moreover, from these comparisons it was not possible to identify a method that is outstanding compared with the others. The structural modes were identified by all of the studied methods, highlighting that performing OMA identification by more than one method and finding similar modal parameters, can give further confidence at the identification being performed.

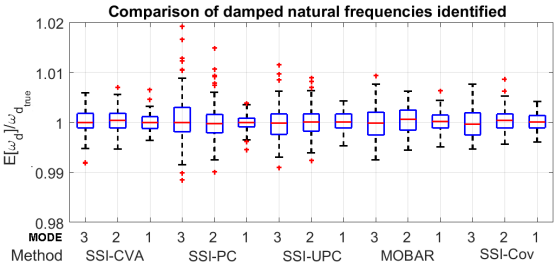

Figure 5.15: Box plot ω_d, SNR 10.

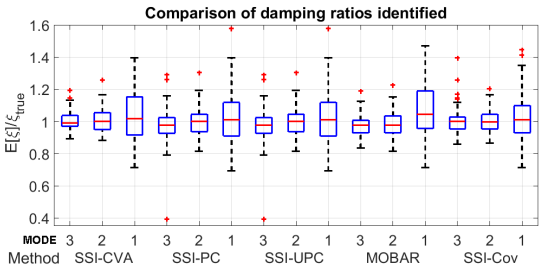

Figure 5.16: Box plot ξ, SNR 10.

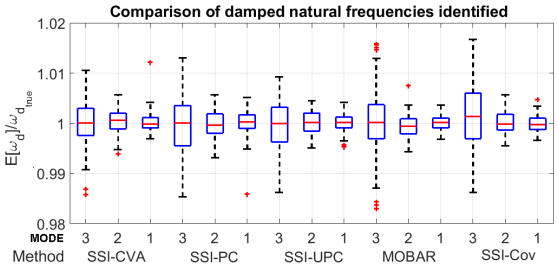

Figure 5.17: Box plot ω_d, SNR 2.

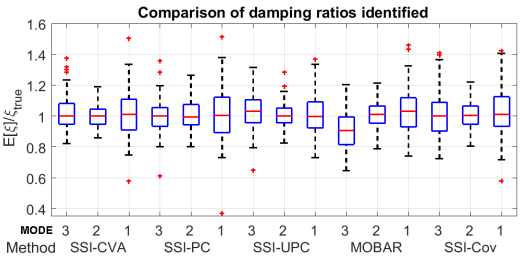

Figure 5.18: Box plot ξ, SNR 2.

Additionally, tables 5.6, 5.7, 5.8, 5.9 and 5.10 summarizes the modal parameters extracted as the mean values (μ) of 100 Monte Carlo runnings for a SNR of 2, and also presents the standard deviation σ of the identified parameters as a percentage of its mean values, without excluding the outliers. It is possible to see a good agreement with the model table 4.2.

The fact that the median values from the box plots and the mean values from the result tables agrees, suggests that the identification errors along the Monte Carlo runnings do not have a skew distribution.

Figures 5.19, 5.20, 5.21, 5.22 and 5.23 allows a visual inspection of the spread of natural frequencies and damping ratio obtained from the Monte Carlo runnings for SSI-UPC, CVA, PC, SSI-UPC Cov and MOBAR with SNR 2 respectively.

The last verification performed with synthetic data generated by the application of white noise excitations to the mass-spring-damper model, was to increase the time span of each Monte Carlo run to 12 minutes, keeping a SNR of 2.

Table 5.11 and figure 5.24 shows the results obtained from SSI-CVA method. It is worth notice that increasing the acquisition time span has meaningfully reduced the spread of modal parameters identified, even with this low SNR. This fact was expected, once for the analyzed time domain methods, increasing the time span allows a more accurate estimate of correlation functions for covariance driven methods and data projections that leads to a better estimate of observability matrix at data driven methods (see Chapter 3).

Table 5.6: System eigenvalues identified by SSI-UPC method, SNR 2.

Mode	First	Second	Third
$\mu(w_n)$ (Hz)	2.8336	7.9398	11.4684
$\sigma(w_n)$ (%)	0.1824	0.2237	0.4737
$error(\mu(w_n))$ (%)	0.01	0.02	-0.03
$\mu(w_d)$ (Hz)	2.8334	7.9359	11.456
$\sigma(w_d)$ (%)	0.1804	0.2234	0.4782
$error(\mu(w_d))$ (%)	0.01	0.02	-0.03
$\mu(\xi)$	0.0111	0.03125	0.0463
$\sigma(\xi)$ (%)	13.22	8.075	11.06
$error(\mu(\xi))$ (%)	0.07	0.15	2.88

Table 5.7: System eigenvalues identified by SSI-PC method, SNR 2.

Mode	First	Second	Third
$\mu(w_n)$ (Hz)	2.8337	7.9370	11.4691
$\sigma(w_n)$ (%)	0.1690	0.2508	0.5335
$error(\mu(w_n))$ (%)	0.02	-0.02	-0.02
$\mu(w_d)$ (Hz)	2.8335	7.9331	11.4574
$\sigma(w_d)$ (%)	0.2467	0.2516	0.5316
$error(\mu(w_d))$ (%)	0.02	-0.02	-0.02
$\mu(\xi)$	0.0112	0.0315	0.0451
$\sigma(\xi)$ (%)	17.38	9.06	10.12
$error(\mu(xi))$ (%)	1.22	0.9	0.15

Table 5.8: System eigenvalues identified by SSI-CVA method, SNR 2.

Mode	First	Second	Third
$\mu(w_n)$ (Hz)	2.8335	7.9419	11.4751
$\sigma(w_n)$ (%)	0.1909	0.2332	0.4346
$error(\mu(w_n))$ (%)	0.01	0.04	0.03
$\mu(w_d)$ (Hz)	2.8333	7.938	11.463
$\sigma(w_d)$ (%)	0.1911	0.2335	0.4357
$error(\mu(w_d))$ (%)	0.01	0.04	0.03
$\mu(\xi)$	0.0111	0.0313	0.0458
$\sigma(\xi)$ (%)	15.62	7.33	10.38
$error(\mu(\xi))$ (%)	0.68	0.19	1.87

Table 5.9: System eigenvalues identified by Covariance Driven SSI-UPC method, SNR 2.

Mode	First	Second	Third
$\mu(w_n)$ (Hz)	2.8330	7.9403	11.4802
$\sigma(w_n)$ (%)	0.1955	0.2227	0.5580
$error(\mu(w_n))$ (%)	0.01	0.02	0.08
$\mu(w_d)$ (Hz)	2.8328	7.9363	11.4677
$\sigma(w_d)$ (%)	0.1955	0.2225	0.5595
$error(\mu(w_n))$ (%)	0.01	0.02	0.08
$\mu(\xi)$	0.0115	0.0314	0.04612
$\sigma(\xi)$ (%)	15.18	7.83	14.76
$error(\mu(w_n))$ (%)	3.6	0.64	0.27

Table 5.10: System eigenvalues identified by MOBAR method.

Mode	First	Second	Third
$\mu(w_n)$ (Hz)	2.8327	7.9405	11.4272
$\sigma(w_n)$ (%)	0.1751	0.2431	0.2938
$error(\mu(w_n))$ (%)	0.01	0.05	-0.01
$\mu(w_d)$ (Hz)	2.8325	7.9365	11.4114
$\sigma(w_d)$ (%)	0.1749	0.243	0.2966
$error(\mu(w_d))$ (%)	0.01	0.06	-0.01
$\mu(\xi)$	0.0117	0.0317	0.0524
$\sigma(\xi)$ (%)	14.06	8.06	7.55
$error(\mu(w_n))$ (%)	2.74	0.79	-9.81

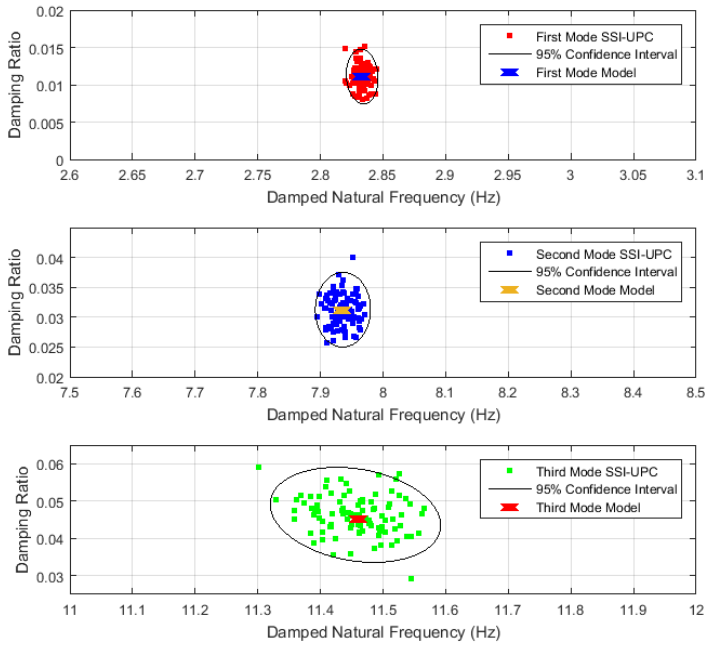

Figure 5.19: Damped Natural Frequency and Damping Ratio identification through SSI-UPC method in 100 Monte Carlo runnings with SNR 10.

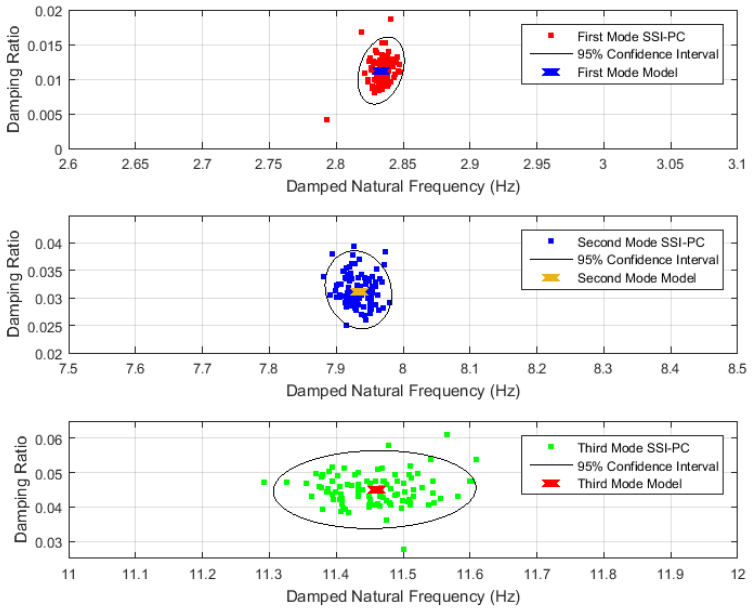

Figure 5.20: Damped Natural Frequency and Damping Ratio identification through SSI-PC method in 100 Monte Carlo runnings with SNR 2.

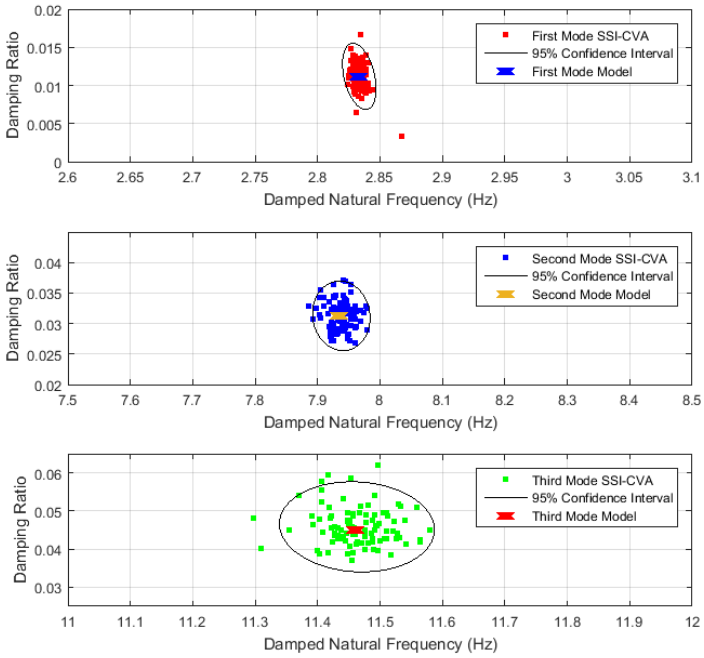

Figure 5.21: Damped Natural Frequency and Damping Ratio identification through SSI-CVA method in 100 Monte Carlo runnings with SNR 2.

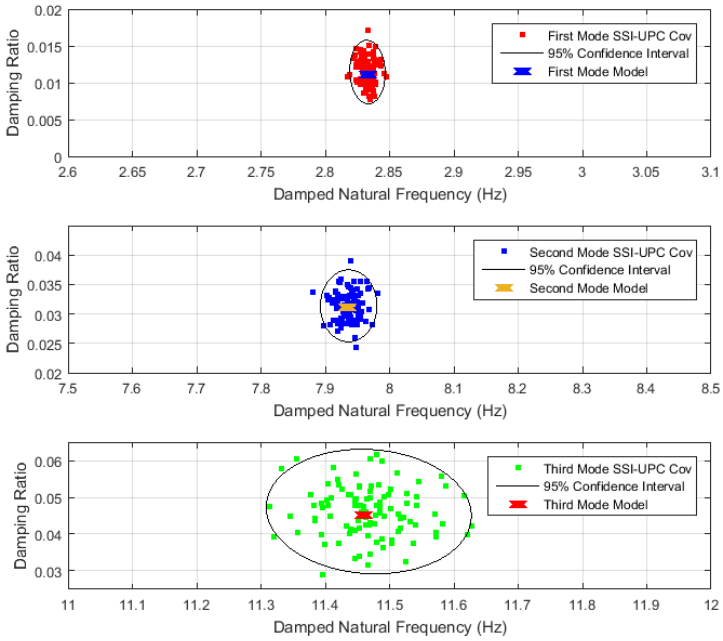

Figure 5.22: Damped Natural Frequency and Damping Ratio identification through SSI-UPC cov method in 100 Monte Carlo runnings with SNR 2.

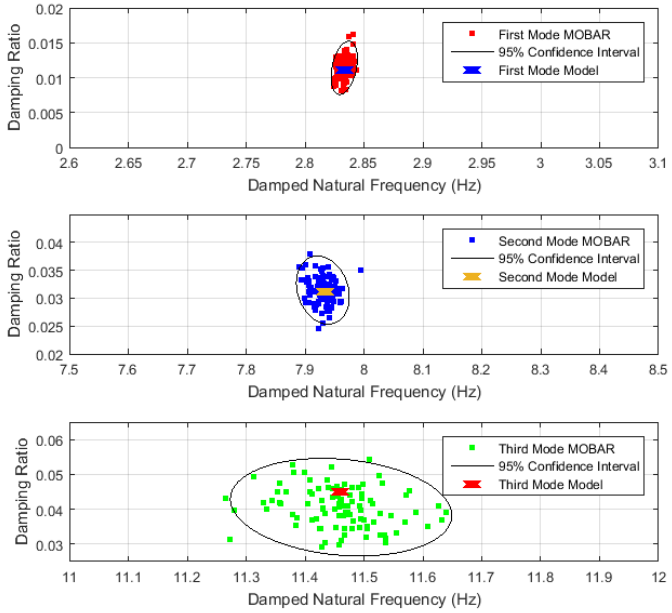

Figure 5.23: Damped Natural Frequency and Damping Ratio identification through MOBAR method in 100 Monte Carlo runnings with SNR 2.

Table 5.11: System eigenvalues identified by SSI-CVA method, SNR 2, 12 minutes of data acquired.

Mode	`First`	`Second`	`Third`
$\mu(w_n)$ (Hz)	2.8331	7.9382	11.4715
$\sigma(w_n)$ (%)	0.068	0.08	0.177
$error(\mu(w_n))$ (%)	0.00	0.00	0.01
$\mu(w_d)$ (Hz)	2.8329	7.9343	11.4611
$\sigma(w_d)$ (%)	0.068	0.08	0.1786
$error(\mu(w_d))$ (%)	0.00	0.00	0.01
$\mu(\xi)$	0.0113	0.0311	0.0439
$\sigma(\xi)$ (%)	5.14	2.59	3.95
$error(\mu(\xi))$ (%)	-0.21	0.44	0.35

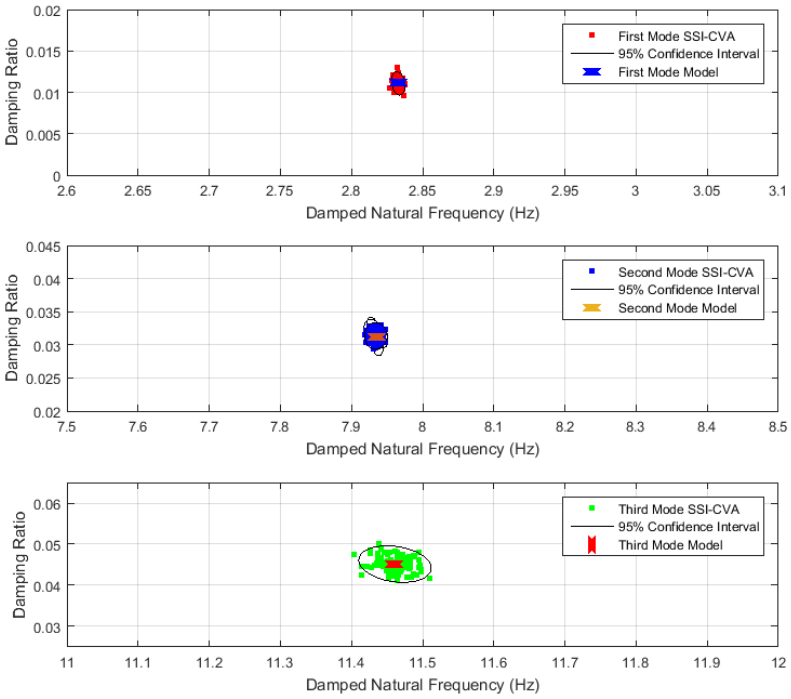

Figure 5.24: Damped Natural Frequency and Damping Ratio identification through SSI-CVA method in 100 Monte Carlo runnings with SNR 2, 12 minutes of data acquired.

5.1.2 Mass-Spring-Damper model: colored noise excitation

To verify the influence of colored noise excitation on the identification of Mass-Spring-Damper modal parameters through the OMA methods studied at the present work, pink, red, blue and violet noise excitations were applied to the three masses.

Uncorrelated white noise was added to the obtained response signal and the input to OMA methods was the displacement responses at the three masses positions as described in the previous section.

Pink noise is defined as a signal with its power spectral density decreasing by 3 dB per octave (density proportional to $1/f$). The PSD of pink noise excitation applied to the mass-spring-damper model is shown in Figure 5.26.

Red noise is defined as a signal with its power density decreasing 6 dB per octave with increasing frequency (density proportional to $1/f^2$). The PSD of red noise excitation applied to the mass-spring-damper model is shown in Figure 5.27.

Blue noise is defined as a signal with its power spectral density increasing 3 dB per octave with increasing frequency (density proportional to f). The PSD of blue noise excitation applied to the mass-spring-damper model is shown in Figure 5.28.

Violet noise is defined as a signal with its power spectral density increasing 6 dB per octave with increasing frequency (density proportional to f^2). The PSD of violet noise excitation applied to the mass-spring-damper model is shown in Figure 5.29.

The stability diagram ploted over sigular values of Spectral Densities Matrix for one realization with pink noise, red noise, blue noise and violet noise excitations is shown in figures 5.30, 5.31, 5.32 and 5.33 respectively. Uncorrelated white noise with SNR 2 was added to the response signals.

Figure 5.34, 5.35, 5.36 and 5.37 shows the results of 100 Monte Carlo simulations, with identification performed through SSI-CVA method.

Once pink and red noise excitations have the characteristics of energy decreasing with frequency, while blue and violet noise excitations have the opposite characteristics, it is possible to notice a lower participation of second and third modes at the Singular Value of Spectral Densities plots for pink and red noise excitation compared with blue and violet noise excitations.

For red noise the energy exciting the third mode is so low, that response is lower than the uncorrelated noise added, thus it was not possible to identify the modal parameters of this mode. Also, the second mode identified have presented a meaningful spread.

This fact illustrates well that OMA methods require enough bandwidth to excite the mode of interest, allied to good SNR at this bandwidth in order to allow a good identification.

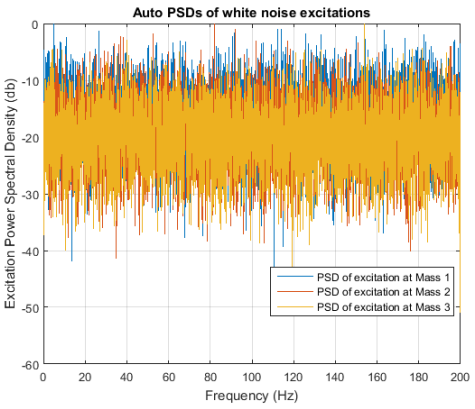

Figure 5.25: white noise.

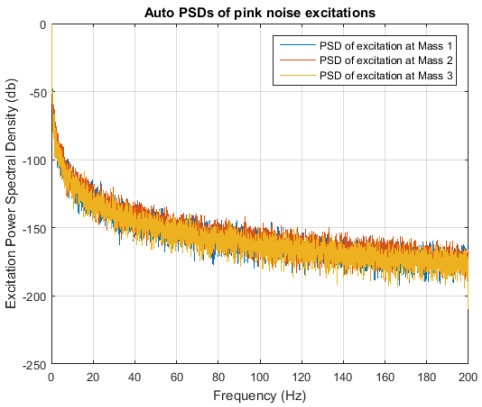

Figure 5.26: pink noise

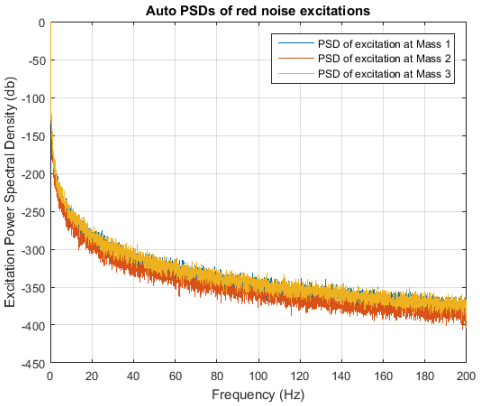

Figure 5.27: red noise

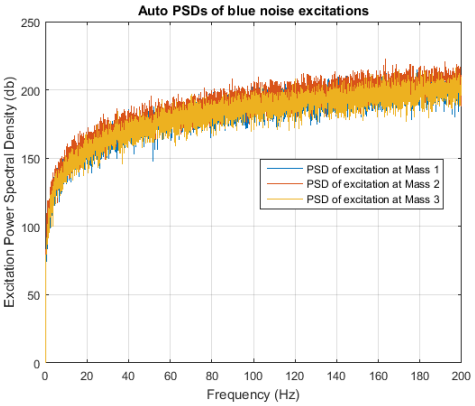

Figure 5.28: blue noise

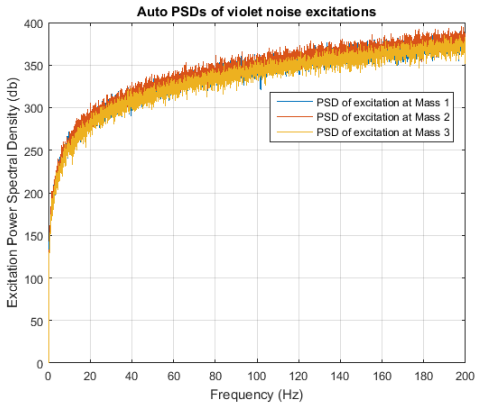

Figure 5.29: violet noise

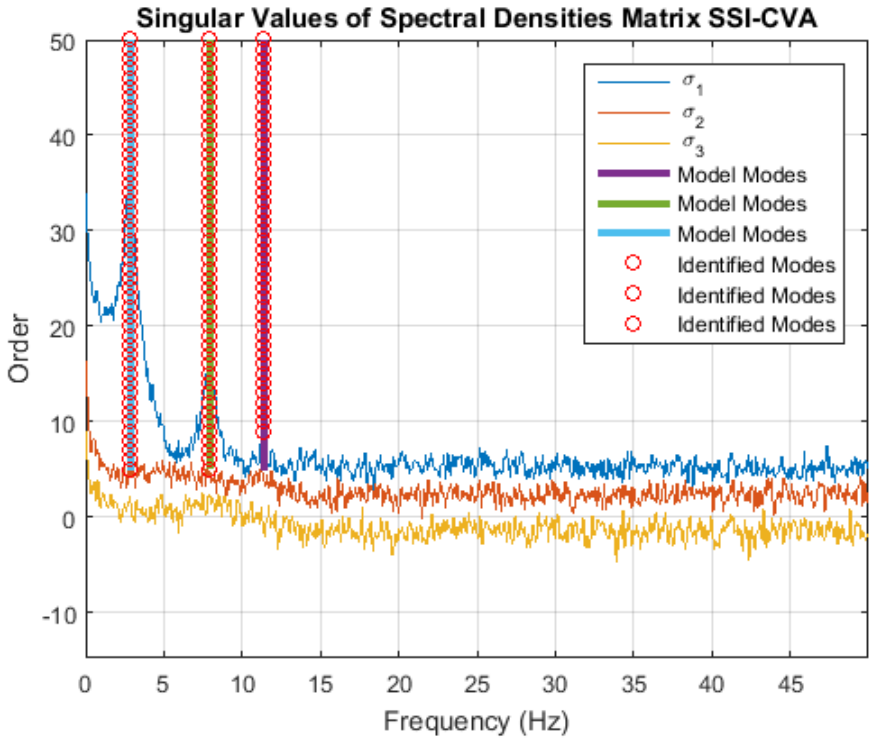

Figure 5.30: Stabilization diagram over Singular Value of Spectral Densities for pink noise excitation.

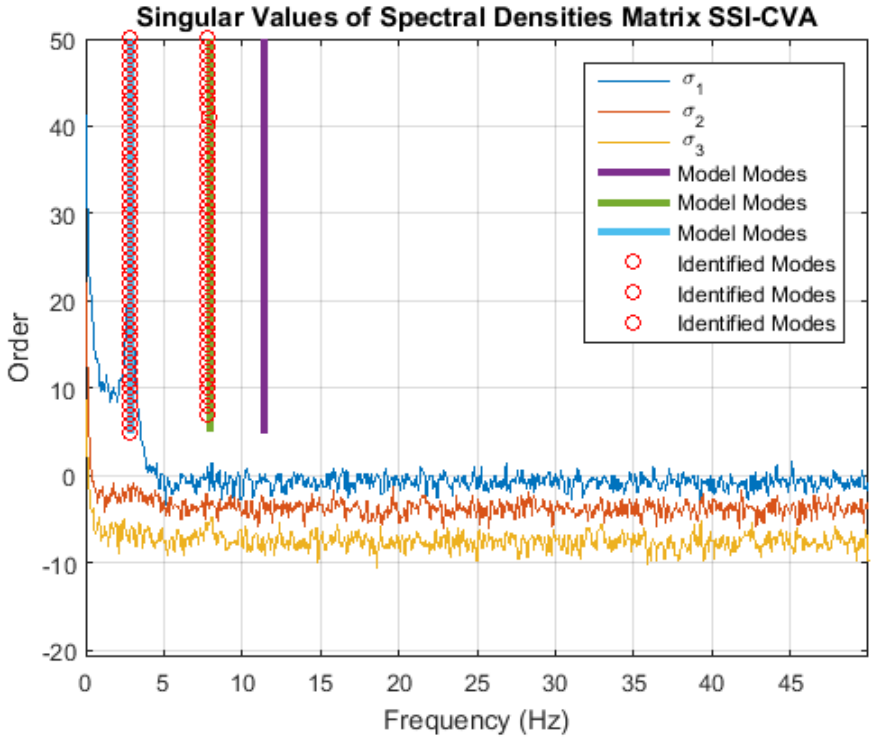

Figure 5.31: Stabilization diagram over Singular Value of Spectral Densities for red noise excitation.

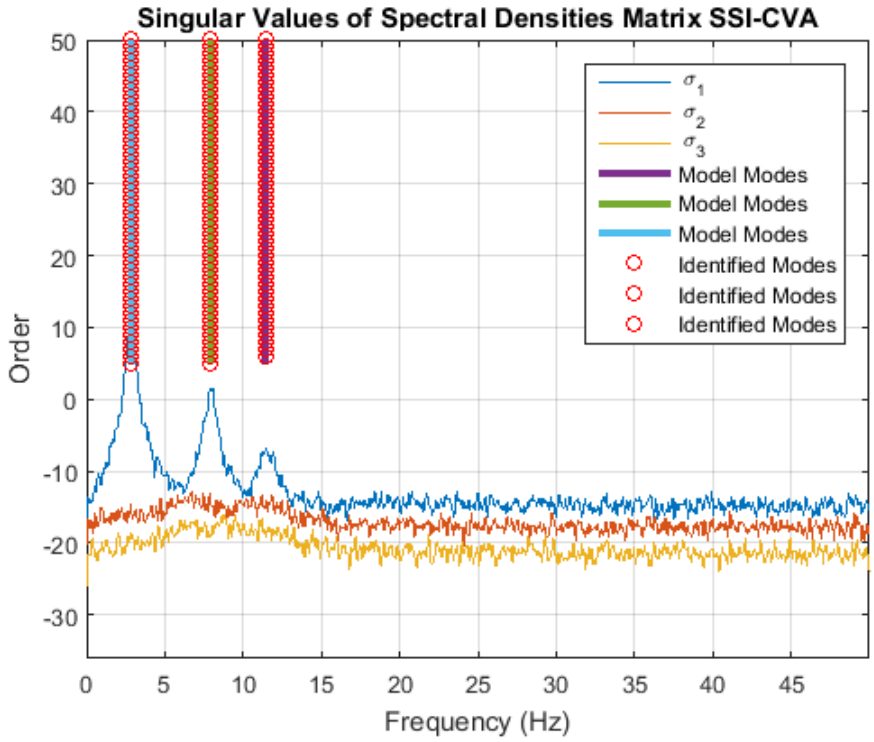

Figure 5.32: Stabilization diagram over Singular Value of Spectral Densities for blue noise excitation.

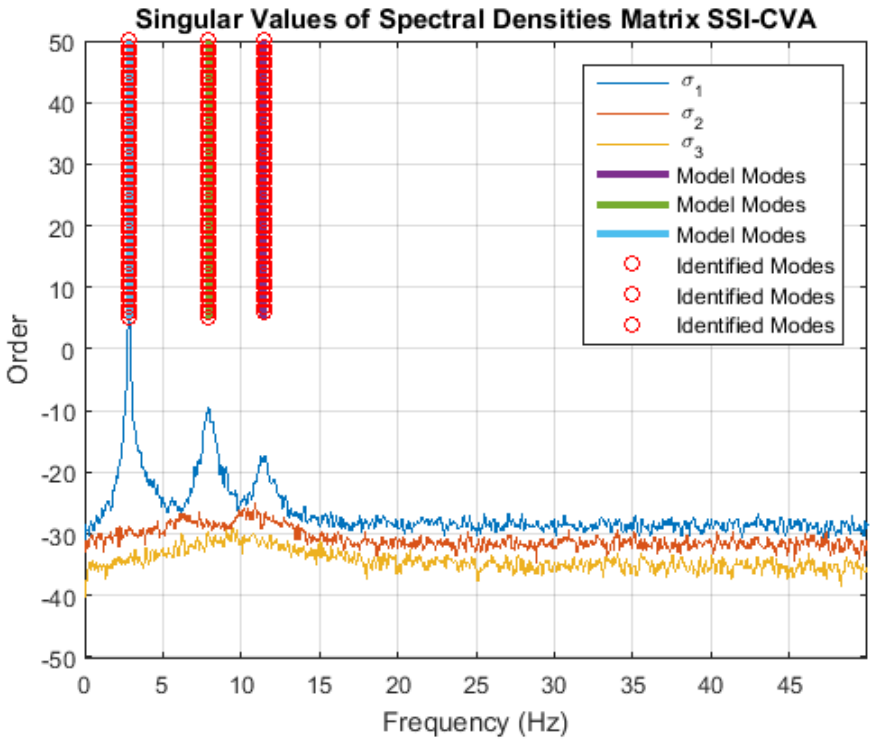

Figure 5.33: Stabilization diagram over Singular Value of Spectral Densities for violet noise excitation.

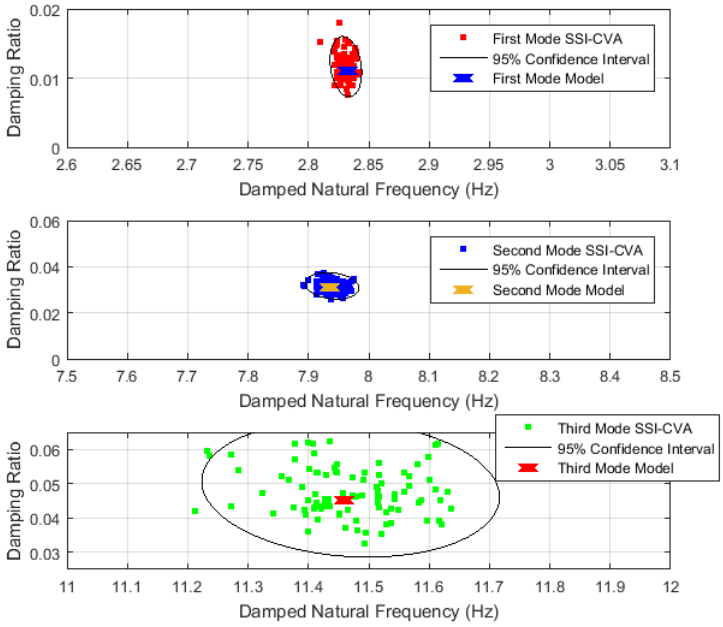

Figure 5.34: Damped Natural Frequency and Damping Ratio Identification through SSI-CVA method in 100 Monte Carlo runnings for pink noise excitation.

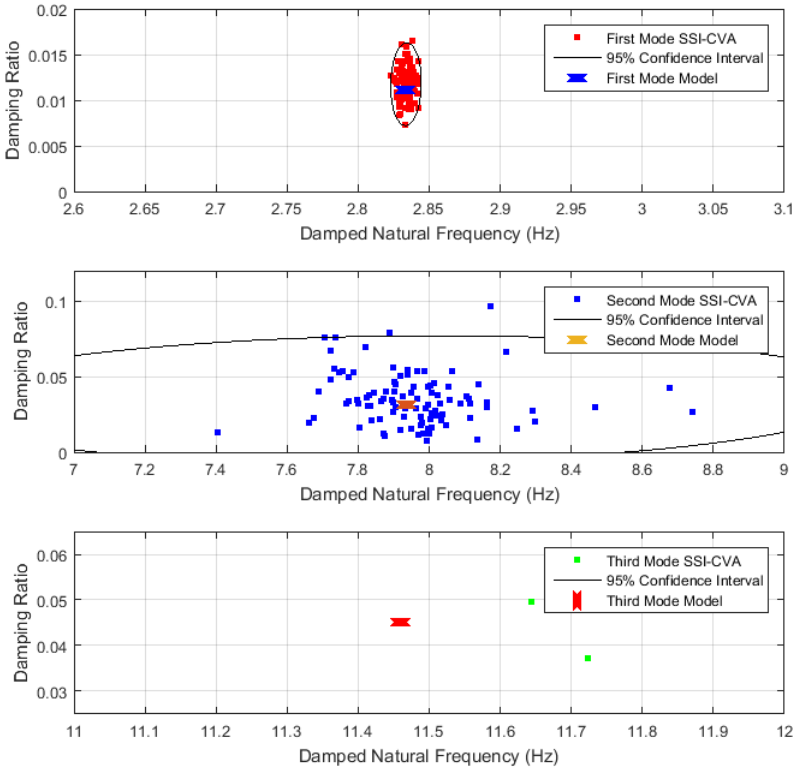

Figure 5.35: Damped Natural Frequency and Damping Ratio Identification through SSI-CVA method in 100 Monte Carlo runnings for red noise excitation.

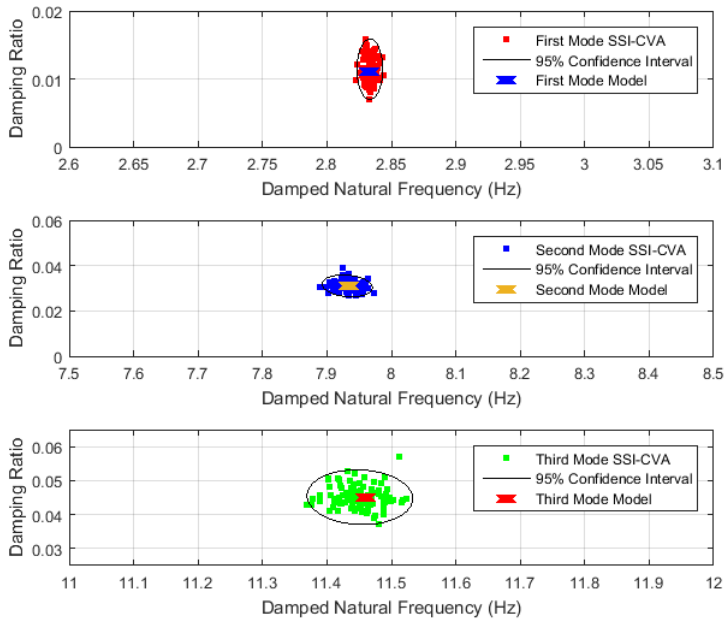

Figure 5.36: Damped Natural Frequency and Damping Ratio Identification through SSI-CVA method in 100 Monte Carlo runnings for blue noise excitation.

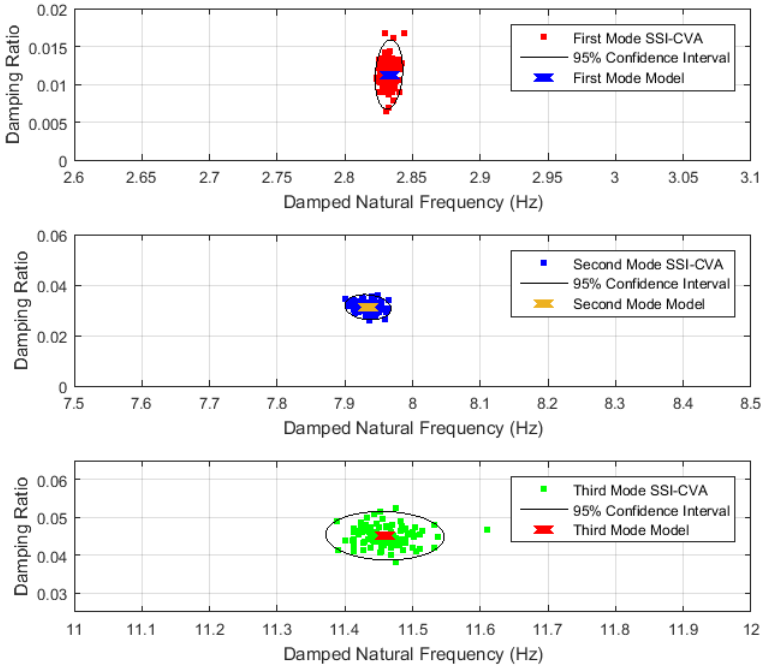

Figure 5.37: Damped Natural Frequency and Damping Ratio Identification through SSI-CVA method in 100 Monte Carlo runnings for violet noise excitation.

5.1.3 Identification from the Finite Element model

The rotor model was also excited with white noise, applied to each of its impellers. The inputs of OMA was the response in X and Y direction in the region of proximity probes (near the bearings nodes, see Chapter 4). Uncorrelated noise was also added to the response.

The process was repeated several times, each time with a new white noise excitation being applied and a new uncorrelated white noise being added to the obtained system response, in order to allow a Monte Carlo analysis of the damping ratio and natural frequencies identification using different OMA methods.

The first model analyzed was the rotor-bearing system, without cross-coupling. The sampling frequency adopted in this discrete model was 4000 Hz and each Monte Carlo run was performed with 1 minute of response data.

Computational modes were eliminated adopting the criteria of stable frequencies, damping ratio and modeshapes among different model orders. Modes with a deviation of more than 3 percent at the identified frequencies, a deviation of more than 7 percent at the identified damping ratio or a MAC lower than 0.95 between the orders, were considered unstable. The higher margins of acceptance, comparing with the mass-spring-damper model were defined due to the higher complexity of the system as stated at the Chapter 4, section Finite Element Rotor Model. Figures 5.38 and 5.39 shows a stabilization diagram over the singular values of PSD matrices plot for a SNR of 10, obtained with SSI-CVA method before and after applying the stable modes criteria, respectively. It can be observed that all the computational modes were eliminated.

It is worth notice that the stability criteria to eliminate computational modes has nothing to do with the stability analysis of turbomachinery. The first is a deviation criteria related with the modal parameters identified among different OMA model orders, while the second is related with the real part of the structural system eigenvalues.

It is possible to see that the first and second singular values modulates together, presenting peaks near 101, 103, 361 and 372 Hz. Once they are closely spaced modes, and the white noise excitation applied to each impeller excites both the forward and backward modes, first and second singular values have presented the same order of energy.

To verify if the identified mode corresponds to a forward or backward mode, the identified modeshapes can be plotted and compared with the spinning direction. The model was simulated with clockwise spinning direction. Figure 5.40 shows the identified modeshapes corresponding to the stabilization diagram from figure 5.39. At this plot, dot means the beginning of a revolution and the blank means the

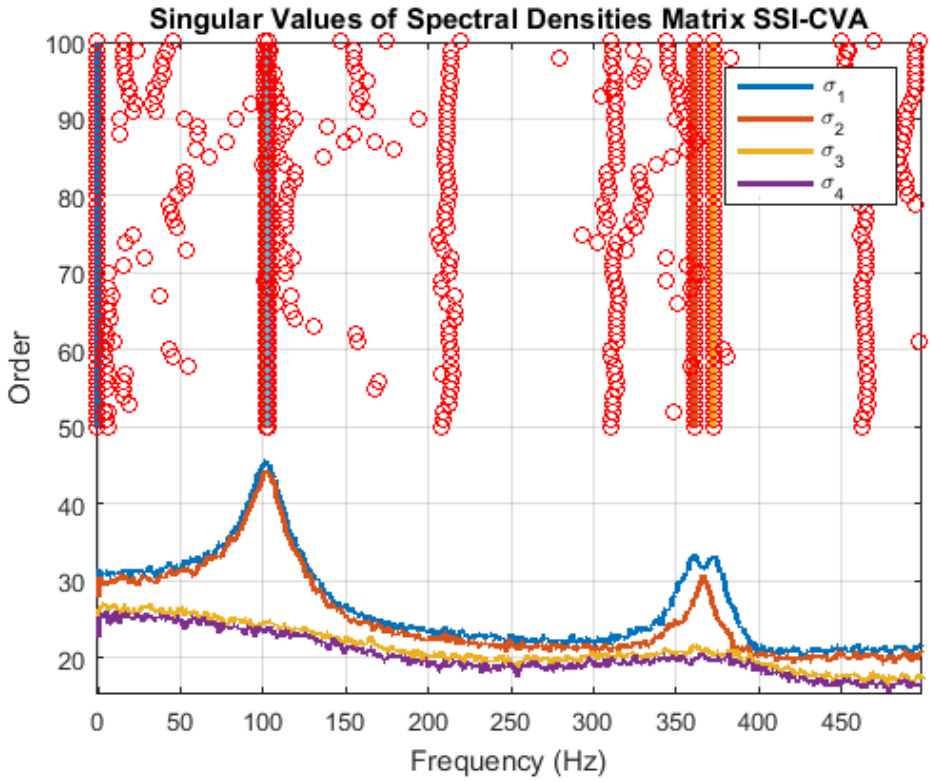

Figure 5.38: Stabilization diagram over Singular Value of Spectral Densities for FEM rotor-bearing system with white noise excitation applied to each impeller, SNR 10 wihtout computational modes elimination.

end, showing the direction of the modeshape precession. Figure 5.41 shows the modeshapes from the model, at the same positions. Good agreement was found between the identified and model modeshapes.

By looking to the MAC between the identified modes (Figure 5.42), it is possible to observe that they are independent between each other, what is an expected outcome for this rotor-bearing system.

Modeshape plots can also be used to verify if an identified mode is a structural or computational mode. Generally, computational modes presents shapes that are unexpected for the frequency range where they are identified, allowing its elimination by simple visual inspection. Figure 5.43 shows examples of computational modeshapes identified by the OMA methods applied to the FEM model.

Figures 5.44 and 5.45 presents box plots with damped natural frequencies and damping ratio respectively, identified from the 100 Monte Carlo runnings for a SNR of 10, using SSI-CVA, SSI-PC, SSI-UPC, MOBAR and SSI-UPC Cov.

Tables 5.12, 5.13, 5.14, 5.15 and 5.16 summarizes the modal parameters extracted, showing the mean values (μ), the standard deviation σ and the error of the identified parameters of 100 Monte Carlo simulations for a SNR of 10.

It can be observed good agreement with the FEM model, even in the presence of

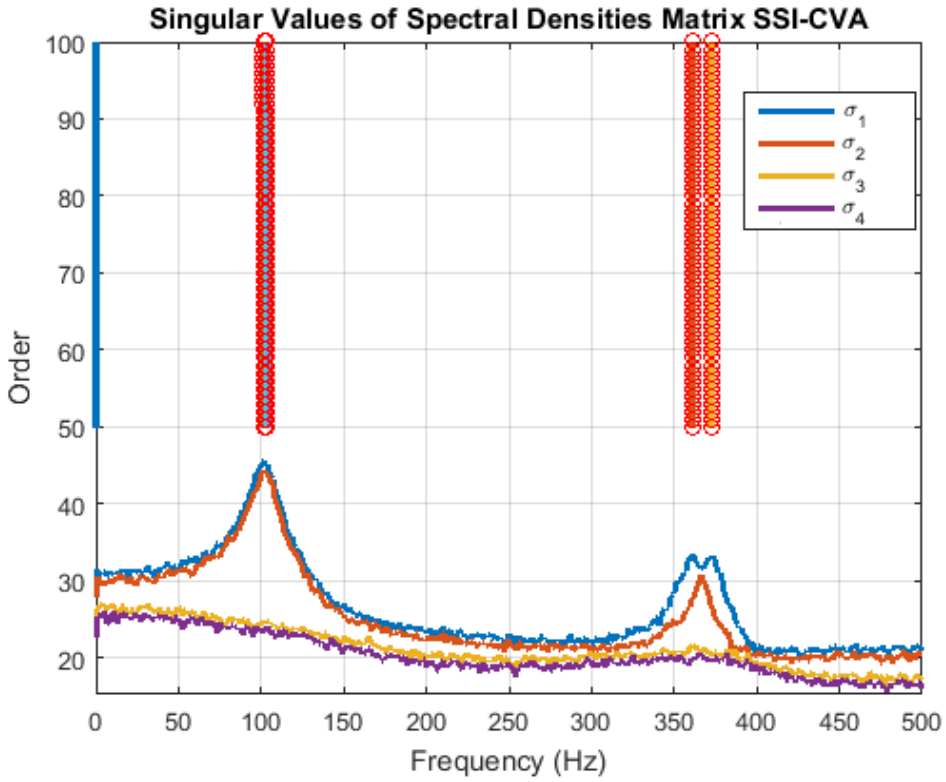

Figure 5.39: Stabilization diagram over Singular Value of Spectral Densities for FEM of rotor-bearing system with white noise excitation applied to each impeller, SNR 10 after computational modes elimination.

closely space modes. Similarly to the mass spring, although the standard deviation is considerable, the mean value obtained through many realizations presents an acceptable level of error.

Figures 5.46, 5.47, 5.48, 5.49 and 5.50 allows a visual inspection of the spread of natural frequencies and damping ratio obtained from the Monte Carlo runnings for SSI-UPC, CVA, PC, SSI-UPC Cov and MOBAR with SNR 10 respectively.

Figures 5.51 and 5.52 presents box plots with damped natural frequencies and damping ratio respectively, identified from the 100 Monte Carlo runnings for a SNR of 2, using SSI-CVA, SSI-PC, SSI-UPC, MOBAR and SSI-UPC Cov.

As presented for the mass-spring-damper model, to allow a better comparison between the identification performed with synthetic data generated with SNR 10 and SNR 2, the box plots already presented for the rotor-bearing model were compiled side by side in figures 5.15, 5.54, 5.55 and 5.56.

The results obtained for this SNR were also satisfactory, although outliers with higher deviation were observed in comparison with the analysis performed with SNR 10.

Tables 5.17, 5.18, 5.19, 5.20 and 5.21 shows the results for a SNR of 2 and figures 5.57, 5.58, 5.59, 5.60 and 5.61 allows a visual inspection of the spread. The outlier

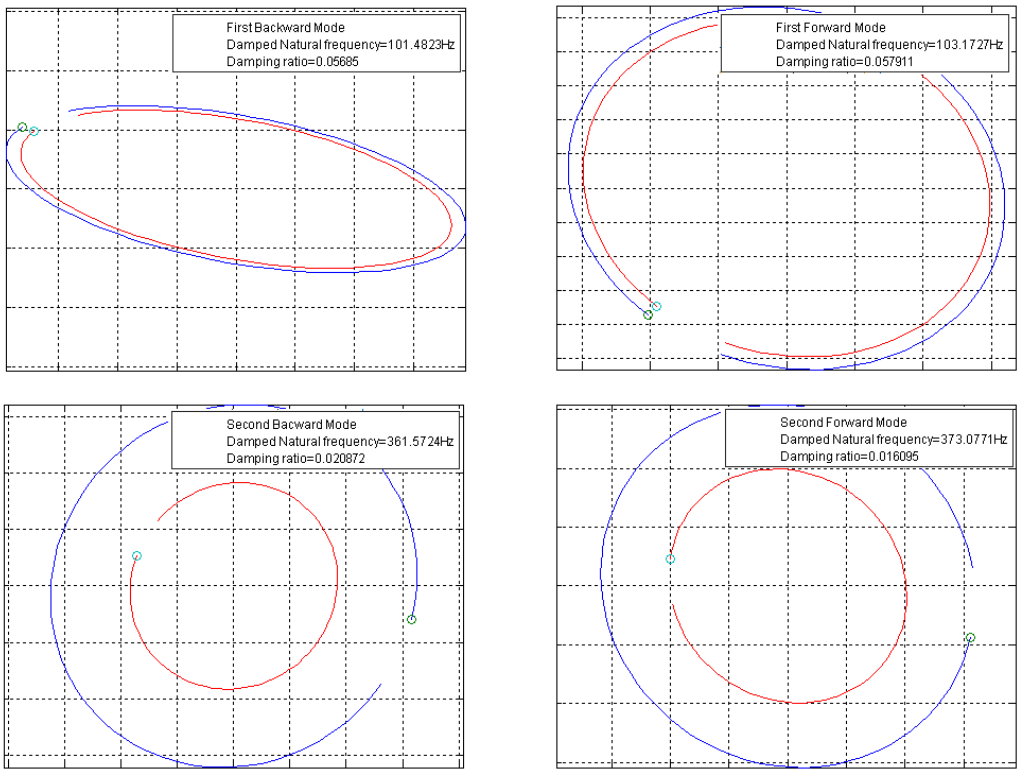

Figure 5.40: Identified modeshapes, DE bearing in blue and NDE bearing in red.

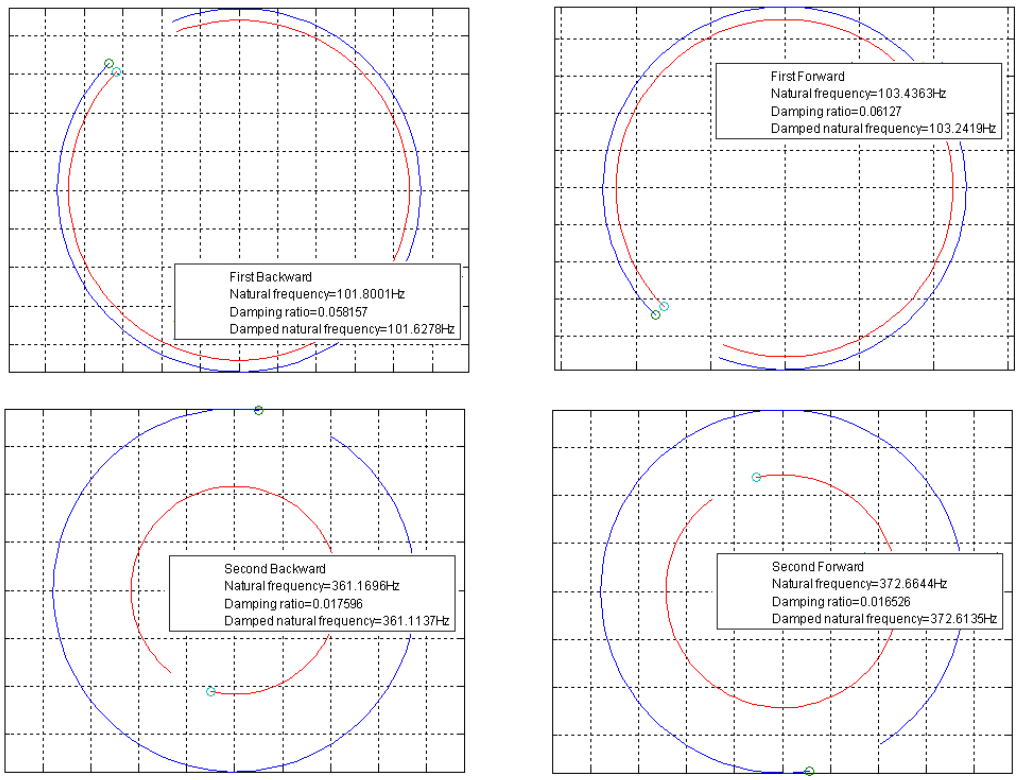

Figure 5.41: Model modeshapes, DE blue and NDE red.

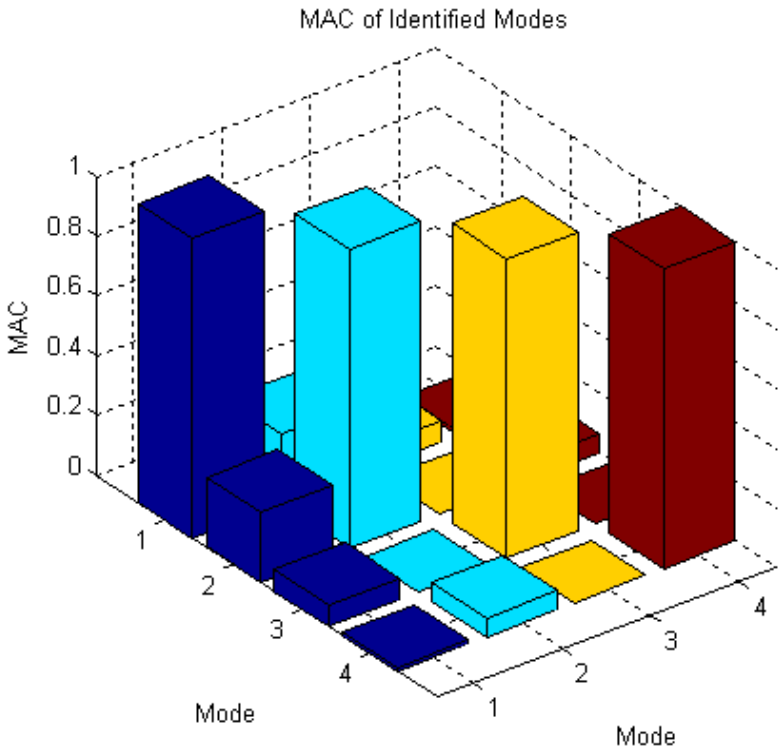

Figure 5.42: MAC between the identified modes 1- First Backward, 2- First Forward, 3- Second Backward and 4- Second Forward.

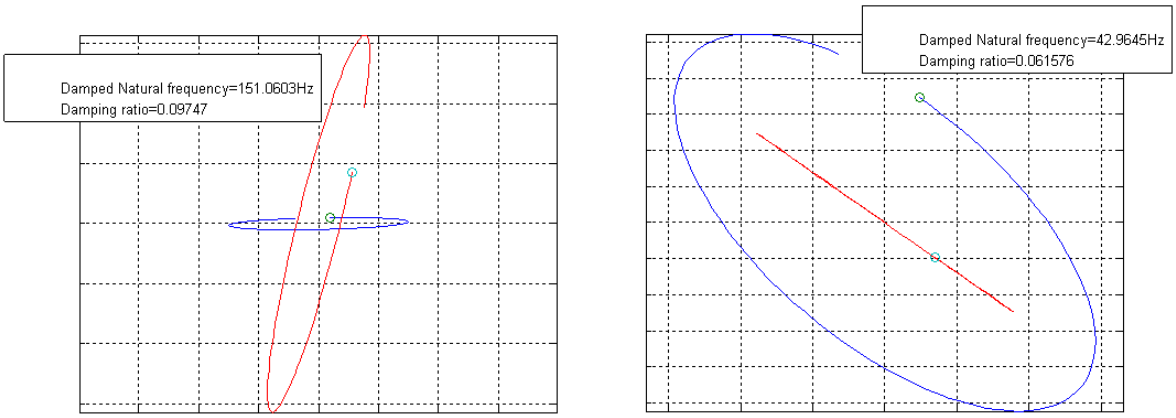

Figure 5.43: Examples of computational modeshapes identified, DE blue and NDE red.

were not eliminated in these figures and tables.

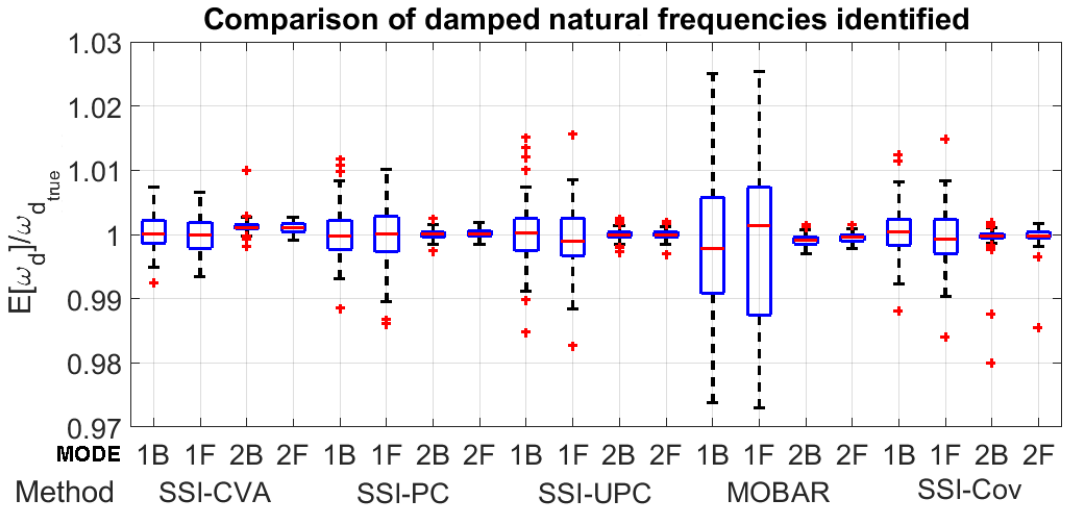

Figure 5.44: Box plot of identified damped natural frequencies for the rotor-bearing system model with SNR 10.

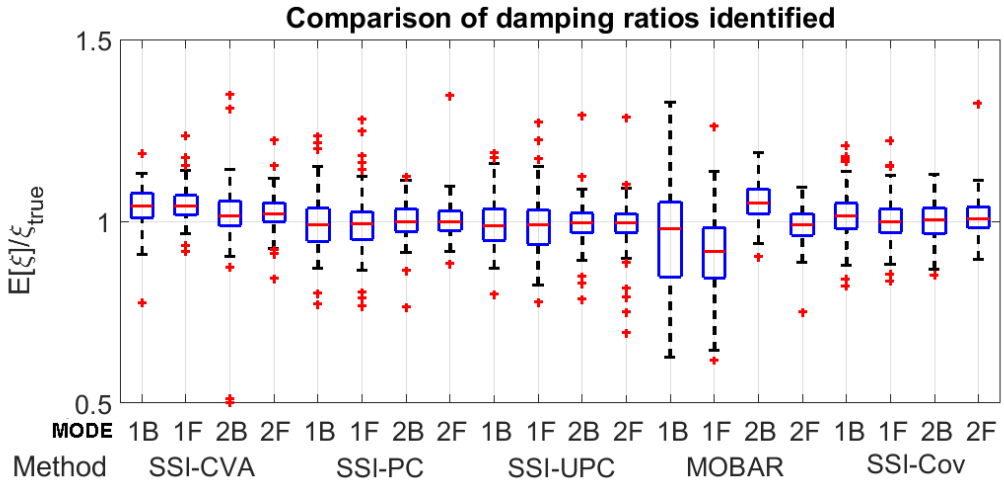

Figure 5.45: Box plot of identified damping ratio for the rotor-bearing system model with SNR 10.

Table 5.12: Rotor-bearing system eigenvalues identified by SSI-UPC method, SNR 10, 1 minutes of data acquired, 100 Monte Carlo runs.

Mode	1^{st} Backward	1^{st} Forward	2^{nd} Backward	2^{nd} Forward
$\mu(w_n)$ (Hz)	101.8043	103.3665	361.1403	372.6698
$\sigma(w_n)$ (%)	0.47	0.51	0.08	0.07
$error(\mu(w_n))$ (%)	0.00	-0.06	0.01	0.00
$\mu(w_d)$ (Hz)	101.6329	103.1759	361.0845	372.6199
$\sigma(w_d)$ (%)	0.48	0.51	0.08	0.07
$error(\mu(w_d))$ (%)	0.00	-0.06	0.01	0.00
$\mu(\xi)$	0.05783	0.060477	0.01755	0.016330654
$\sigma(\xi)$ (%)	7.71	8.72	5.88	7.00
$error(\mu(\xi))$ (%)	-0.57	-1.29	-0.3	-1.03

Table 5.13: Rotor-bearing system eigenvalues identified by SSI-PC method, SNR 10, 1 minute of data acquired, 100 Monte Carlo runs.

Mode	1^{st} Backward	1^{st} Forward	2^{nd} Backward	2^{nd} Forward
$\mu(w_n)$ (Hz)	101.8188	103.4243	361.1673	372.7148
$\sigma(w_n)$ (%)	0.39	0.43	0.08	0.06
$error(\mu(w_n))$ (%)	0.02	-0.01	0.0	0.01
$\mu(w_d)$ (Hz)	101.6469	103.2309	361.1113	372.6633
$\sigma(w_d)$ (%)	0.38	0.44	0.08	0.06
$error(\mu(w_d))$ (%)	0.02	-0.01	0.0	0.01
$\mu(\xi)$	0.05790	0.06093	0.01758	0.01659
$\sigma(\xi)$ (%)	7.79	8.16	5.30	5.37
$error(\mu(\xi))$ (%)	-0.44	-0.55	-0.09	-0.57

Table 5.14: Rotor-bearing system eigenvalues identified by SSI-CVA method, SNR 10, 1 minute of data acquired, 100 Monte Carlo runs.

Mode	1^{st} Backward	1^{st} Forward	2^{nd} Backward	2^{nd} Forward
$\mu(w_n)$ (Hz)	101.868	103.429	361.5909	373.04139
$\sigma(w_n)$ (%)	0.27	0.31	0.12	0.07
$error(\mu(w_n))$ (%)	0.07	0.00	0.12	0.10
$\mu(w_d)$ (Hz)	101.6795	103.2159	361.5326	372.9879
$\sigma(w_d)$ (%)	0.27	0.30	0.12	0.07
$error(\mu(w_d))$ (%)	0.05	-0.02	0.21	0.10
$\mu(\xi)$	0.06074	0.06408	0.01786	0.01691
$\sigma(\xi)$ (%)	8.39	4.67	9.70	5.12
$error(\mu(\xi))$ (%)	4.43	4.59	1.5	2.49

Table 5.15: Rotor-bearing system eigenvalues identified by Cov SSI-UPC method, SNR 10, 1 minute of data acquired, 100 Monte Carlo runs.

Mode	1^{st} Backward	1^{st} Forward	2^{nd} Backward	2^{nd} Forward
$\mu(w_n)$ (Hz)	101.869	103.392	361.087	372.617
$\sigma(w_n)$ (%)	0.37	0.043	0.08	0.08
$error(\mu(w_n))$ (%)	0.07	-0.04	-0.02	-0.01
$\mu(w_d)$ (Hz)	101.691	103.196	360.913	372.511
$\sigma(w_d)$ (%)	0.37	0.42	0.24	0.16
$error(\mu(w_d))$ (%)	0.06	-0.04	-0.05	-0.03
$\mu(\xi)$	0.05902	0.06142	0.01764	0.01667
$\sigma(\xi)$ (%)	6.66	6.33	5.04	5.3
$error(\mu(\xi))$ (%)	1.48	0.25	0.24	1.05

Table 5.16: Rotor-bearing system eigenvalues identified by MOBAR method, SNR 10, 1 minute of data acquired, 100 Monte Carlo runs.

Mode	1^{st} Backward	1^{st} Forward	2^{nd} Backward	2^{nd} Forward
$\mu(w_n)$ (Hz)	101.705	103.267	360.825	372.451
$\sigma(w_n)$ (%)	1.1	1.2	0.08	0.07
$error(\mu(w_n))$ (%)	-0.09	-0.16	-0.1	-0.06
$\mu(w_d)$ (Hz)	101.544	103.107	360.76	372.4
$\sigma(w_d)$ (%)	1.09	1.21	0.08	0.07
$error(\mu(w_d))$ (%)	-0.08	-0.13	-0.1	-0.06
$\mu(\xi)$	0.0554	0.05534	0.0184	0.0163
$\sigma(\xi)$ (%)	16.53	13.02	8.49	5.49
$error(\mu(\xi))$ (%)	-4.67	-9.67	4.66	-1.04

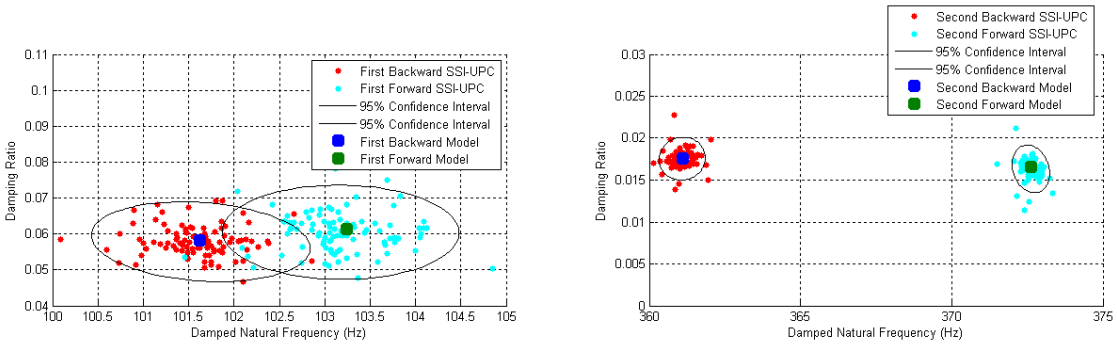

Figure 5.46: Rotor-bearing system Damped Natural Frequency and Damping Ratio identification through SSI-UPC method in 100 Monte Carlo runnings, SNR 10, 1 minute of data acquired.

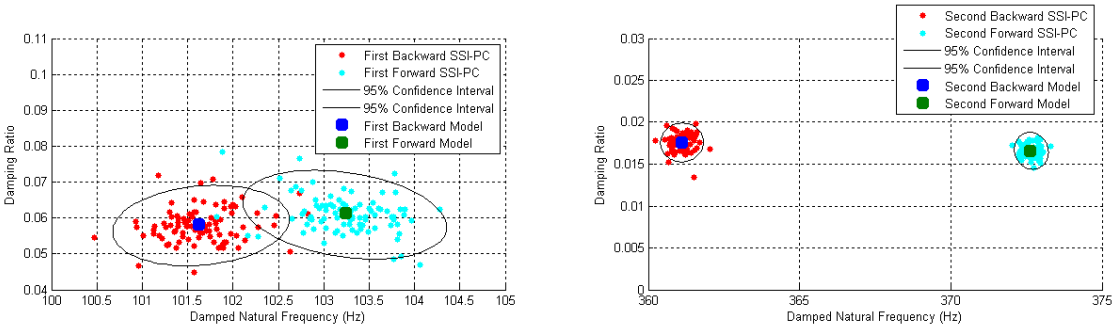

Figure 5.47: Rotor-bearing system Damped Natural Frequency and Damping Ratio identification through SSI-PC method in 100 Monte Carlo runnings, SNR 10, 1 minute of data acquired.

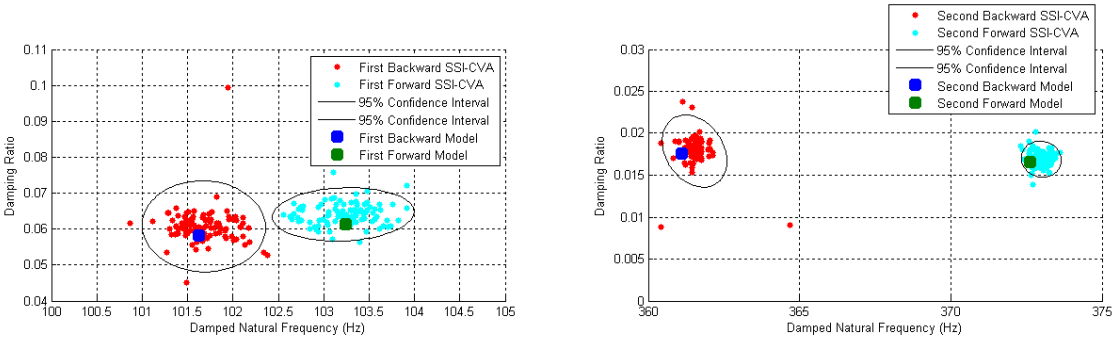

Figure 5.48: Rotor-bearing system Damped Natural Frequency and Damping Ratio identification through SSI-CVA method in 100 Monte Carlo runnings, SNR 10, 1 minute of data acquired.

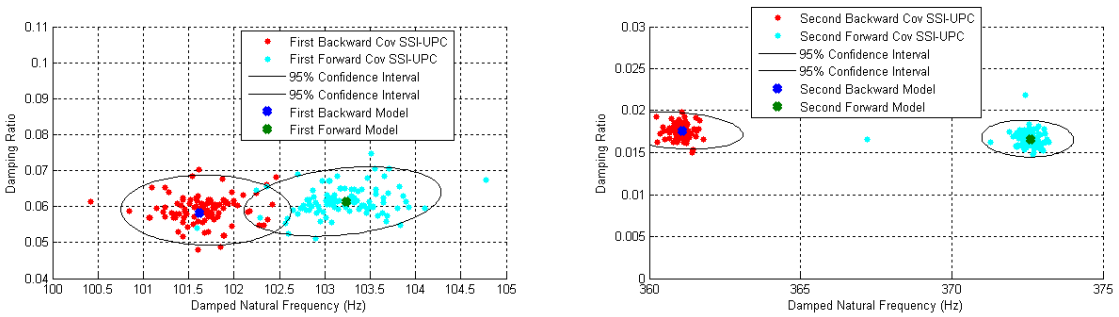

Figure 5.49: Rotor-bearing system Damped Natural Frequency and Damping Ratio identification through Cov SSI-UPC method in 100 Monte Carlo runnings, SNR 10, 1 minute of data acquired.

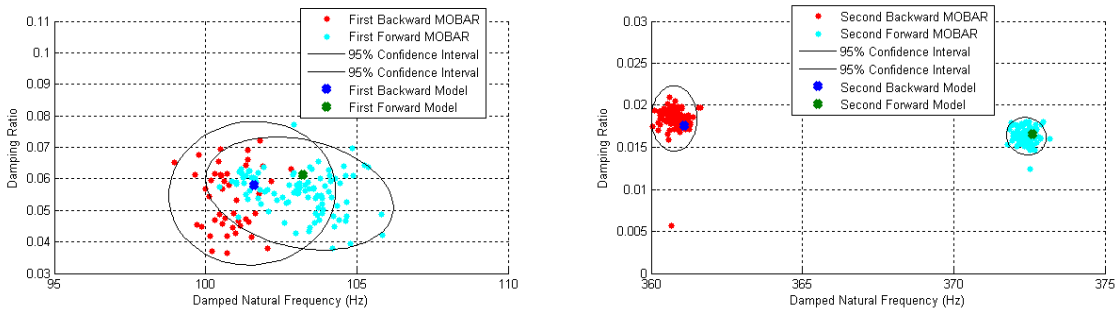

Figure 5.50: Rotor-bearing system Damped Natural Frequency and Damping Ratio identification through MOBAR method in 100 Monte Carlo runnings, SNR 10, 1 minute of data acquired.

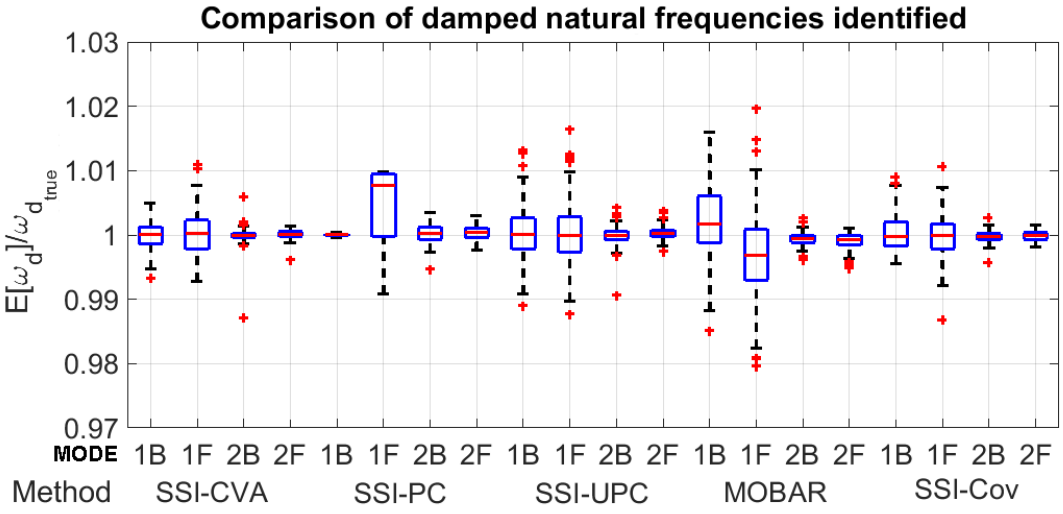

Figure 5.51: Box plot of identified damped natural frequencies for the rotor-bearing system model with SNR 2.

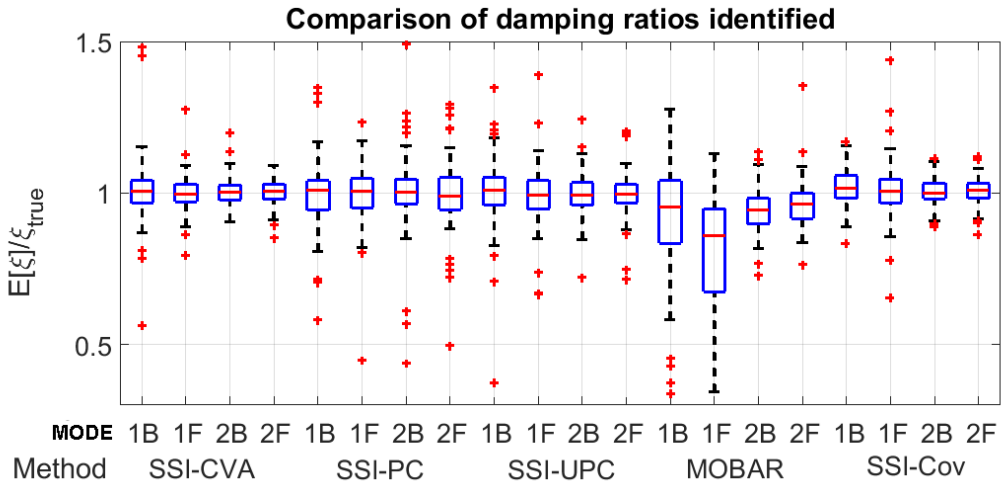

Figure 5.52: Box plot of identified damping ratio for the rotor-bearing system model with SNR 2.

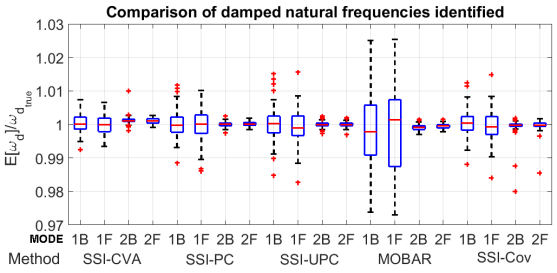

Figure 5.53: Box plot ω_d, SNR 10.

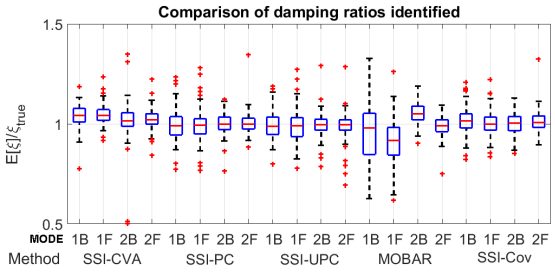

Figure 5.54: Box plot ξ, SNR 10.

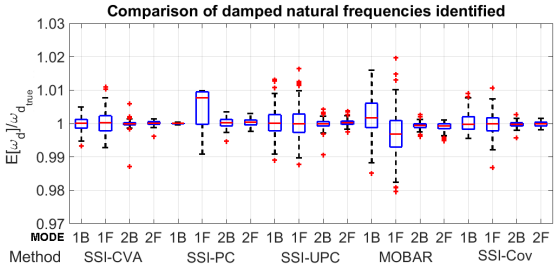

Figure 5.55: Box plot ω_d, SNR 2.

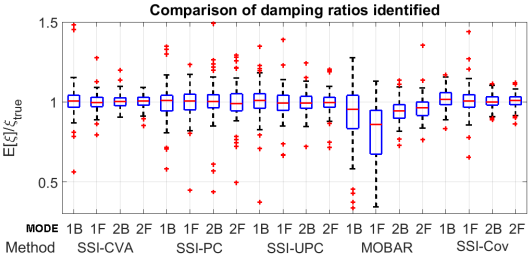

Figure 5.56: Box plot ξ, SNR 2.

Table 5.17: Rotor-bearing system eigenvalues identified by SSI-UPC method, SNR 2, 1 minute of data acquired, 100 Monte Carlo runs.

Mode	1^{st} Backward	1^{st} Forward	2^{nd} Backward	2^{nd} Forward
$\mu(w_n)$ (Hz)	101.8341	103.4712	361.163	372.753
$\sigma(w_n)$ (%)	0.43	0.48	0.12	0.10
$error(\mu(w_n))$ (%)	0.03	0.04	0.00	0.02
$\mu(w_d)$ (Hz)	101.658	103.278	361.081	372.70
$\sigma(w_d)$ (%)	0.43	0.48	0.15	0.10
$error(\mu(w_d))$ (%)	0.03	0.04	-0.01	0.02
$\mu(\xi)$	0.0585	0.06078	0.01784	0.01657
$\sigma(\xi)$ (%)	10.94	9.7	18.16	10.79
$error(\mu(\xi))$ (%)	0.58	-0.8	1.38	0.46

Table 5.18: Rotor-bearing system eigenvalues identified by SSI-PC method, SNR 2, 1 minute of data acquired, 100 Monte Carlo runs.

Mode	1^{st} Backward	1^{st} Forward	2^{nd} Backward	2^{nd} Forward
$\mu(w_n)$ (Hz)	101.8332	103.4023	361.1452	372.7414
$\sigma(w_n)$ (%)	0.43	0.57	0.13	0.11
$error(\mu(w_n))$ (%)	0.03	-0.03	-0.01	0.02
$\mu(w_d)$ (Hz)	101.6581	103.2079	361.0884	372.6904
$\sigma(w_d)$ (%)	0.43	0.58	0.13	0.11
$error(\mu(w_d))$ (%)	0.03	-0.03	-0.01	0.02
$\mu(\xi)$	0.0583	0.0610	0.0176	0.0164
$\sigma(\xi)$ (%)	10.97	9.38	12.05	10.86
$error(\mu(\xi))$ (%)	0.17	-0.39	0.04	-0.37

Table 5.19: Rotor-bearing system eigenvalues identified by SSI-CVA method, SNR 2, 1 minute of data acquired, 100 Monte Carlo runs.

Mode	1^{st} Backward	1^{st} Forward	2^{nd} Backward	2^{nd} Forward
$\mu(w_n)$ (Hz)	101.797	103.4587	361.1753	372.6986
$\sigma(w_n)$ (%)	0.24	0.37	0.09	0.07
$error(\mu(w_n))$ (%)	0.00	0.03	0.00	0.01
$\mu(w_d)$ (Hz)	101.6212	103.2643	361.0687	372.647
$\sigma(w_d)$ (%)	0.24	0.36	0.16	0.07
$error(\mu(w_d))$ (%)	-0.01	0.02	-0.01	0.01
$\mu(\xi)$	0.05852	0.06122	0.0177	0.01653
$\sigma(\xi)$ (%)	9.77	5.87	4.13	4.31
$error(\mu(\xi))$ (%)	0.63	-0.08	0.54	0.17

Table 5.20: Rotor-bearing system eigenvalues identified by Cov SSI-UPC method, SNR 2, 1 minute of data acquired, 100 Monte Carlo runs.

Mode	1^{st} Backward	1^{st} Forward	2^{nd} Backward	2^{nd} Forward
$\mu(w_n)$ (Hz)	101.8376	103.4101	361.0816	372.6130
$\sigma(w_n)$ (%)	0.29	0.34	0.08	0.07
$error(\mu(w_n))$ (%)	0.04	-0.02	-0.02	-0.01
$\mu(w_d)$ (Hz)	101.6506	103.2109	361.0104	372.5617
$\sigma(w_d)$ (%)	0.29	0.34	0.09	0.07
$error(\mu(w_d))$ (%)	0.02	-0.03	-0.03	-0.01
$\mu(\xi)$	0.0601	0.0618	0.0177	0.0166
$\sigma(\xi)$ (%)	12.50	8.82	4.47	4.31
$error(\mu(\xi))$ (%)	3.35	0.87	0.50	0.48

Table 5.21: Rotor-bearing system eigenvalues identified by MOBAR method, SNR 2, 1 minute of data acquired, 100 Monte Carlo runs.

Mode	1^{st} Backward	1^{st} Forward	2^{nd} Backward	2^{nd} Forward
$\mu(w_n)$ (Hz)	101.9783	103.0671	360.9262	372.2689
$\sigma(w_n)$ (%)	0.56	0.70	0.10	0.12
$error(\mu(w_n))$ (%)	0.18	-0.35	-0.07	-0.10
$\mu(w_d)$ (Hz)	101.82	102.9398	360.8762	372.22173
$\sigma(w_d)$ (%)	0.59	0.72	0.10	0.12
$error(\mu(w_d))$ (%)	0.19	-0.29	-0.06	-0.10
$\mu(\xi)$	0.0536	0.0477	0.0166	0.015880472
$\sigma(\xi)$ (%)	28.63	29.41	7.57	7.30
$error(\mu(\xi))$ (%)	-7.88	-22.13	-5.67	-3.75

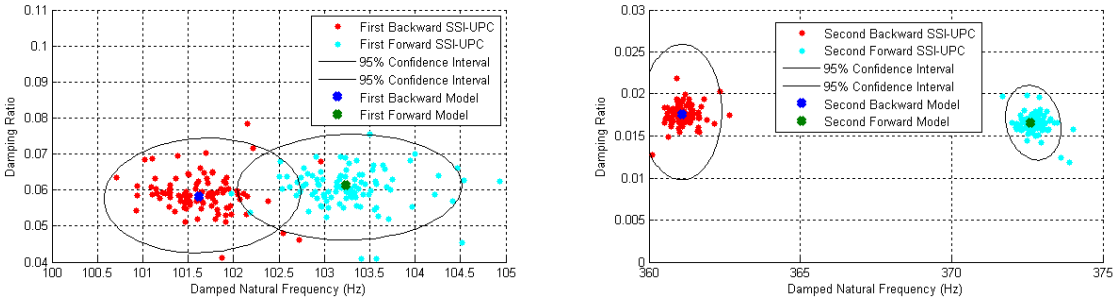

Figure 5.57: Rotor-bearing system Damped Natural Frequency and Damping Ratio identification through SSI-UPC method in 100 Monte Carlo runnings, SNR 2, 1 minute of data acquired for run.

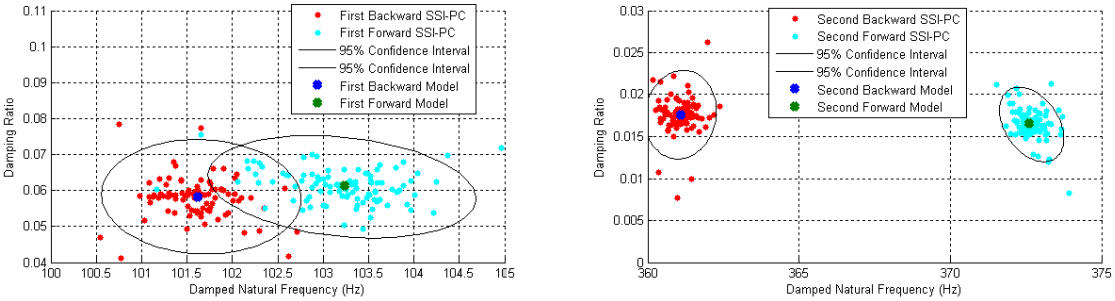

Figure 5.58: Rotor-bearing system Damped Natural Frequency and Damping Ratio identification through SSI-PC method in 100 Monte Carlo runnings, SNR 2, 1 minute of data acquired for run.

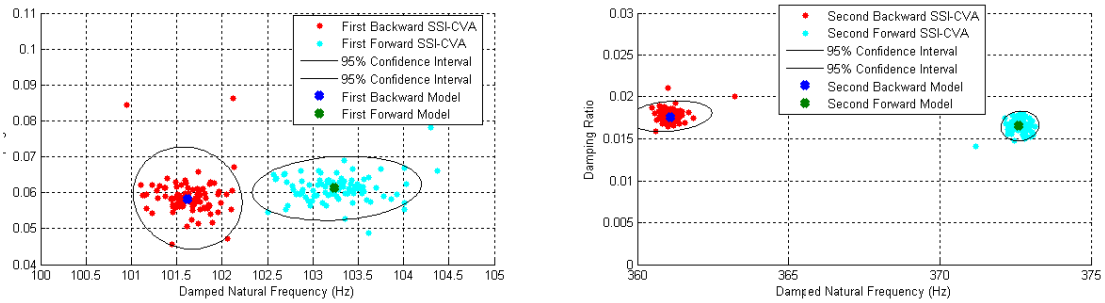

Figure 5.59: Rotor-bearing system Damped Natural Frequency and Damping Ratio identification through SSI-CVA method in 100 Monte Carlo runnings, SNR 2, 1 minute of data acquired for run.

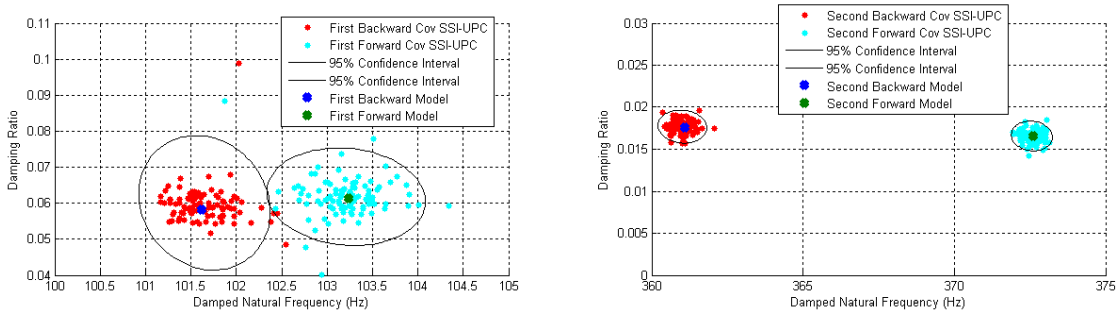

Figure 5.60: Rotor-bearing system Damped Natural Frequency and Damping Ratio identification through Cov SSI-UPC method in 100 Monte Carlo runnings, SNR 2, 1 minute of data acquired for run.

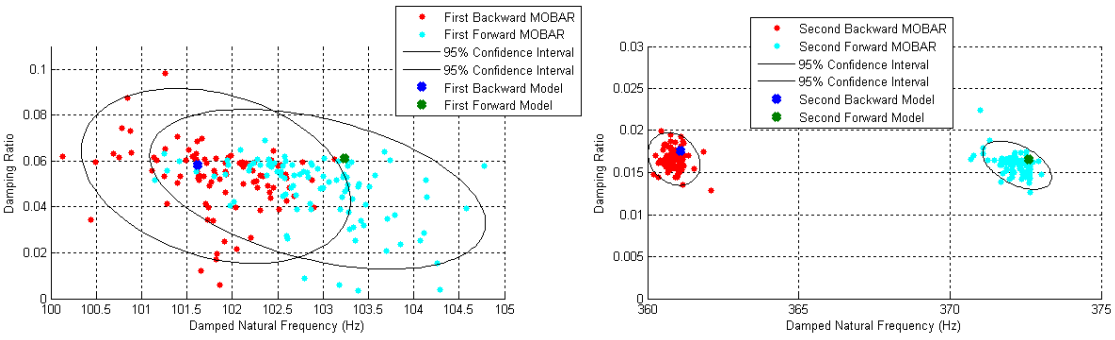

Figure 5.61: Rotor-bearing system Damped Natural Frequency and Damping Ratio identification through MOBAR method in 100 Monte Carlo runnings, 1 minute of data acquired for run.

The second model analyzed was the rotor-bearing system, with cross-coupling applied to the midspan until stability threshold was achieved (damping ratio of first forward mode neat to zero). The sampling frequency adopted in this discrete model was also 4000 Hz and each Monte Carlo run was performed with 1 minute of response data.

Computational modes were eliminated adopting the same criteria adopted for the first FEM model. The closely spaced backward and forward modes at this model have a separation of just 0.27 Hz, what makes the distinction between them a good test of the identification algorithms applied.

Figure 5.62 shows a stabilization diagram over the singular values of PSD matrices plot for a SNR of 2, obtained with SSI-CVA method after applying the computational modes elimination filters. It can be observed that a computational mode appeared at higher orders at the frequency of 277 Hz and was not eliminated by the criteria adopted. Figure 5.63 shows the modeshape of this mode, and once this is unexpected for this frequency range, it could be eliminated by looking at modeshape.

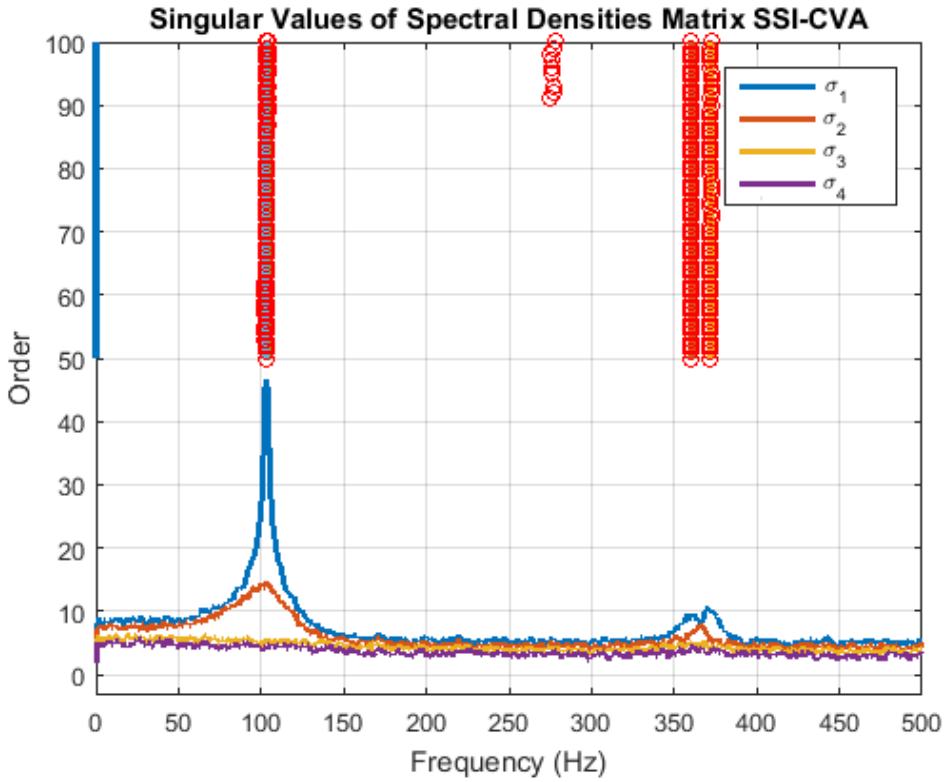

Figure 5.62: Stabilization diagram over Singular Value of Spectral Densities for FEM of rotor-bearing system with cross-coupling applied at midspan until threshold of instability, SNR 2, computational modes eliminated.

The low damping of first forward mode is evidenced by looking to the sharp peak at the first singular value, near 100 Hz. Once sharp peaks are also characteristics of harmonics, it is important to make distinction between an excitation harmonic

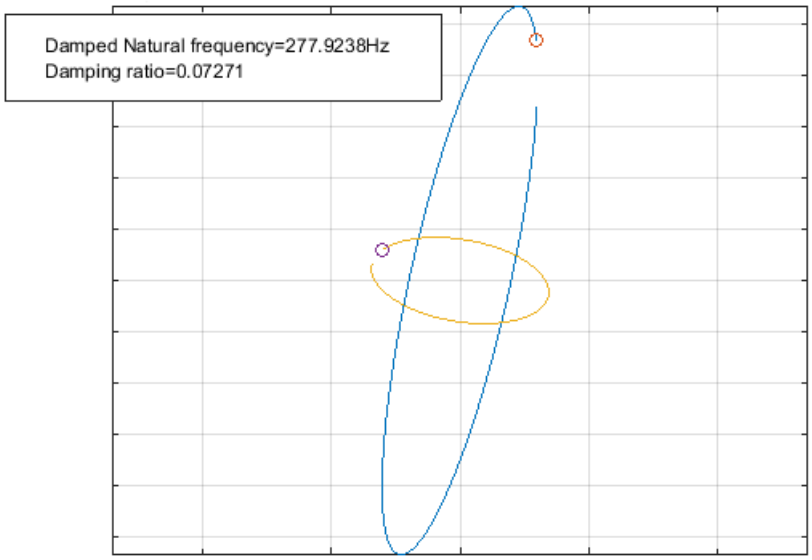

Figure 5.63: Remaining computational modeshape at 277 Hz.

and a modeshape.Two basic features to help in harmonic recognition were adopted at present work (see GUGLIELMO *et al.* [7]).

The first one is related with the second singular value. Although the peak at first singular value is very sharp, the first backward mode usually present increased damping with increasing in cross-coupling, thus the second singular value present a smooth modulation, allowing recognition of a modal response.

The second one makes use of Kurtosis (γ), defined by equation 5.1. By band-pass filtering the signal with a narrow band range, near the interest frequency and calculating the Kurtosis of signal, an harmonic can be recognized. Kurtosis of Gaussian distributed measurements present a value of 3 while sinusoidal measurements presents Kurtosis of 1.5. Thus, a harmonic will present Kurtosis of 1.5 while a mode will present a higher value of Kurtosis. Figure 5.64 shows the average Kurtosis of measurement signals (mean value of the measured channels)as a function of the frequency, evidencing that the sharp peak near 100 Hz is related to a modal response.

$$\gamma = \frac{E[(y-\mu)^4]}{\sigma^4} \tag{5.1}$$

Tables 5.22, 5.23, 5.24, 5.25 and 5.26 shows the results for the modal parameters identification from the rotor-bearing system at threshold of stability with a SNR of 2 using SSI-UPC, SSI-PC, SSI-CVA, SSI-UPC Cov and MOBAR respectively and figures 5.65, 5.66, 5.67, 5.68 and 5.69 allows a visual inspection of the spread. Additionally, figures 5.70 and 5.71 presents the box plots from the damped natural

frequencies and damping ratio identification.

Covariance Driven methods have presented bias at first forward mode damping identification, when comparing with the Data Driven methods, but although the percent errors are high, both Covariance Driven methods applied have shown a damping ratio close to instability, thus being an acceptable error from an engineering perspective.

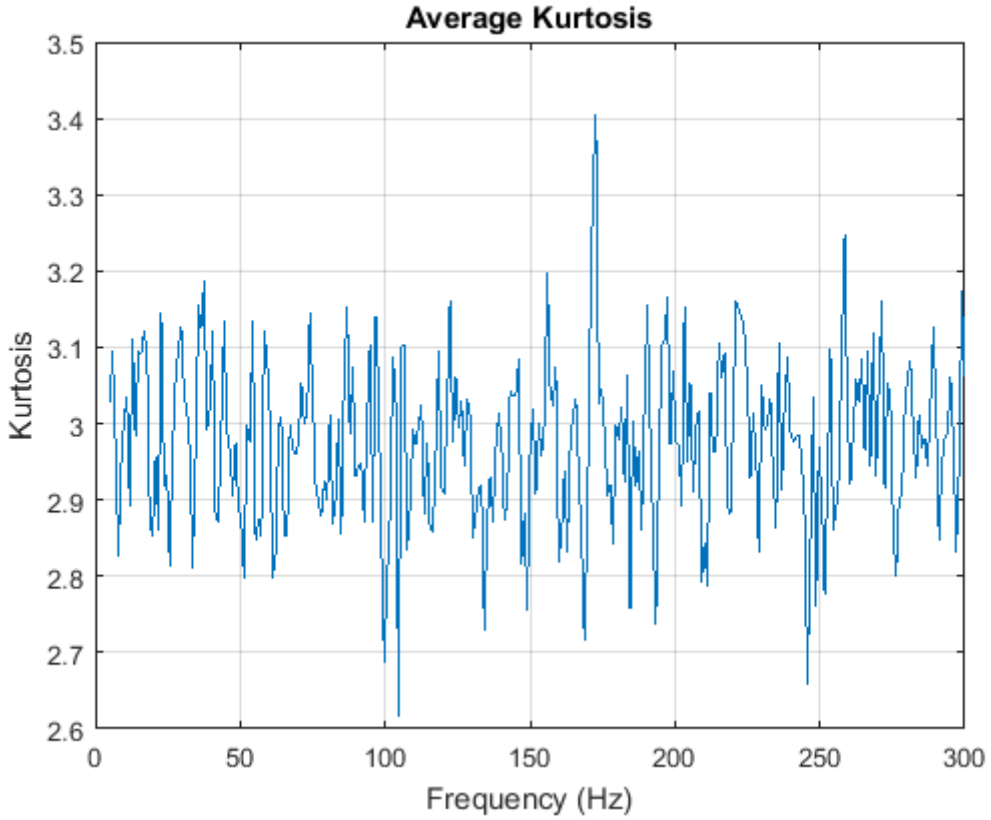

Figure 5.64: Average Kurtosis of measurement signals.

Table 5.22: Eigenvalues identified by SSI-UPC method, SNR 2, 1 minute of data acquired, 100 Monte Carlo runs for the rotor-bearing system with cross-coupling added to midspan until threshold of stability.

Mode	1^{st} Backward	1^{st} Forward	2^{nd} Backward	2^{nd} Forward
$\mu(w_n)$ (Hz)	103.3656	103.1468	361.1737	372.7231
$\sigma(w_n)$ (%)	0.63	0.02	0.16	0.13
$error(\mu(w_n))$ (%)	0.47	0.00	0.01	0.01
$\mu(w_d)$ (Hz)	102.5752	103.14667	361.1069	372.6781
$\sigma(w_d)$ (%)	0.56	0.02	0.16	0.13
$error(\mu(w_d))$ (%)	0.39	0.00	0.00	0.01
$\mu(\xi)$	0.12276	0.0015	0.01914	0.01548
$\sigma(\xi)$ (%)	10.10	15.11	9.36	8.55
$error(\mu(\xi))$ (%)	4.93	0.13	1.25	1.19

Table 5.23: Eigenvalues identified by SSI-PC method, SNR 2, 1 minute of data acquired, 100 Monte Carlo runs for the rotor-bearing system with cross-coupling added to midspan until threshold of stability.

Mode	1^{st} Backward	1^{st} Forward	2^{nd} Backward	2^{nd} Forward
$\mu(w_n)$ (Hz)	103.4342	103.1470	361.2287	372.7745
$\sigma(w_n)$ (%)	0.69	0.02	0.15	0.14
$error(\mu(w_n))$ (%)	0.53	0.00	0.02	0.03
$\mu(w_d)$ (Hz)	102.6257	103.1469	361.1623	372.7035
$\sigma(w_d)$ (%)	0.62	0.02	0.15	0.12
$error(\mu(w_d))$ (%)	0.44	0.00	0.02	0.02
$\mu(\xi)$	0.1239	0.00150 1	0.01906	0.01629
$\sigma(\xi)$ (%)	11.58	14.98	10.80	65.94
$error(\mu(\xi))$ (%)	5.91	0.15	0.86	6.46

Table 5.24: Eigenvalues identified by SSI-CVA method, SNR 2, 1 minute of data acquired, 100 Monte Carlo runs for the rotor-bearing system with cross-coupling added to midspan until threshold of stability.

Mode	1^{st} Backward	1^{st} Forward	2^{nd} Backward	2^{nd} Forward
$\mu(w_n)$ (Hz)	102.7359	103.1463	361.2930	372.9134
$\sigma(w_n)$ (%)	0.13	0.02	0.18	0.13
$error(\mu(w_n))$ (%)	-0.14	0.00	0.04	0.07
$\mu(w_d)$ (Hz)	102.0274	103.1462	361.2239	372.8686
$\sigma(w_d)$ (%)	0.13	0.02	0.18	0.13
$error(\mu(w_d))$ (%)	-0.15	0.00	0.04	0.07
$\mu(\xi)$	0.1171	0.00151	0.01944	0.01544
$\sigma(\xi)$ (%)	4.46	14.85	10.50	8.68
$error(\mu(\xi))$ (%)	0.10	0.67	2.88	0.92

Table 5.25: Eigenvalues identified by Cov SSI-UPC method, SNR 2, 1 minute of data acquired, 100 Monte Carlo runs for the rotor-bearing system with cross-coupling added to midspan until threshold of stability.

Mode	1^{st} Backward	1^{st} Forward	2^{nd} Backward	2^{nd} Forward
$\mu(w_n)$ (Hz)	103.447	103.126	360.767	372.241
$\sigma(w_n)$ (%)	0.65	0.02	0.26	0.2
$error(\mu(w_n))$ (%)	0.55	-0.02	-0.11	-0.11
$\mu(w_d)$ (Hz)	102.616	103.126	360.694	372.193
$\sigma(w_d)$ (%)	0.56	0.02	0.26	0.2
$error(\mu(w_d))$ (%)	0.43	-0.02	-0.11	-0.12
$\mu(\xi)$	0.117	0.0015	0.0189	0.0153
$\sigma(\xi)$ (%)	7.62	33.59	5.97	4.2
$error(\mu(\xi))$ (%)	3.35	0.87	0.50	0.48

Table 5.26: Eigenvalues identified by MOBAR method, SNR 2, 1 minute of data acquired, 100 Monte Carlo runs for the rotor-bearing system with cross-coupling added to midspan until threshold of stability.

Mode	1^{st} Backward	1^{st} Forward	2^{nd} Backward	2^{nd} Forward
$\mu(w_n)$ (Hz)	96.9681	103.1438	360.7911	372.4897766
$\sigma(w_n)$ (%)	9.70	0.02	0.19	0.19
$error(\mu(w_n))$ (%)	-5.75	0.00	-0.10	-0.05
$\mu(w_d)$ (Hz)	99.7167	103.1435	360.7361	372.4574
$\sigma(w_d)$ (%)	0.75	0.02	0.19	0.19
$error(\mu(w_d))$ (%)	-2.41	0.00	-0.10	-0.04
$\mu(\xi)$	0.11246	0.002359	0.017198	0.012985
$\sigma(\xi)$ (%)	11.30	10.63	17.65	17.71
$error(\mu(\xi))$ (%)	-3.88	57.30	-9.01	-15.13

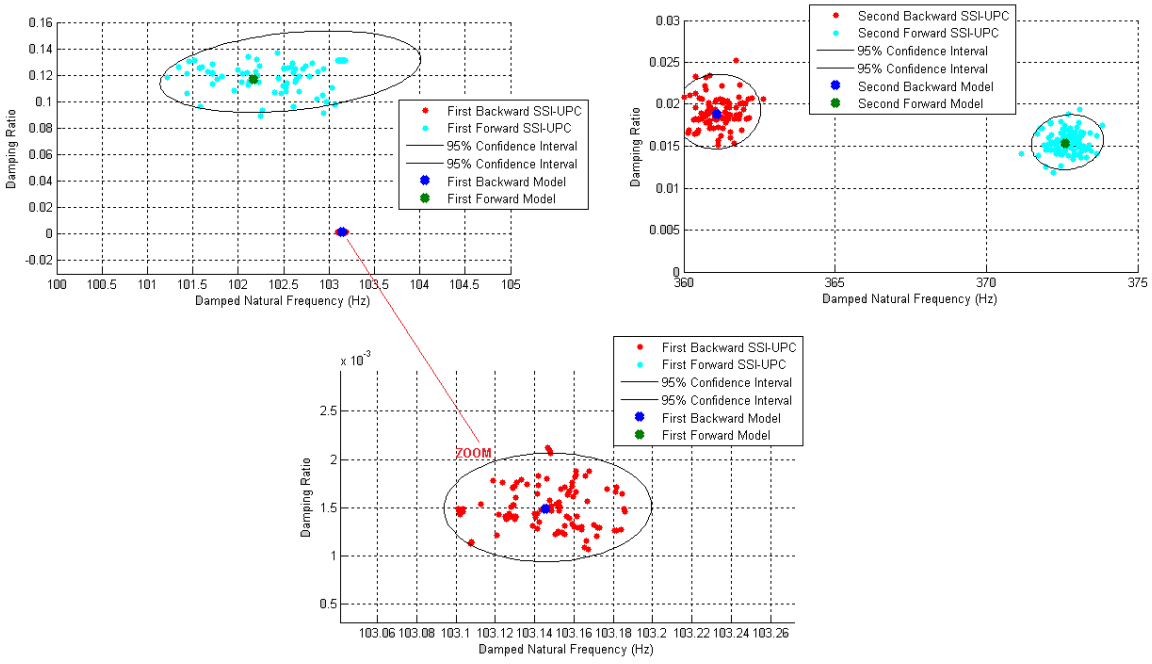

Figure 5.65: Damped Natural Frequency and Damping Ratio identification through SSI-UPC method in 100 Monte Carlo runnings, SNR 2, 1 minute of data acquired per run for the rotor-bearing system at threshold of stability.

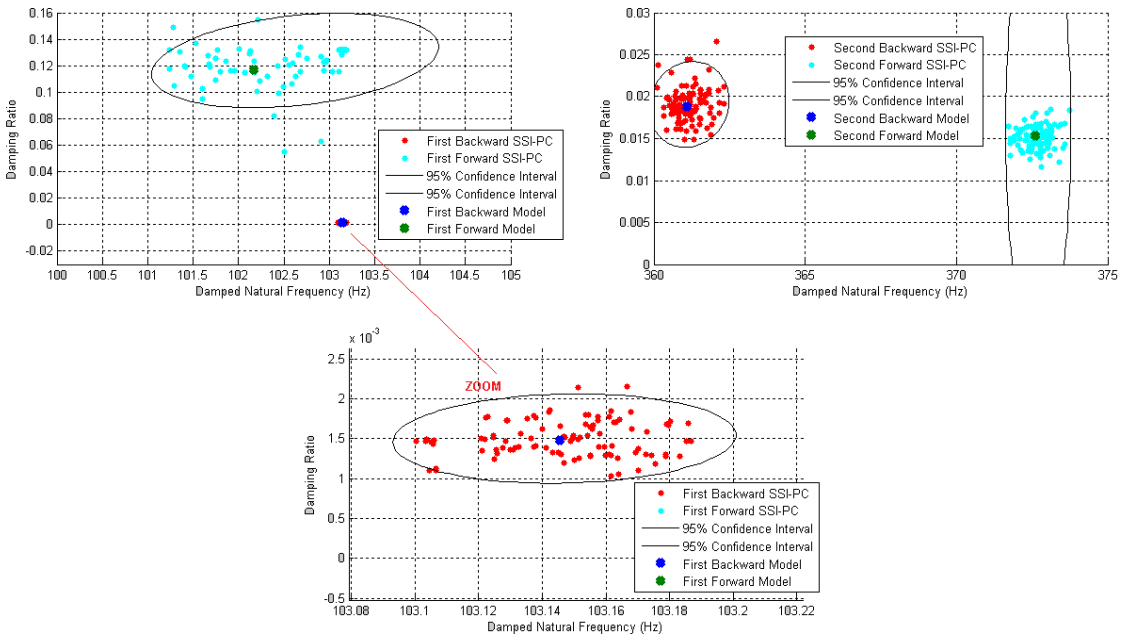

Figure 5.66: Damped Natural Frequency and Damping Ratio identification through SSI-PC method in 100 Monte Carlo runnings, SNR 2, 1 minute of data acquired per run for the rotor-bearing system at threshold of stability.

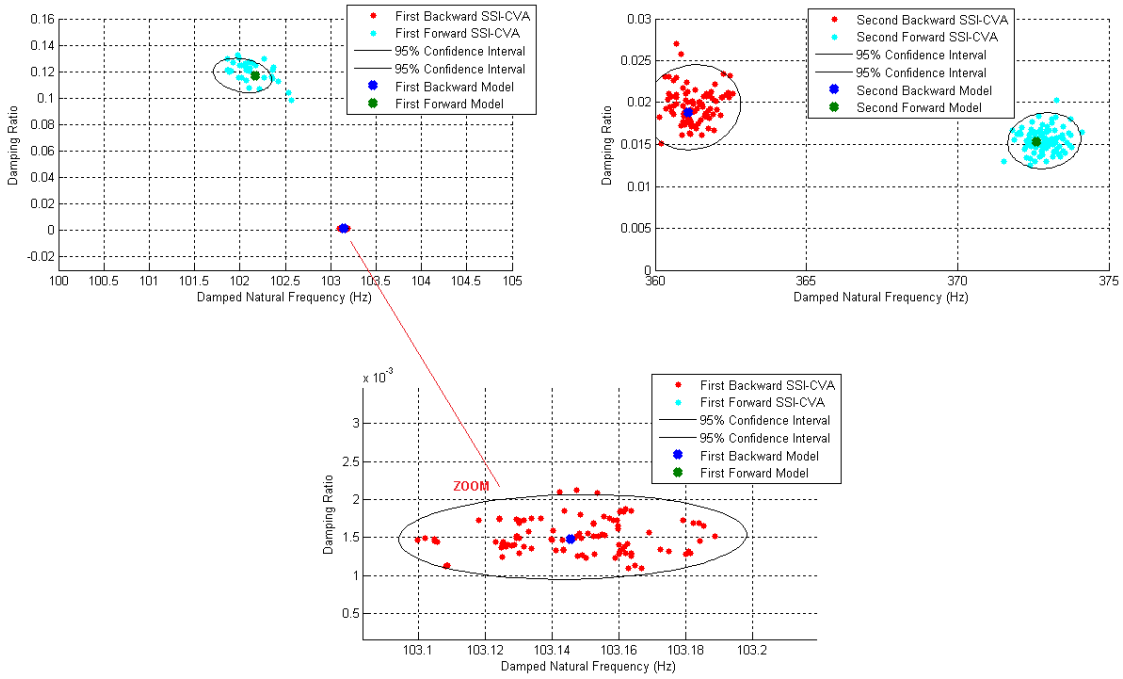

Figure 5.67: Damped Natural Frequency and Damping Ratio identification through SSI-CVA method in 100 Monte Carlo runnings, SNR 2, 1 minute of data acquired per run for the rotor-bearing system at threshold of stability.

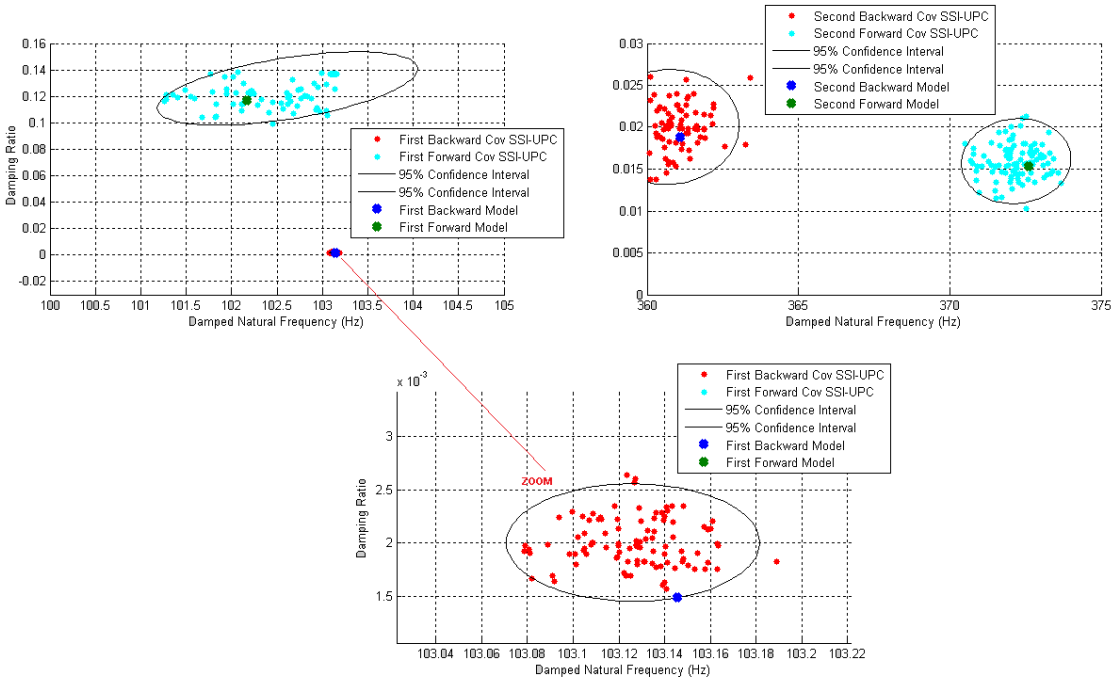

Figure 5.68: Damped Natural Frequency and Damping Ratio identification through Cov SSI-UPC method in 100 Monte Carlo runnings, SNR 2, 1 minute of data acquired per run for the rotor-bearing system at threshold of stability..

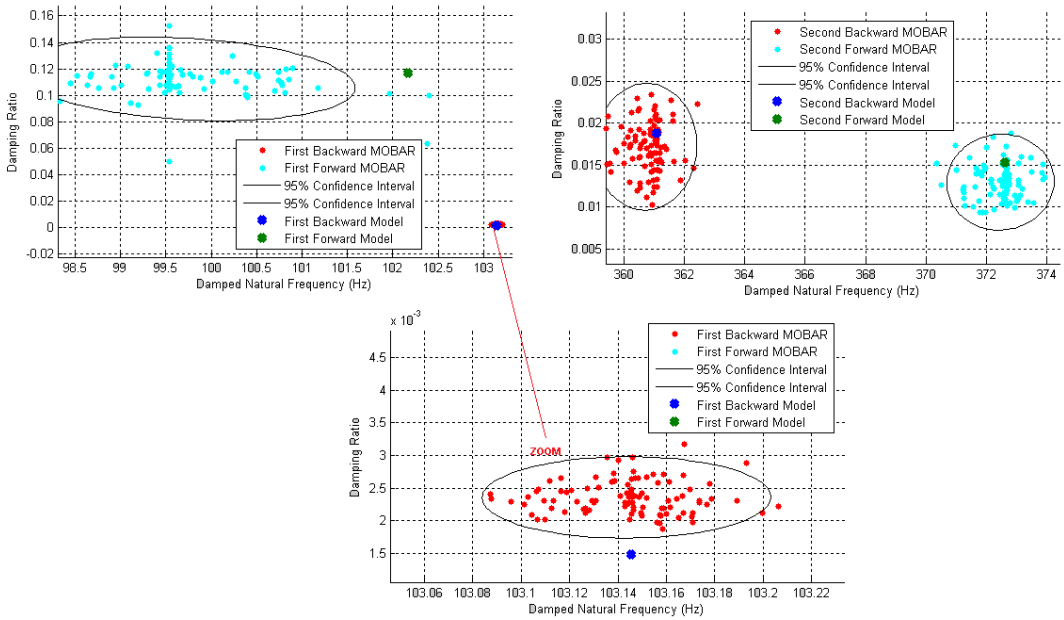

Figure 5.69: Damped Natural Frequency and Damping Ratio identification through MOBAR method in 100 Monte Carlo runnings, SNR 2, 1 minute of data acquired per run for the rotor-bearing system at threshold of stability.

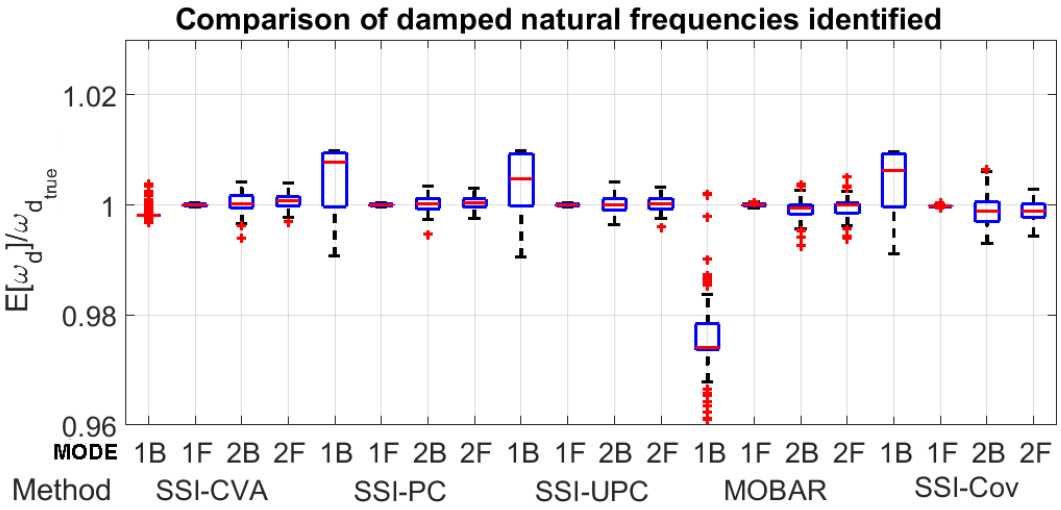

Figure 5.70: Box plot of identified damped natural frequencies for the rotor-bearing system at threshold of stability with SNR 2.

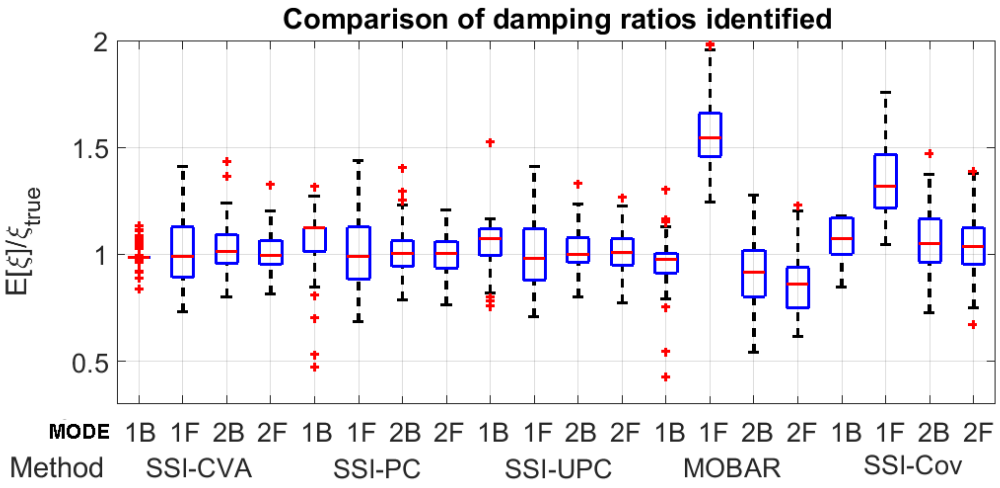

Figure 5.71: Box plot of identified damping ratio for the rotor-bearing system at threshold of stability with SNR 2.

The third model analyzed was the rotor-bearing system, with addition of squeeze-film dampers at both bearings, resulting in a model with an increased damping compared to the previous. The sampling frequency adopted in this discrete model was also 4000 Hz and each Monte Carlo run was performed with 1 minute of response data.

Computational modes were eliminated adopting the same criteria adopted for the previous FEM models analyzed.

Figure 5.72 shows a stabilization diagram over the singular values of PSD matrices plot for a SNR of 2, obtained with SSI-CVA method after applying the computational modes elimination filters.

The high damping of first forward mode is evidenced by looking to the wider peak at the first singular value, near 100 Hz.

Tables 5.27, 5.28, 5.29, 5.30 and 5.31 shows the results for the modal parameters identification from the rotor-bearing-squeeze-film system with a SNR of 2 using SSI-UPC, SSI-PC, SSI-CVA, SSI-UPC Cov and MOBAR respectively. Additionally, figures 5.78 and 5.79 presents the information of these tables in box plot form and figures 5.73, 5.74, 5.75, 5.76 and 5.77 allows a visual inspection of the spread.

The identification of modal parameters with the increased damping has presented higher spread between the realizations, for both the natural frequencies and damping ratio identification, for all the identification techniques applied. This result is attributed to the fast dissipation of transient responses caused by the high damping, what increases the errors of impulse responses or free decays estimation through OMA algorithms.

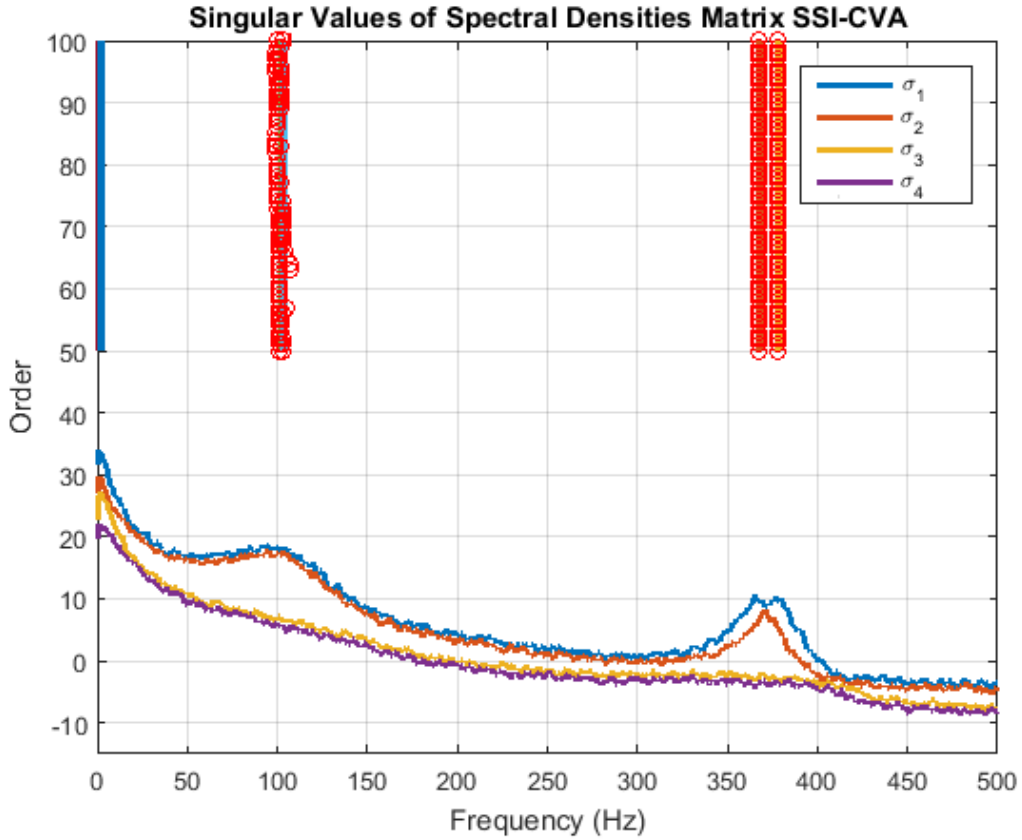

Figure 5.72: Stabilization diagram over Singular Value of Spectral Densities for FEM of rotor-bearing system with addition of squeeze-film damper at both bearings, SNR 2, computational modes eliminated.

Table 5.27: Eigenvalues identified by SSI-UPC method, SNR 2, 1 minute of data acquired, 100 Monte Carlo runs for the rotor-bearing system with addition of squeeze-film damper at both bearings.

Mode	1^{st} Backward	1^{st} Forward	2^{nd} Backward	2^{nd} Forward
$\mu(w_n)$ (Hz)	104.2196	105.4275	367.4931	378.8229
$\sigma(w_n)$ (%)	1.86	2.10	0.18	0.15
$error(\mu(w_n))$ (%)	-0.37	-0.93	-0.01	0.01
$\mu(w_d)$ (Hz)	102.0342	103.4985	367.3775	378.7166
$\sigma(w_d)$ (%)	1.90	1.83	0.18	0.15
$error(\mu(w_d))$ (%)	-0.39	-0.55	-0.01	0.01
$\mu(\xi)$	0.2033	0.1818	0.02503	0.02355
$\sigma(\xi)$ (%)	6.14	29.66	6.16	11.02
$error(\mu(\xi))$ (%)	0.33	-12.83	-0.72	2.03

Table 5.28: Eigenvalues identified by SSI-PC method, SNR 2, 1 minute of data acquired, 100 Monte Carlo runs for the rotor-bearing system with addition of squeeze-film damper at both bearings.

Mode	1^{st} Backward	1^{st} Forward	2^{nd} Backward	2^{nd} Forward
$\mu(w_n)$ (Hz)	106.8943	105.6798	367.607	378.8526
$\sigma(w_n)$ (%)	3.99	2.16	0.21	0.19
$error(\mu(w_n))$ (%)	2.19	-0.69	0.02	0.02
$\mu(w_d)$ (Hz)	104.7171	103.6203	367.492	378.7532591
$\sigma(w_d)$ (%)	4.03	1.84	0.21	0.19
$error(\mu(w_d))$ (%)	2.23	-0.43	0.02	0.02
$\mu(\xi)$	0.20064	0.1829	0.0249	0.0227
$\sigma(\xi)$ (%)	4.52	37.79	8.67	12.49
$error(\mu(\xi))$ (%)	-1.00	-12.31	-1.22	-1.55

Table 5.29: Eigenvalues identified by SSI-CVA method, SNR 2, 1 minute of data acquired, 100 Monte Carlo runs for the rotor-bearing system with addition of squeeze-film damper at both bearings.

Mode	1^{st} Backward	1^{st} Forward	2^{nd} Backward	2^{nd} Forward
$\mu(w_n)$ (Hz)	103.831	105.7146	367.694	378.823
$\sigma(w_n)$ (%)	1.75	1.59	0.16	0.12
$error(\mu(w_n))$ (%)	-0.74	-0.66	0.04	0.01
$\mu(w_d)$ (Hz)	101.6124	103.2657	367.5743	378.7176
$\sigma(w_d)$ (%)	1.78	1.58	0.16	0.12
$error(\mu(w_d))$ (%)	-0.81	-0.78	0.04	0.01
$\mu(\xi)$	0.20538	0.21297	0.02547	0.02355
$\sigma(\xi)$ (%)	4.92	9.37	6.86	6.41
$error(\mu(\xi))$ (%)	1.34	2.11	1.02	2.04

Table 5.30: Eigenvalues identified by Cov SSI-UPC method, SNR 2, 1 minute of data acquired, 100 Monte Carlo runs for the rotor-bearing system with addition of squeeze-film damper at both bearings.

Mode	1^{st} Backward	1^{st} Forward	2^{nd} Backward	2^{nd} Forward
$\mu(w_n)$ (Hz)	104.755	106.301	367.483	378.657
$\sigma(w_n)$ (%)	2.71	2.51	0.18	0.16
$error(\mu(w_n))$ (%)	0.14	-0.10	-0.01	-0.03
$\mu(w_d)$ (Hz)	102.5766	104.1846	367.363	378.556
$\sigma(w_d)$ (%)	2.52	2.47	0.18	0.16
$error(\mu(w_d))$ (%)	0.14	0.11	-0.01	-0.03
$\mu(\xi)$	0.1983	0.1942	0.02546	0.02311
$\sigma(\xi)$ (%)	20.33	20.39	7.68	6.83
$error(\mu(\xi))$ (%)	-2.16	-6.88	0.98	0.11

Table 5.31: Eigenvalues identified by MOBAR method, SNR 2, 1 minute of data acquired, 100 Monte Carlo runs for the rotor-bearing system with addition of squeeze-film damper at both bearings.

Mode	1^{st} Backward	1^{st} Forward	2^{nd} Backward	2^{nd} Forward
$\mu(w_n)$ (Hz)	104.4528	105.1569	366.2431	377.7185
$\sigma(w_n)$ (%)	0.53	0.80	0.48	0.26
$error(\mu(w_n))$ (%)	-0.15	-1.18	-0.35	-0.28
$\mu(w_d)$ (Hz)	102.5439	103.2909	366.168	377.643
$\sigma(w_d)$ (%)	0.53	0.83	0.48	0.26
$error(\mu(w_d))$ (%)	0.10	-0.75	-0.34	-0.28
$\mu(\xi)$	0.19011	0.1874	0.01982	0.01981
$\sigma(\xi)$ (%)	4.42	4.23	20.67	11.90
$error(\mu(\xi))$ (%)	-6.19	-10.15	-21.37	-14.17

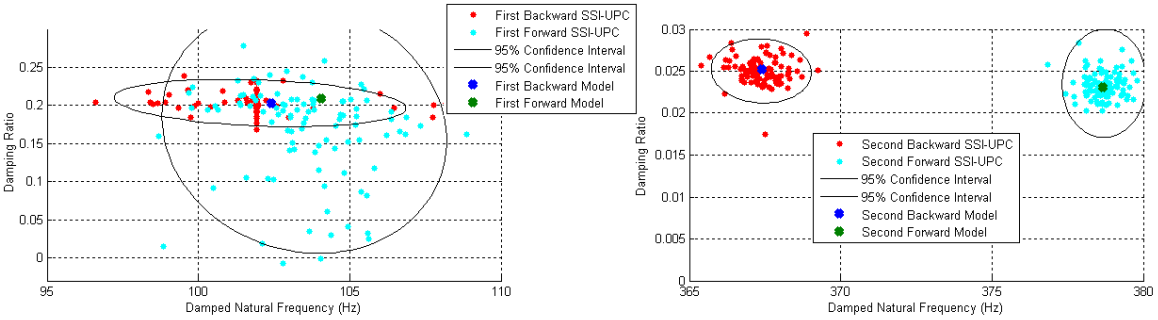

Figure 5.73: Damped Natural Frequency and Damping Ratio identification through SSI-UPC method in 100 Monte Carlo runnings, SNR 2, 1 minute of data acquired per run for the rotor-bearing with addition of squeeze-film damper at both bearings.

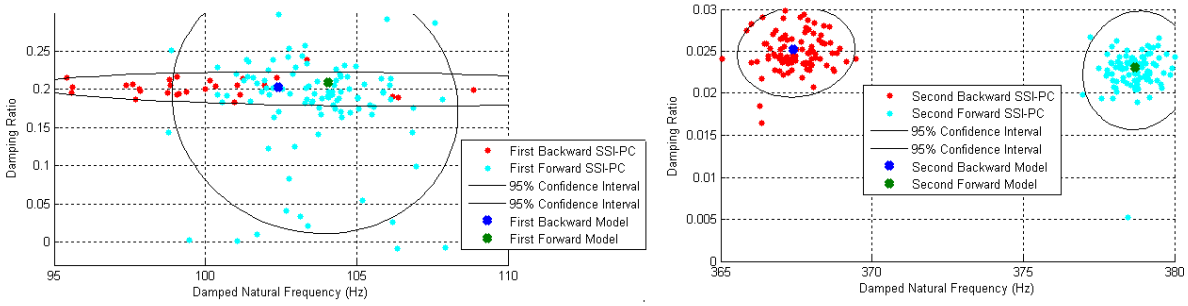

Figure 5.74: Damped Natural Frequency and Damping Ratio identification through SSI-PC method in 100 Monte Carlo runnings, SNR 2, 1 minute of data acquired per run for the rotor-bearing system with addition of squeeze-film damper at both bearings.

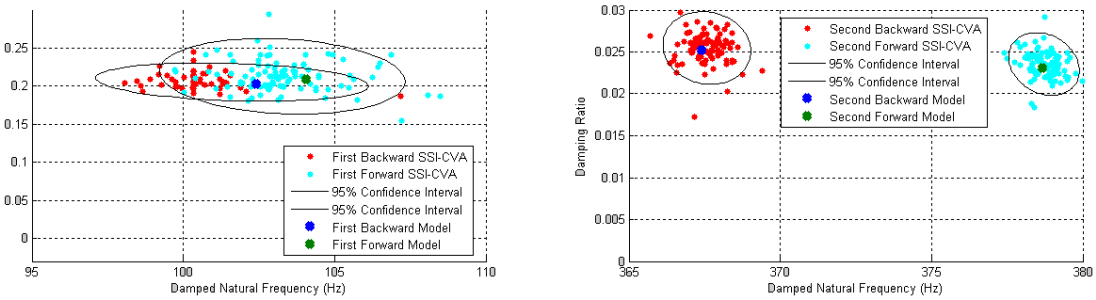

Figure 5.75: Damped Natural Frequency and Damping Ratio identification through SSI-CVA method in 100 Monte Carlo runnings, SNR 2, 1 minute of data acquired per run for the rotor-bearing system with addition of squeeze-film damper at both bearings.

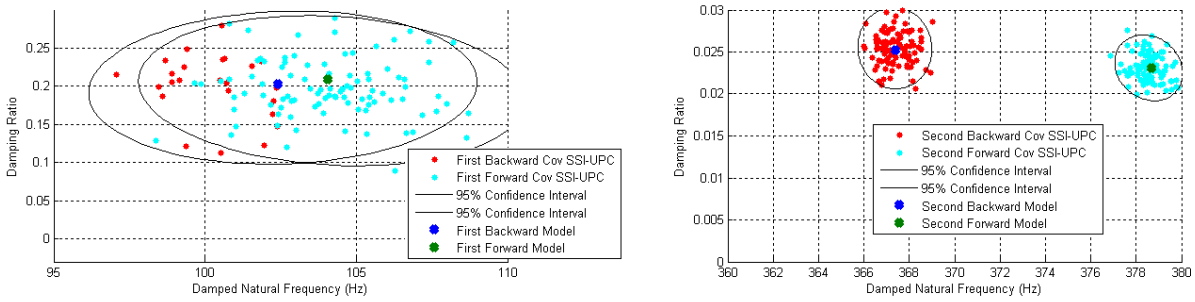

Figure 5.76: Damped Natural Frequency and Damping Ratio identification through Cov SSI-UPC method in 100 Monte Carlo runnings, SNR 2, 1 minute of data acquired per run for the rotor-bearing system with addition of squeeze-film damper at both bearings.

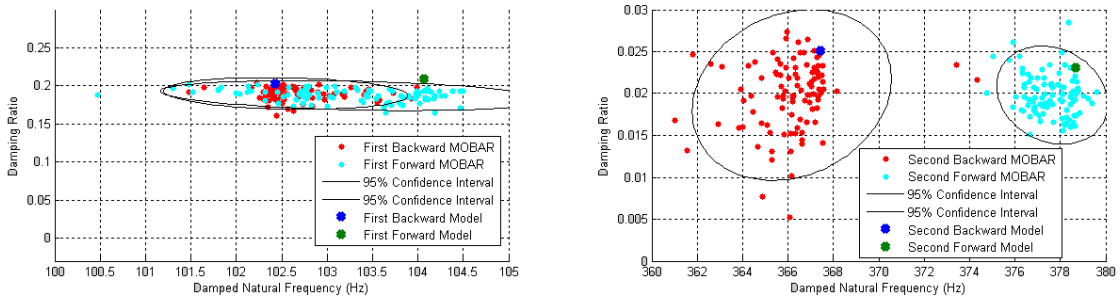

Figure 5.77: Damped Natural Frequency and Damping Ratio identification through MOBAR method in 100 Monte Carlo runnings, SNR 2, 1 minute of data acquired per run for the rotor-bearing system with addition of squeeze-film damper at both bearings.

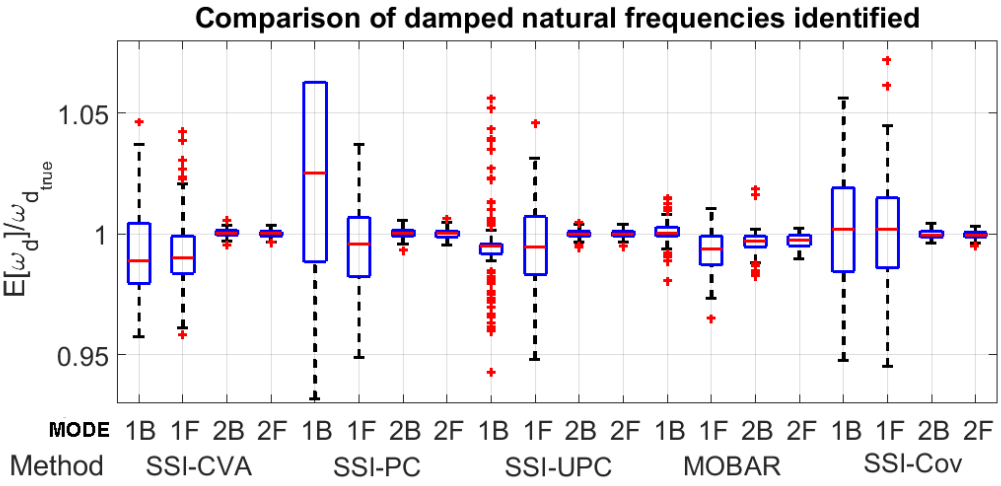

Figure 5.78: Box plot of identified damped natural frequencies for the rotor-bearing system with addition of squeeze-film damper at both bearings, SNR 2.

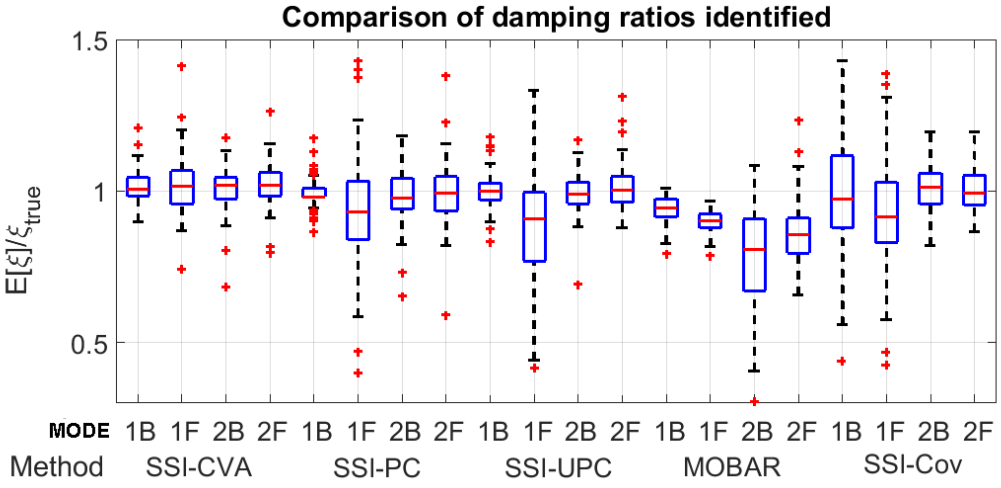

Figure 5.79: Box plot of identified damping ratio for the rotor-bearing system with addition of squeeze-film damper at both bearings, SNR 2.

5.2 Field Measurements and Signal Processing

The evaluated compressor has two pairs of displacement sensors, assembled in directions named X and Y, with an angle of 90 degrees between them. One pair is located near the drive end (DE) journal bearing and the other near the non-drive end (NDE) journal bearing. Figure 5.80 show a diagram representing the vibration and bearings pad temperature sensors of the complete compressor train, helping to visualize the 4 radial displacement sensors of the compressor.

Data from these four proximity sensors was collected during operation, by connecting a data collector to the Machinery Protection System buffered output channels. The sampling frequency was set to 128 kHz, and raw waveforms for each sensor were collected simultaneously during 25 minutes. Channels 1 and 2 correspond to X and Y direction at the NDE, respectively, while channels 3 and 4 correspond to X and Y direction at the DE, respectively.

The operational conditions during the data acquisition are shown in table 5.32, and compared with the Design and Shop Stability Test conditions.

Table 5.32: Design, Shop Test and Field Conditions

	Design	**Shop**	**Field**
Aero Case	Guarantee	Vacuum	H_2+HC
Speed (rpm)	13660	13660	13860
P_s (bara)	9.032	-	9.74
T_s (°C)	38	-	31.6
P_d (bara)	23.539	-	23.34
T_d (°C)	125	-	119.5
Oil Inlet (°C)	43.3 - 54.4	46.6	42

Figure 5.81 shows the raw waveforms, that presents very low peak-to-peak amplitudes (3 microns). Highlighted by the red circles, scratches on the shaft, located in the sensor's tracks at both ends of the compressor, create large 10-15 microns spikes in the signals.

Since harmonics of running speed lower the SNR of the modes of interest, it is important to minimize those harmonics created by the shaft scratches. To do so, all the signals were low pass filtered and than down-sampled. The final processed waveform is shown in figure 5.81, where it can be observed the effect of scratches have been effectively eliminated.

The low-pass filter followed by the down-sampling is known as decimation and it can be helpful on making the number of block lines s used to build the Hankel matrices suitable to avoid issues related with low eigenfrequencies compared with the sampling ratio (see WAGNER *et al.* [52]). As proposed by REYNDERS and

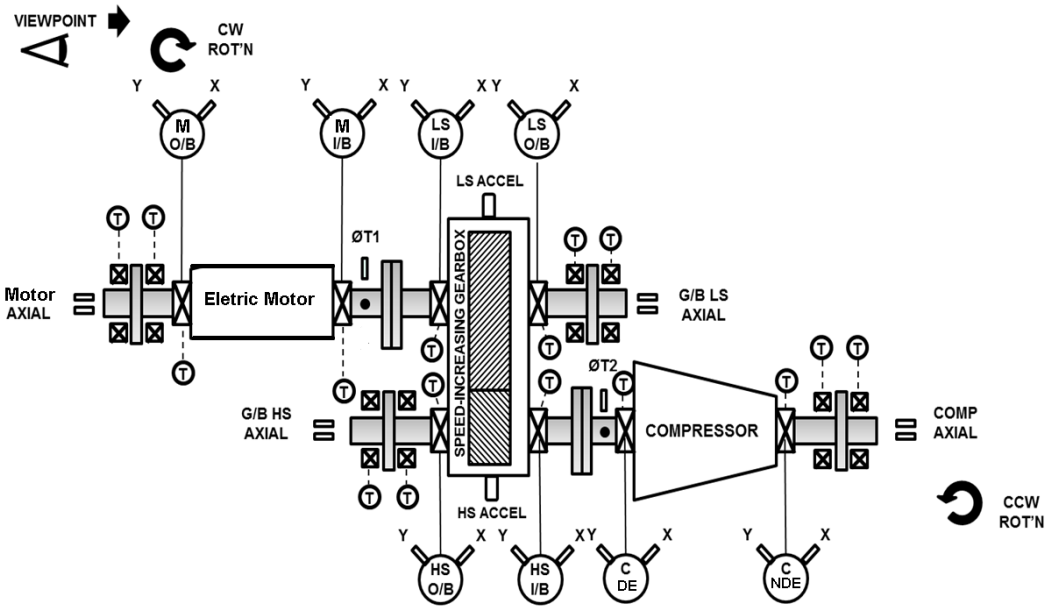

Figure 5.80: Diagram showing vibration and bearing temperature instruments of the analyzed compressor

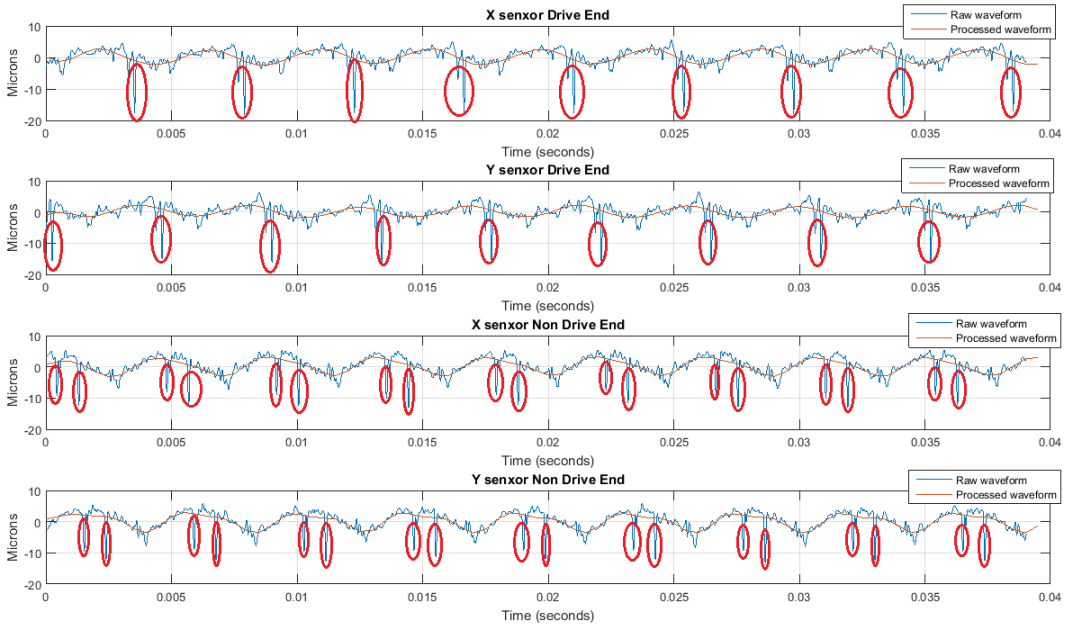

Figure 5.81: Raw waveforms showing the scratches and filtered waveforms.

DE ROECK [53], s can be chosen by equation 5.2, where f_s and f_0 correspond to sampling frequency and lowest frequency of interest, respectively.

$$s \geq \frac{f_s}{2f_0} \tag{5.2}$$

Moreover, the acquisition duration should be large enough to allow a good estimation of the covariance matrix.

The processed waveforms were applied directly in OMA SSI data driven methods. For covariance driven methods it was applied Welch's method to find the PSD, with FFT blocks containing 4096 samples, applying Hanning window to each block and averaging the FFTs with overlap of 75%. After this the covariances were calculated through the Inverse Fast Fourier Transform of the obtained PSD. The resulting PSDs G_{ij} between channels i and j are shown in Figure 5.82, where the dominant frequency component in each is the compressor's running speed. One can also clearly observe the drive motor's $1\times$ and $2\times$ running speed components near 1800 cpm and 3600 cpm.

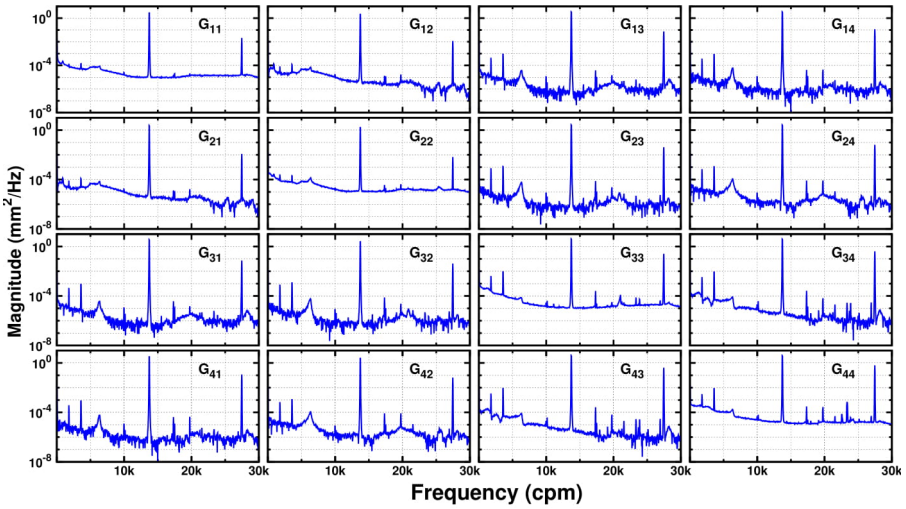

Figure 5.82: Measured PSD matrix $\boldsymbol{G}(\boldsymbol{\omega})$

Based on the shop SVT measurements and predictions, the 1F mode is expected to be near 6000 cpm. All of the power spectrum indicate a peak near this frequency. The singular values σ of the 4×4 PSD matrix $\boldsymbol{G}(\boldsymbol{\omega})$, presented in Figure 5.83, confirm the presence of the mode(s) in the data, even though its response is almost four orders of magnitude smaller than the synchronous vibration.

The final step of signal processing effort was to calculate the covariances, by taking the inverse Fourier transform of the averaged PSDs. Figure 5.84 shows the auto-correlation functions obtained.

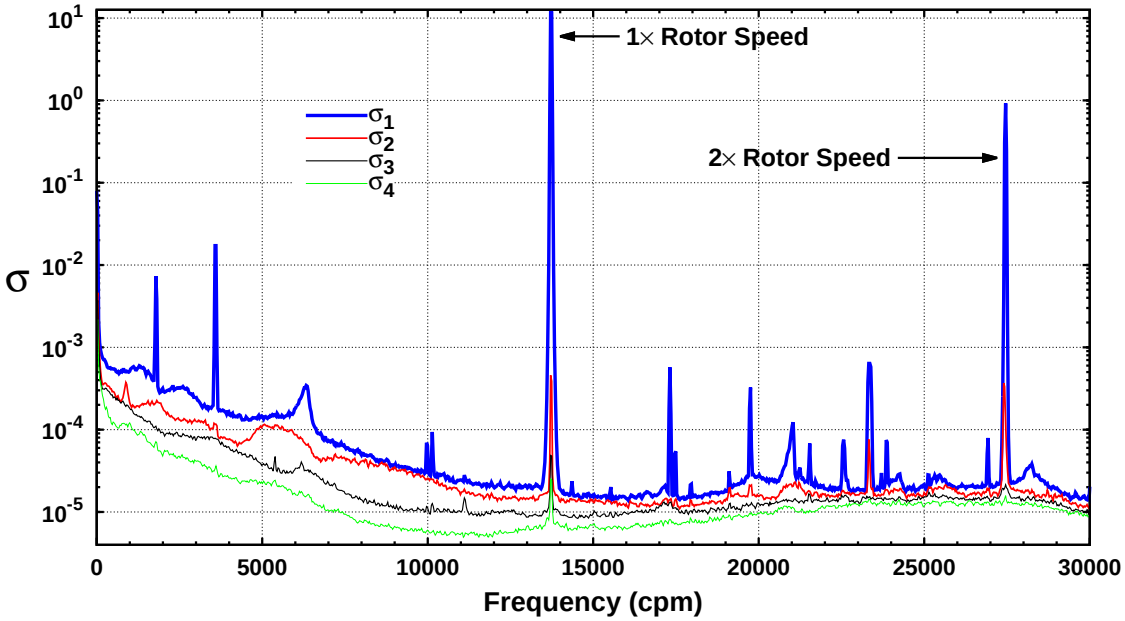

Figure 5.83: Singular values of power spectral density matrix $G(\omega)$

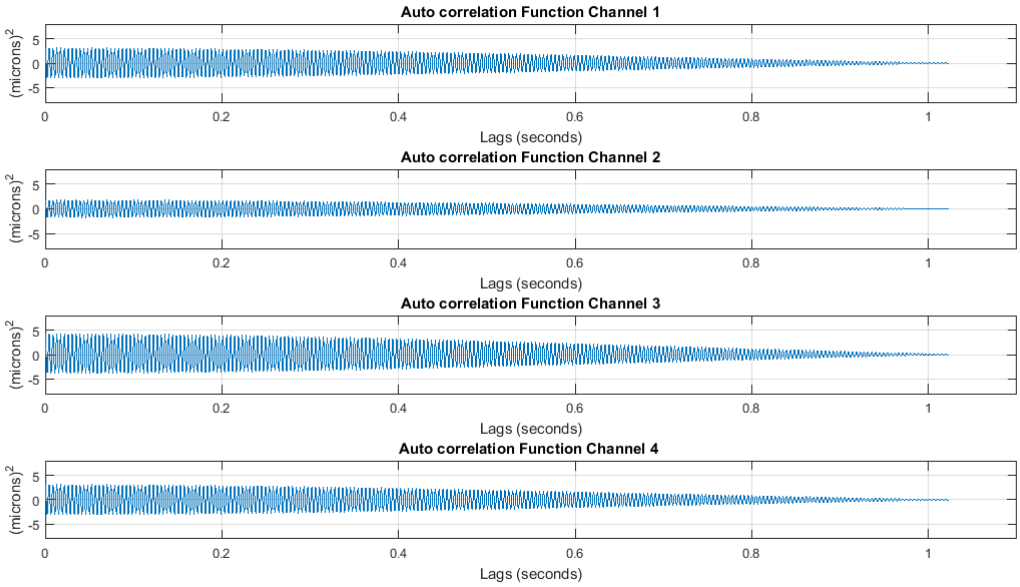

Figure 5.84: Autocorrelation Functions

5.2.1 Identification from Centrifugal Compressor in Field Operation

Figures 5.85(a) and 5.85(b) present the resulting modal parameters identified by the covariance-based and data-driven identification techniques, respectively using the first four minutes of data.

The upper part of these figures shows the stability spectrum for all the system modes identified during these order variations. The lower part of each figure presents a stabilization diagram to show the identified frequencies for each model order. For information purposes, the singular value results from Figure 5.83 are also presented within the stabilization diagrams.

All of the techniques accurately identify the compressor and motor $1\times$ and $2\times$ harmonics of their rotor speeds as, effectively, undamped modes. The results also show that the SSI techniques have identified relatively few modes below the compressor's running speed, but a large amount of modes in the frequency region above compressor speed. Some of these high frequency modes are associated with computational or noise modes, not physical modes, as evidenced by the lack of any clearly discernible peaks in the singular values at these frequencies.

By comparison, Figure 5.85(b) indicates that MOBAR does not identify these spurious, noise modes. This is a direct result of MOBAR's formulation that filters out noise poles by placing them inside the discrete time unit circle [26]. Relative to the other techniques, MOBAR has identified more modes in the subsynchronous region, in particular, several with relatively high damping levels that are clearly present in the σ_1 and σ_2 results.

Depending on the order, Figures 5.85 and 5.86 show that all of the techniques identify two modes around the σ_1 and σ_3 peaks near 6000 cpm. These modes are the primary ones of interest, the rotor's first sister modes, 1F and 1B.

By looking to the Averaged Kurtosis of measurement signals at figure 5.87, it is possible to see a kurtosis of 2.4 and 2.2 at 1800 and 3600 cpm and a kurtosis of 1.5 at running speed, evidencing the non gaussian nature of signal at these frequencies, while near 6000 cpm, a kurtosis of 3 was found, evidencing the modal nature of the poles identified in this region.

For the SSI methods, significant spread of 1F damping estimates occurs at low model orders. Greater consistency in the 1F mode's damping estimates is achieved at higher orders, once the SSI methods are able to identify both the first forward and first backward sister modes. This consistency is illustrated in Figure 5.88.

Once 25 minutes of data were acquired, it was possible to perform the analysis several times, using samples of 4 minutes of data on each run, with an overlap of 75 % between the previous and next samples, allowing to see the spread of modal

parameters identification through the different samples. Figures 5.89, 5.90, 5.91, 5.92 and 5.93 shows the obtained results for Covariance Driven SSI-UPC and MOBAR, and Data Driven SSI-UPC, PC and CVA respectively.

The mean value of damping ratio ζ and damped natural frequencies w_d identified from the several runnings for the first forward and backward modes using OMA during field operation and identified during vacuum running in the Factory Stability Test with magnetic exciter are summarized in tables 5.33 and 5.34. All the presented results are for MCS.

Estimates for the 1F mode agree very well between the different techniques applied, as shown in Figure 5.94. The 1F log decrement estimates fall around approximately 0.12. This value correlates well with that predicted by the first simplified model correction approach from the shop SVT, where δ_{1F} was predicted to be 0.12–0.14. The agreement between different identification techniques, as well as the shop SVT results, provides confidence in the 1F modal estimates.

From the different realizations performed, significant variation exists in the 1B modal damping estimates obtained from the data-driven SSI-PC and UPC techniques. On the contrary, little variation is present in MOBAR, Covariance Driven SSI-UPC and Data Driven SSI-CVA's 1B modal damping estimates.

The agreement between different output only estimation techniques gives confidence in the obtained results, for a smooth running compressor, exposed to very low density gas excitation, with considerable scratches in the sensors tracks.

Several other modes were identified that are of interest. Observed as a peak in the σ_2 results near 830 cpm, all of the techniques, with sufficient model order, identify a mode here. However, the techniques are unable to confidently identify this mode's damping, although it appears to be moderate ($\zeta > 5\%$).

At approximately 5000 cpm, another mode was identified by most of the techniques. The σ_2 results near this frequency suggest a well-damped mode, which correlates well with MOBAR's estimate near 20% modal damping. However, the DD-SSI techniques estimate its damping to be much lower, less than 5%.

The shop SVT identified a mode near 20,000 cpm that was suspected to be associated with one of the rotor's second sister modes. So, it was hoped that OMA would be able to provide further evidence as to their location. Although several cross spectrum (see G_{13} and G_{24} in Figure 5.82) show some modal-like response near 20,000 cpm, another signal with undamped nature dominates at this frequency. As a result, all of the techniques, unfortunately, identify a pole that is too lightly damped to be the rotor's second mode.

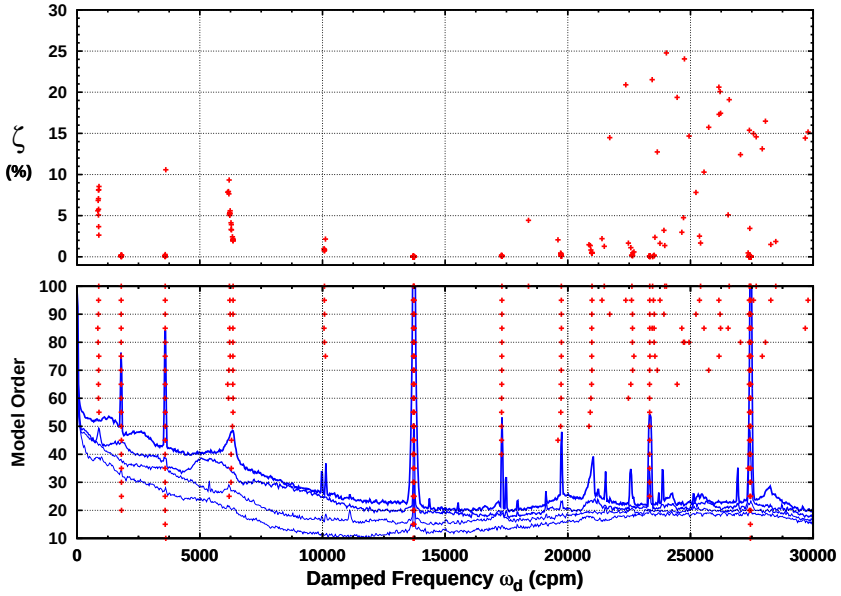

(a) COV-SSI

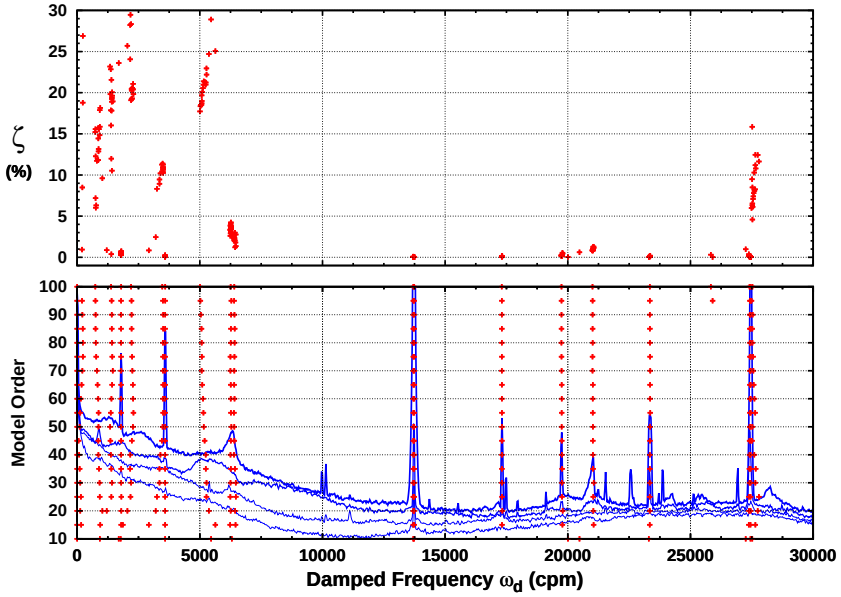

(b) MOBAR

Figure 5.85: Identified parameters vs. order variation for correlation-based ID techniques

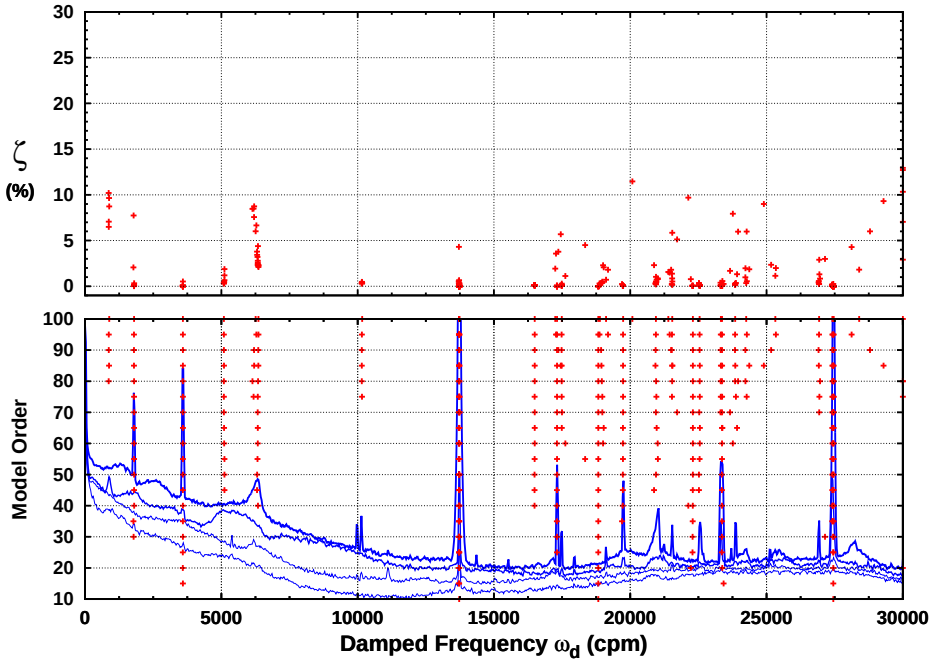

(a) DD-SSI-CVA

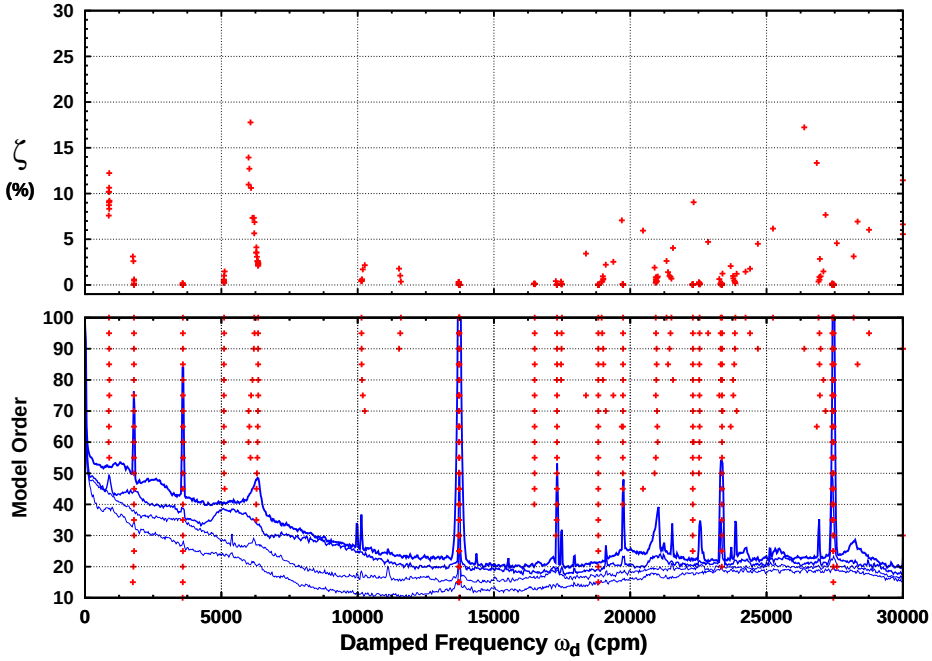

(b) DD-SSI-UPC

Figure 5.86: Identified parameters vs. order variation for data-driven SSI techniques

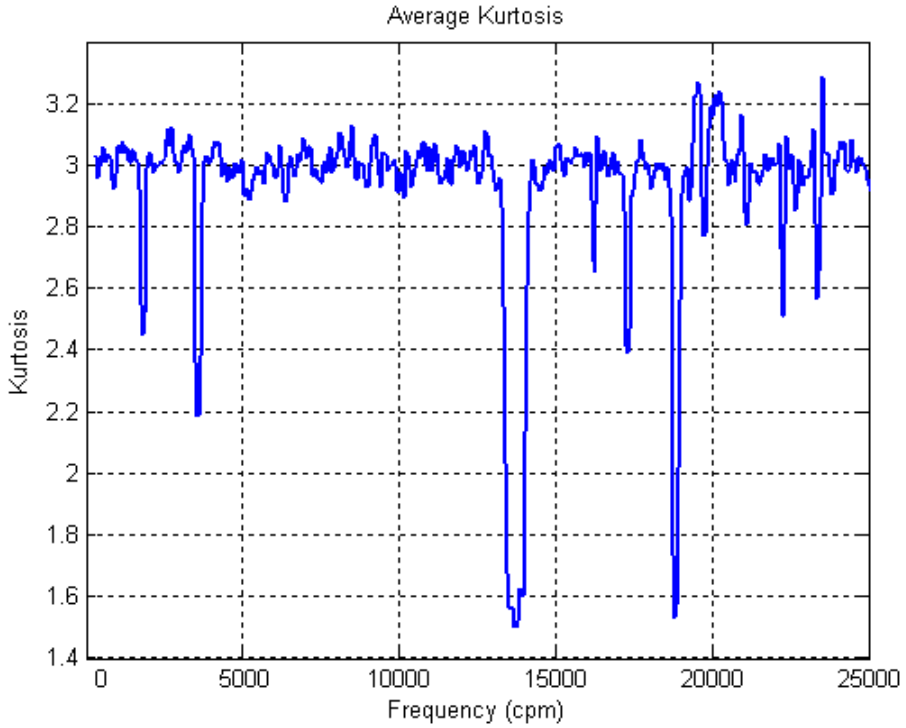

Figure 5.87: Average Kurtosis of measurement signals.

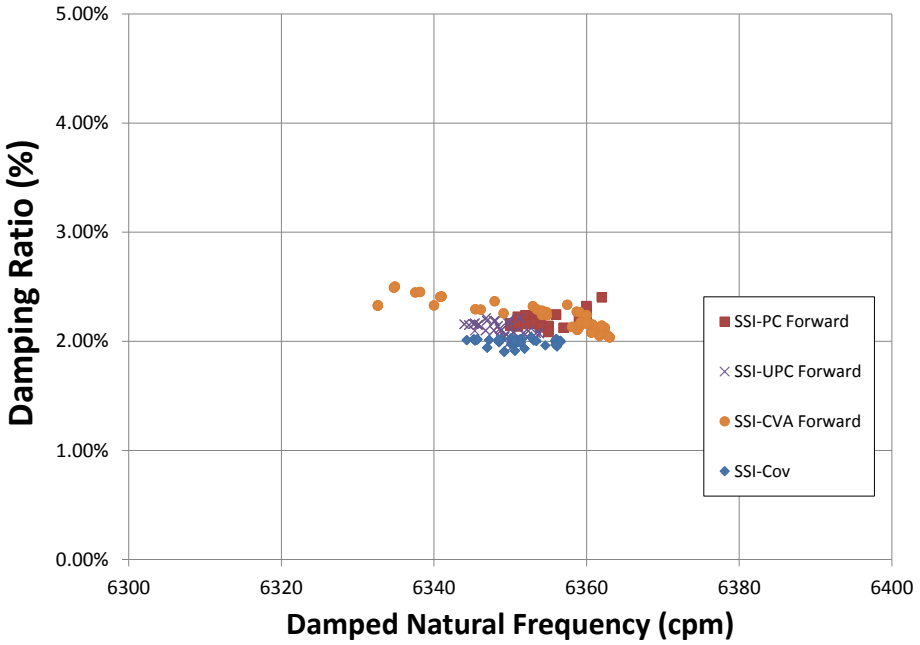

Figure 5.88: Damping of first forward mode, identified by SSI methods in orders above the minimum able to identify the first forward and backward modes.

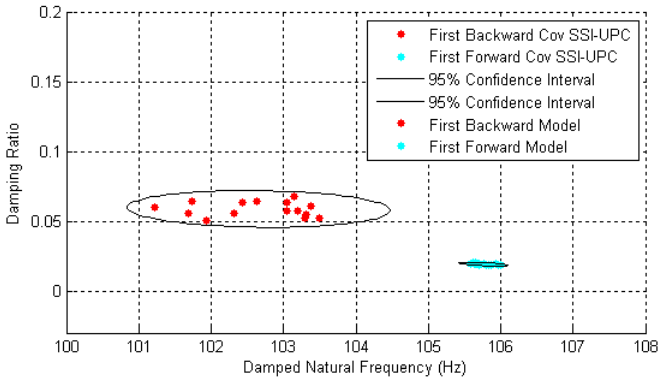

Figure 5.89: Modal parameters of first backward and forward modes identified by Covariance Driven SSI-UPC method.

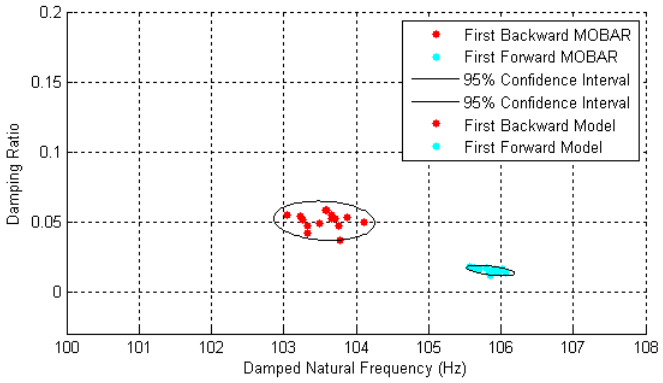

Figure 5.90: Modal parameters of first backward and forward modes identified by Covariance Driven MOBAR method.

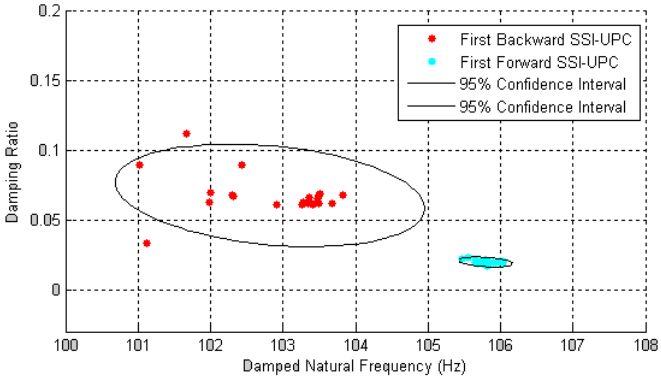

Figure 5.91: Modal parameters of first backward and forward modes identified by Data Driven SSI-UPC method.

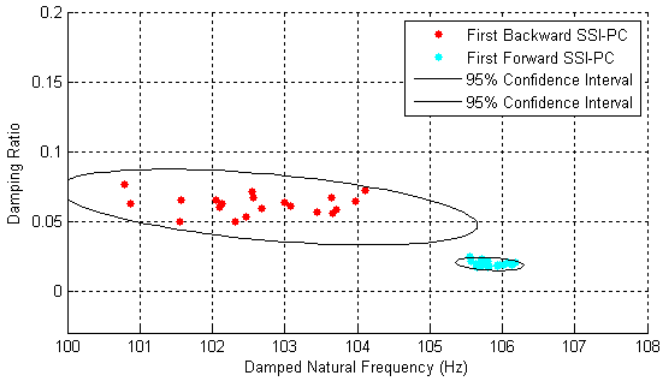

Figure 5.92: Modal parameters of first backward and forward modes identified by Data Driven SSI-PC method.

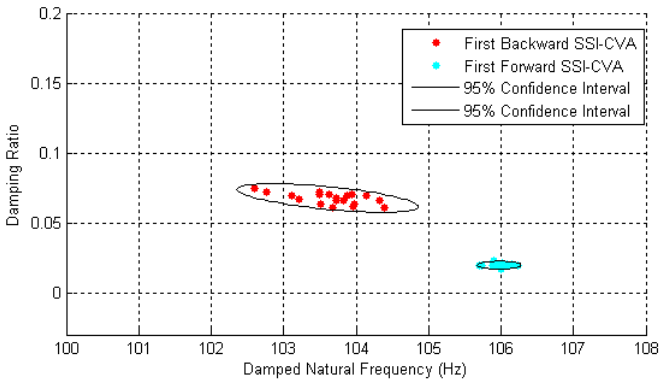

Figure 5.93: Modal parameters of first backward and forward modes identified by Data Driven SSI-CVA method.

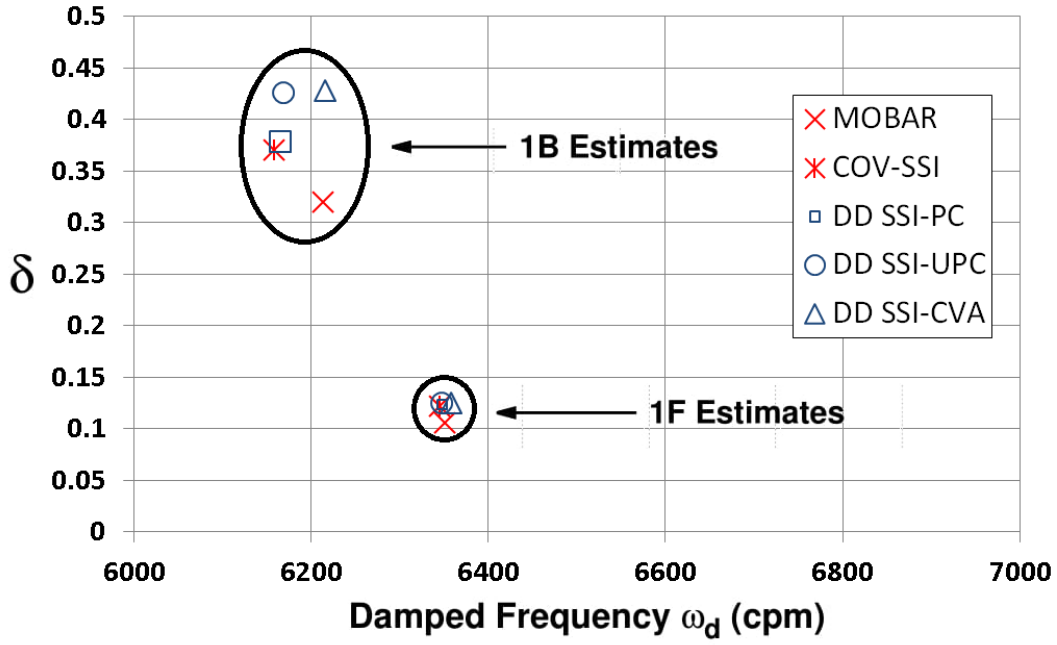

Figure 5.94: Stability spectrum of first rotor modes' parameter estimates using different ID techniques

Table 5.33: Modal Identification Results

	SSI-PC	**SSI-UPC**	**SSI-CVA**	**MOBAR**
Operational Condition	Field	Field	Field	Vacuum
1st Forward w_d(cpm)	6349.45	6345.7	6358.65	6307
1st Forward ζ(%)	1.943	1.933	1.982	1.94
1st Backward w_d(cpm)	6165.66	6159.29	6216.47	6155
1st Backward ζ(%)	6.01	5.883	6.777	4.02

Table 5.34: Modal Identification Results

	SSI-Cov	**MOBAR**	**MOBAR**
Operational Condition	Field	Field	Vacuum
1st Forward w_d(cpm)	6345.70	6351.48	6307
1st Forward ζ(%)	1.93	1.68	1.94
1st Backward w_d(cpm)	6159.29	6213.57	6155
1st Backward ζ(%)	5.88	5.08	4.02

Chapter 6

Conclusions

The focus of the present work was to analyze OMA methods applied to centrifugal compressors, highlighting aspects of OMA that are specific to rotating machines. The investigation was related to aspects as signal processing, parameter setting, elimination of computational and excitation modes and finally the modal parameters extraction in each of analyzed methods. The main conclusions associated to this investigation are described next.

Firstly, time domain OMA methods were applied to synthetic data from a simple model with three mass-spring-damper elements subject to white noise excitation. The spread observed over the different realizations has highlighted the advantages of performing many realizations in order to have a better identification. Meaningful reduction on the spread of identification parameters was obtained by increasing the acquisition time span, highlighting the importance of choosing properly the time span when performing a modal identification through OMA methods.

Secondly, the OMA methods were applied to synthetic data from a finite element model with three different levels of damping subject to white noise excitation. A time span of just 1 minute per realization was enough to provide good identification results, with all the methods analyzed here. One could observe reliable identifications of the first and second forward rotor modes. This behavior was noticed for different levels of damping. Means to recognize between a harmonic and a low damped mode were discussed with help of the model at threshold of stability. The SVD's modulation shape with the closed spaced backward and forward modes helps to identify the modal response, mainly because although at threshold of stability the damping of first forward mode is low, the first backward mode usually present higher damping, showing a smooth modulation at second SVD. Another useful tool applied to the model was the calculation of Kurtosis of responses, after bandpass filter them at the range of interest, allowing to verify the Gaussian or harmonic nature of identified poles, that is related with structural modes and excitation filter respectively.

Finally, the identification of modal parameters from the hydrogen compressor was performed. It was necessary to increase the time span to 4 minutes per realization, in order to reduce the deviation of modal parameters identification between realizations. The cause for that is attributed to the presence of superimposed loads, non white noise characteristics of the stochastic excitation and small variations of process parameters during the acquisition time, that are expected in any industrial plant. The findings from this system can be summarized as the following:

1. Although four orders of magnitude lower than the predominant, synchronous vibrations, the 1F mode's presence was easily distinguished through the use of various signal processing techniques, particularly averaging in the frequency domain over a long time span. Very close correlation in the 1F mode's frequency and damping estimates was obtained from five different time domain, output-only, identification techniques. Further confidence is provided by the fact that the mode's estimated frequency and damping are, as expected, very close to those measured during the shop SVT.

2. Very good agreement between the different ID techniques' studied was observed at estimates for the 1F mode. Compared to the other ID techniques, dramatically fewer computational, noise modes were identified by MOBAR, a direct result of its backward formulation which acts to filter such modes.

3. Like the shop SVT, field OMA identified the rotor's first backward mode to be in close proximity to its sister forward mode with slightly higher damping. Unfortunately, the compressor's second rotor modes could not be identified with any great confidence.

Application of OMA methods to the hydrogen compressor has reached a promising outcome, since it has shown that OMA can be successful for services or machine applications with relatively low, ambient excitations. Furthermore, sophisticated identification techniques are not always necessary to estimate modal locations. If sufficient ambient excitation is present, useful information on the modal picture can be obtained by simply studying the averaged PSDs and their singular values, just as one might do with frequency response functions.

It must be acknowledged that significant uncertainties may exist in the modal parameter estimates, particularly, their damping level. While signal processing and identification techniques can provide high confidence in a mode's estimated damped natural frequency, estimation of a mode's damping ratio will always have less certainty. Leakage, noise and modal proximity pose a continuous challenge to accurate identification of modal damping. In the end, what modes are identified and the

quality of their modal parameter estimates is highly dependent on the analyst's expertise with the signal processing and identification techniques employed, just as much as on the information contained within the raw measured data.

Bibliography

[1] BRINCKER, R., VENTURA, C. *Introduction to Operational Modal Analysis*. 2 ed. Chichester, United Kingdom, Wiley, 2015.

[2] PETTINATO, B. C., CLOUD, C. H., CAMPOS, R. S., et al. "Shop acceptance testing of compressor rotordynamic stability and theoretical correlation". In: *Proceedings of the 39th Turbomachinery Symposium*. Texas A&M University. Turbomachinery Laboratories, 2010.

[3] VAN OVERSCHEE, P., DE MOOR, B. *Subspace identification for linear systems: Theory—Implementation—Applications*. Springer Science & Business Media, 1996.

[4] API 617, S. "617, 8th edition", *Axial and Centrifugal Compressors and Expander-Compressors for Petroleum, Chemical and Gas Industry Services," Eighth Edition, American Petroleum Institute, Washington, DC*, 2014.

[5] CLOUD, H. "Stability of rotors supported by tilting pad journal bearings [Ph. D. thesis]". 2007.

[6] KOCUR, J. A., NICHOLAS, J. C., LEE, C. C. "Surveying tilting pad journal bearing and gas labyrinth seal coefficients and their effect on rotor stability". In: *36th Turbomachinery Symposium, Turbomachinery Laboratory, Texas A&M University, College Station, TX, September*, pp. 10–13, 2007.

[7] GUGLIELMO, A., BALDASSARRE, L., CATANZARO, M., et al. "Operational modal analysis application for the measure of logarithm decrement in centrifugal compressor". In: *Proceedings of the 44th Turbomachinery Symposium*. Turbomachinery Laboratories, Texas A&M Engineering Experiment Station, 2015.

[8] REYNDERS, E. "System identification methods for (operational) modal analysis: review and comparison", *Archives of Computational Methods in Engineering*, v. 19, n. 1, pp. 51–124, 2012.

[9] AKAIKE, H. "Markovian representation of stochastic processes and its application to the analysis of autoregressive moving average processes", *Annals of the Institute of Statistical Mathematics*, v. 26, n. 1, pp. 363–387, 1974.

[10] BENDAT, J. S., PIERSOL, A. G. "Engineering applications of correlation and spectral analysis", *New York, Wiley-Interscience, 1980. 315 p.*, 1980.

[11] IBRAHAM, S. "A method for the direct identification of vibration parameter from the free responses", *Shock and Vibration Bulletin*, v. 47, n. 4, 1977.

[12] VOLD, H., KUNDRAT, J., ROCKLIN, G. T., et al. *A multi-input modal estimation algorithm for mini-computers*. Relatório técnico, SAE Technical Paper, 1982.

[13] JUANG, J., PAPPA, R. "An Eigensystem Realization Algorithm (ERA) for Modal Parameter Identification and Model Reduction", *Journal of Guidance, Control and Dynamics*, v. 8, n. 5, pp. 620–627, 1985.

[14] JAMES, G., CARNE, T. G., LAUFFER, J. P., et al. "The natural excitation technique (NExT) for modal parameter extraction from operating structures", *Modal Analysis-the International Journal of Analytical and Experimental Modal Analysis*, v. 10, n. 4, pp. 260, 1995.

[15] YUEN, K.-V., KATAFYGIOTIS, L. S. "Bayesian time–domain approach for modal updating using ambient data", *Probabilistic Engineering Mechanics*, v. 16, n. 3, pp. 219–231, 2001.

[16] YUEN, K.-V., KUOK, S.-C. "Bayesian methods for updating dynamic models", *Applied Mechanics Reviews*, v. 64, n. 1, pp. 010802, 2011.

[17] REYNDERS, E., PINTELON, R., DE ROECK, G. "Uncertainty bounds on modal parameters obtained from stochastic subspace identification", *Mechanical systems and signal processing*, v. 22, n. 4, pp. 948–969, 2008.

[18] MODAK, S., RAWAL, C., KUNDRA, T. "Harmonics elimination algorithm for operational modal analysis using random decrement technique", *Mechanical Systems and Signal Processing*, v. 24, n. 4, pp. 922–944, 2010.

[19] PEETERS, B., CORNELIS, B., JANSSENS, K., et al. "Removing disturbing harmonics in operational modal analysis". In: *Proceedings of International Operational Modal Analysis Conference, Copenhagen, Denmark*, 2007.

[20] QI, K., HE, Z., LI, Z., et al. "Vibration based operational modal analysis of rotor systems", *Measurement*, v. 41, n. 7, pp. 810–816, 2008.

[21] GRES, S., ANDERSEN, P., HOEN, C., et al. "Orthogonal projection-based harmonic signal removal for operational modal analysis". In: *Structural Health Monitoring, Photogrammetry & DIC, Volume 6*, Springer, pp. 9–21, 2019.

[22] REYNDERS, E., MAES, K., LOMBAERT, G., et al. "Uncertainty quantification in operational modal analysis with stochastic subspace identification: validation and applications", *Mechanical Systems and Signal Processing*, v. 66, pp. 13–30, 2016.

[23] PINTELON, R., GUILLAUME, P., SCHOUKENS, J. "Uncertainty calculation in (operational) modal analysis", *Mechanical systems and signal processing*, v. 21, n. 6, pp. 2359–2373, 2007.

[24] ZHANG, L., BRINCKER, R. "An overview of operational modal analysis: major development and issues". In: *1st international operational modal analysis conference*, pp. 179–190. Aalborg Universitet, 2005.

[25] HUNG, C., KO, W. "Identification of modal parameters from measured output data using vector backward autoregressive model", *Journal of Sound and Vibration*, v. 256, n. 2, pp. 249–270, 2002.

[26] KUMARESAN, R., TUFTS, D. "Estimating the parameters of exponentially damped sinusoids and pole-zero modeling in noise", *IEEE Transactions on Acoustics, Speech, and Signal Processing*, v. 30, n. 6, pp. 833–840, 1982.

[27] CLOUD, C. H., MASLEN, E. H., BARRETT, L. E. "Damping ratio estimation techniques for rotordynamic stability measurements", *Journal of Engineering for Gas Turbines and Power*, v. 131, n. 1, pp. 012504, 2009.

[28] HOLOPAINEN, T. P., AATOLA, S. A., CLOUD, C. H., et al. "Comparison of Modal Parameter Estimation Techniques for Electromechanical Rotordynamics of Cage Induction Motors". In: *ASME 2007 International Design Engineering Technical Conferences and Computers and Information in Engineering Conference*, pp. 1215–1224. American Society of Mechanical Engineers, 2007.

[29] NORONHA, R. F. D., MIRANDA, M. A., LUCCHESI-CAVALCA, K., et al. "Stability Testing of CO2 Compressors". In: *Proceedings of the 43rd Turbomachinery Symposium*. Texas A&M University. Turbomachinery Laboratories, 2014.

[30] BAUMANN, U., OTHERS. "Rotordynamic Stability Tests On High-Pressure Radial Compressors." In: *Proceedings of the 28th turbomachinery symposium*. Texas A&M University. Turbomachinery Laboratories, 1999.

[31] MOORE, J. J., WALKER, S. T., KUZDZAL, M. J., et al. "Rotordynamic Stability Measurement During Full-Load, Full-Pressure Testing Of A 6000 Psi Reinjection Centrifugal Compressor." In: *Proceedings of the 31st Turbomachinery Symposium*. Texas A&M University. Turbomachinery Laboratories, 2002.

[32] SOROKES, J. M., SOULAS, T. A., KOCH, J. M., et al. "Full-Scale Aerodynamic And Rotordynamic Testing For Large Centrifugal Compressors." In: *Proceedings of the 38th Turbomachinery Symposium*. Texas A&M University. Turbomachinery Laboratories, 2009.

[33] BIDAUT, Y., BAUMANN, U., AL-HARTHY, S. M. H., et al. "Rotordynamic Stability Of A 9500 Psi Reinjection Centrifugal Compressor Equipped With A Hole Pattern Seal-Measurement Versus Prediction Taking Into Account The Operational Boundary Conditions." In: *Proceedings of the 38th Turbomachinery Symposium*. Texas A&M University. Turbomachinery Laboratories, 2009.

[34] CLOUD, C. H., MASLEN, E. H., BARRETT, L. E. "Damping ratio estimation techniques for rotordynamic stability measurements". In: *ASME Turbo Expo 2008: Power for Land, Sea, and Air*, pp. 1111–1120. American Society of Mechanical Engineers, 2008.

[35] LI, Q., WANG, W., CHEN, L., et al. "Rotor-system log-decrement identification using short-time fourier-transform filter", *International Journal of Rotating Machinery*, v. 2015, 2015.

[36] MESQUITA, A., DIAS, M., MIRANDA, U. "A comparison between the traditional frequency response function (frf) and the directional frequency response function (dfrf) in rotordynamic analysis". In: *First South American congress on computational mechanics, MECOM*, v. 21, 2002.

[37] WANG, W., LI, Q., GAO, J., et al. "An identification method for damping ratio in rotor systems", *Mechanical Systems and Signal Processing*, v. 68, pp. 536–554, 2016.

[38] ZHONG, P. "Rotor-bearing system identification using time domain methods." 1998.

[39] GUGLIELMO, A., MITARITONNA, N., CATANZARO, M., et al. "Full load stability test (FLST) on LNG compressor". In: *ASME Turbo Expo 2014: Turbine Technical Conference and Exposition*, pp. V07AT31A006–V07AT31A006. American Society of Mechanical Engineers, 2014.

[40] CARDEN, E. P., SEHLSTEDT, N., NIELSEN, K. K., et al. "Stability Analysis and Assessment of Rotor Trains Using Operational Modal Analysis". In: *Proceedings of the 9th IFToMM International Conference on Rotor Dynamics*, pp. 2083–2093. Springer, 2015.

[41] OZBEK, M., RIXEN, D. J. "Operational modal analysis of a 2.5 MW wind turbine using optical measurement techniques and strain gauges", *Wind Energy*, v. 16, n. 3, pp. 367–381, 2013.

[42] ALLEN, M. S., SRACIC, M. W., CHAUHAN, S., et al. "Output-only modal analysis of linear time-periodic systems with application to wind turbine simulation data", *Mechanical Systems and Signal Processing*, v. 25, n. 4, pp. 1174–1191, 2011.

[43] CHAUHAN, S., HANSEN, M., TCHERNIAK, D. "Application of operational modal analysis and blind source separation/independent component analysis techniques to wind turbines". In: *Proceedings of XXVII International Modal Analysis Conference, Orlando (FL), USA*, 2009.

[44] DEVRIENDT, C., MAGALHÃES, F., WEIJTJENS, W., et al. "Structural health monitoring of offshore wind turbines using automated operational modal analysis", *Structural Health Monitoring*, v. 13, n. 6, pp. 644–659, 2014.

[45] BRINCKER, R., ANDERSEN, P. "Understanding Stochastic Subspace Identification". In: *Proceedings of the 24th IMAC*, pp. 279–311, St. Louis, Missouri, 2006.

[46] JUANG, J.-N., PHAN, M. "Linear system identification via backward-time observer models", *Journal of guidance, control, and dynamics*, v. 17, n. 3, pp. 505–512, 1994.

[47] HE, M. "Thermoelastohydrodynamic analysis of fluid film journal bearings [Ph. D. thesis]". 2004.

[48] KLEYNHANS, G. F. "A two-control-volume bulk-flow rotordynamic analysis for smooth-rotor/honeycomb-stator gas annular seals [Ph. D. thesis]". 1997.

[49] FRISWELL, M. I. *Dynamics of rotating machines*. Cambridge University Press, 2010.

[50] SILVA, R. T. *Impact of damper seal coefficients uncertainties in rotordynamics*. M. Sc. dissertation, COPPE/UFRJ, Rio de Janeiro, RJ, Brasil, 2018.

[51] KANKI, H. "Solving nonsynchronous vibration problems of large rotating machineries by exciting test in actual operating condition". In: *Proceedings of International Conference on Rotordynamics, JSME, IFToMM, 1986*, pp. 221–225, 1986.

[52] WAGNER, G. B., FOINY, D., SAMPAIO, R., et al. "Operational modal analysis under wind load using stochastic sub-space identification", *Proceedings of DINAME*, 2017.

[53] REYNDERS, E., DE ROECK, G. "Reference-based combined deterministic–stochastic subspace identification for experimental and operational modal analysis", *Mechanical Systems and Signal Processing*, v. 22, n. 3, pp. 617–637, 2008.

[54] ROWELL, D. "State-space representation of LTI systems". http://web.mit.edu/2.14/www/Handouts/StateSpace.pdf, 2002. [Online; accessed 29-Apr-2017].

[55] MEIROVITCH, L. *Principles and techniques of vibrations*, v. 1. New Jersey, Prentice Hall, 1997.

Appendix A

Lateral Analysis: General Description

At design phase, the modeling of lateral behavior of a rotor using Finite Element Model (FEM) is the tool used by the OEM to verify if the rotordynamic project goals were achieved, minimizing risk of unexpected behavior after the equipment is produced.

The standard practice in oil and gas market nowadays, ruled by API 617 [4], is to perform these verifications in three steps:

(i) Undamped Critical Speed Analysis;

(ii) Unbalance Response Analysis;

(iii) Stability Analysis;

The Undamped Critical Speed Analysis is performed by considering a FEM of the rotor, consisting of the shaft, with addition of the inertial effect of elements assembled in the shaft such as sleeves, disks, couplings, dry gas seals and balance drum, known as built-in parts. This analysis considers the assembly of shaft and built-in parts, supported by bearings without damping.

An eigenvalue and eigenvector analysis is done for many values of bearing stiffness, covering a wide range in order to build a Critical Speed Map, as shown in figure A.1. The eigenvalue and eigenvectors problems solved in Undamped Critical Speed Analysis, arises from the undamped, free response equation A.1, in which $\boldsymbol{M}$, $\boldsymbol{K}$ and $\boldsymbol{G}$ are the mass, stiffness and gyroscopic matrices of the system respectively and $\underset{\sim}{z}$ is a vector with the displacement of each degree of freedom from the model.

$$\boldsymbol{M}\ddot{\underset{\sim}{z}} + \boldsymbol{G}\dot{\underset{\sim}{z}} + \boldsymbol{K}\underset{\sim}{z} = 0 \tag{A.1}$$

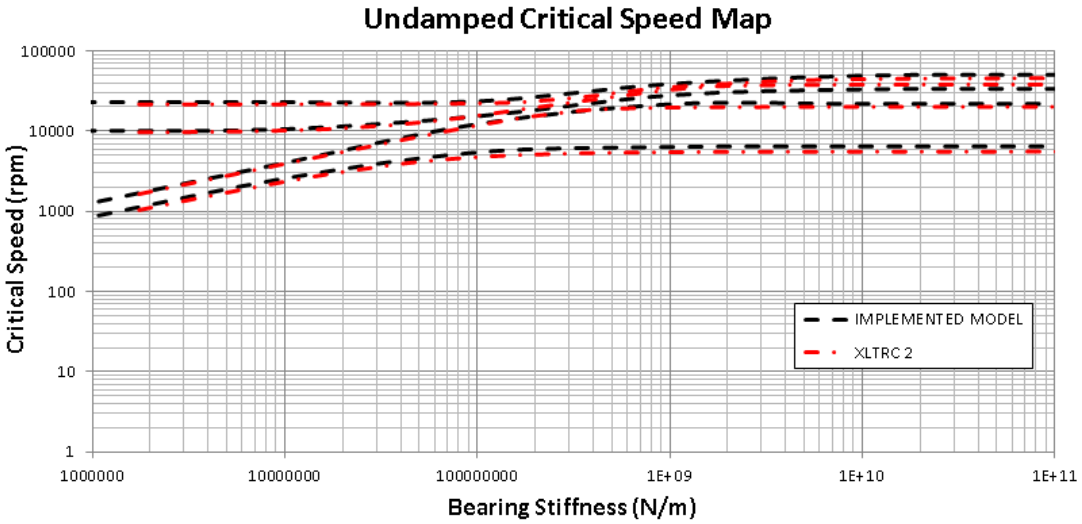

Figure A.1: Undamped Critical Speed Map.

This analysis is used in conceptual design phase, to make a pre-matching between rotor and bearing. After the rotor construction, free-free and rigid support natural frequency can be measured and compared with the predicted soft bearing and rigid bearing natural frequencies, and if necessary, corrections in the shaft FEM model shall be made. Once this analysis relies in the FEM without estimation of bearings and seals rotordynamic coefficients, there are minor uncertainties associated with its results.

In the Unbalance Response Analysis, the FEM of the rotor assembly is considered, adding gyroscopic effect of the shaft and built-in parts. These gyroscopic effect couples the motion equations in vertical and horizontal directions. The bearings are added to the model through their predicted rotordynamics coefficients, including damping and cross coupling stiffness, calculated through codes that performs thermo-elasto-hidrodynamic analysis using the finite element method as proposed by HE [47], or in some cases, through a complete Computational Fluid Dynamics (CFD) analysis solving continuity, Navier-Stokes and Energy equations. Besides the bearings, squeeze film dampers (when applied) and suport stiffness are considered.

Unbalance excitation is then applied in different positions, to excite the first mode, then the second mode and so on, depending on the operational speed and with positions defined by the undamped modeshapes (obtained during the Undamped Critical Speed Analysis). Thus this analysis is done through the solution of the forced response movement equation A.2, in which $\boldsymbol{C}$ is the damping matrix of the system and $\underline{u}$ corresponds to the force vector. Figure A.2 show the result of this analysis to an unbalance placed in a position that aims to excite the first mode, with prediction of displacement in the proximity sensor's location, at Drive-End (DE) and Non Drive End (NDE) bearings. The uncertainties in bearing rotordynamic

coefficients, makes the uncertainties in this analysis higher than those of Undamped Critical Speed Analysis.

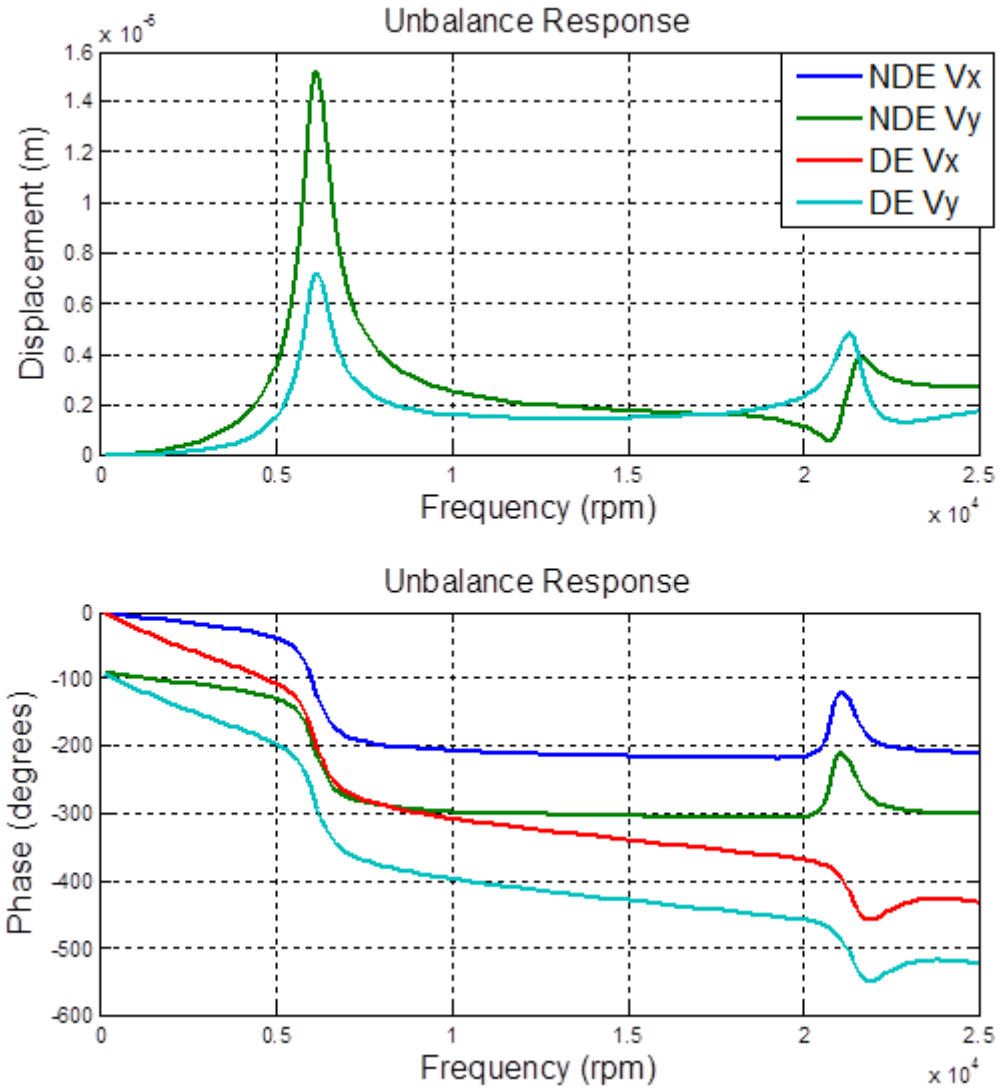

Figure A.2: Unbalance Response Analysis.

To reduce these uncertainties, verifying and updating the model, usually the compressor's purchaser specifies an Unbalance Response Test, performed at the facility of the Original Equipment Manufacturer (OEM) and witnessed by purchaser's inspectors. In this test, an unbalance is added to the rotor (usually at the coupling) and the results are compared to those of the Unbalance Response Analysis, that must contain a case with the unbalance in the same position that in the test.

$$\boldsymbol{M}\ddot{\underset{\sim}{z}} + [\boldsymbol{C} + \boldsymbol{G}]\dot{\underset{\sim}{z}} + \boldsymbol{K}\underset{\sim}{z} = \underset{\sim}{u} \tag{A.2}$$

API 617 [4] standard does not require that the Unbalance Response Analysis considers the rotordynamic effect of gas flowing through the compressor internal components, therefore this analysis is equivalent to a no load operational condition and does not cover relevant changes that can happen in critical speed, due to stiffening effect of high density gas flowing through damper seals.

The Stability analysis is done considering the complete FEM used to perform the Unbalance Response Analysis, with addition of the rotordynamic parameters of labyrinth seals, damper seals, oil seals (when applied) and disks (aerodynamic cross-coupling), solving the free equations of movement (equation A.3), that leads to a damped eigenvalues and eigenvectors problem (using state space formulation for the general case of damping). Most of these parameters vary with gas composition, pressure, temperature and flow and thus many scenarios must be evaluated.

$$\boldsymbol{M}\ddot{\underset{\sim}{z}} + [\boldsymbol{C} + \boldsymbol{G}]\dot{\underset{\sim}{z}} + \boldsymbol{K}\underset{\sim}{z} = \underset{\sim}{0} \tag{A.3}$$

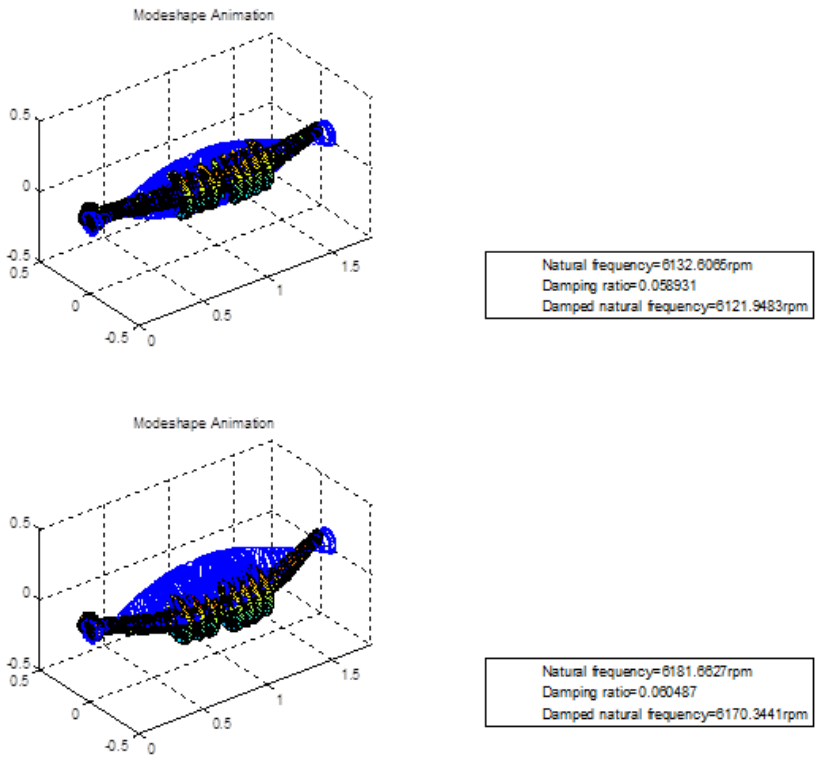

Figure A.3: Stability Analysis: 1^{st} forward and 1^{st} backward modeshapes and eigenvalues.

Besides the stability level, this analysis reveals the changes in critical speed, related to different operational conditions, and can reveal previously the possibility of issues with critical speeds inside the operational range. Figure A.3 shows an example with the 1^{st} forward and backward modeshapes and eigenvalues for an operational condition of a centrifugal compressor. The addition of seals and aerodynamic cross coupling coefficients makes the uncertainties in this analysis higher than those of Unbalance Response Analysis.

Appendix B

Basic Concepts

In this chapter, the basic concepts, necessary prior to understanding the model parameters extraction through Operational Modal Analysis, will be presented.

B.1 Transfer Function

For linear, time invariant systems, the transfer function matrix $\tilde{\boldsymbol{H}}(s)$, defined in Laplace Domain, describes the dynamic of system, allowing computing the outputs of system ($\tilde{\underset{\sim}{Y}}(s)$) once the inputs ($\tilde{\underset{\sim}{U}}(s)$)are known, according to equation B.1.

$$\tilde{\underset{\sim}{Y}}(s) = \tilde{\boldsymbol{H}}(s)\tilde{\underset{\sim}{U}}(s) \tag{B.1}$$

Each element $H_{ij}(s)$ of the transfer function matrix gives the relation between an input at position j and an output at position i, and can be written as per equation B.2. The roots of the numerator $N(s)$ are called "zeros" and the roots of denominator $D(s)$ are called "poles" of the system.

$$H_{ij}(s) = \frac{b_0 + b_1 s + b_2 s^2 ... + b_q s^q}{a_0 + a_1 s + a_2 s^2 ... + a_n s^n} = \frac{N(s)}{D(s)} \tag{B.2}$$

Considering the representation given by equation B.3, the response can be written by equation B.4, where the last term refers to the input poles contribution.

$$H_{ij}(s) = \frac{(s-z_o)(s-z_1)(s-z_2)...(s-z_q)}{(s-p_o)(s-p_1)(s-p_2)...(s-p_q)}K = \frac{R_1}{s-p_1} + \frac{R_2}{s-p_2} + ... + \frac{R_n}{s-p_n} \tag{B.3}$$

$$\tilde{Y}_i(s) = \frac{A_1}{s-p_1} + \frac{A_2}{s-p_2} + ... + \frac{A_n}{s-p_n} + \sum_{in=1}^{l} \frac{A_{in}}{s-p_{in}} \tag{B.4}$$

Applying inverse Laplace transform, to equation B.4, the time domain response is found as in equation B.5.

$$y_i(t) = A_1 e^{p_1 t} + A_2 e^{p_2 t} + ... + A_n e^{p_n t} + \sum_{in=1}^{l} A_{in} e^{p_{in} t} \tag{B.5}$$

Equation B.5 shows that, for stable inputs, systems with at least one pole with real part positive, the response will be instable, while for system with poles that have negative real part, the response is stable. For the case of real part zero, the system oscillates without decaying in response.

B.2 Impulse Response Function

Considering an input with the distribution following a Dirac's $\delta(t)$, where the internal product of any function g(t) with a Dirac's $\delta(t_0)$ follows accordingly with equation B.6, it can be seen from equation B.1 that the response $y_\delta(t)$ to the Dirac's $\delta(t)$ in Laplace domain is equivalent to the transfer function $H(s)$ (equation B.7), once the Laplace transform of Dirac's $\delta(t)$ is equal to one.

$$\begin{array}{l} < g(t), \delta(t - t_0) >= \int_{-\infty}^{+\infty} g(t)\delta(t - t_0)dt = g(t_0) \\ < g(t + t_0), \delta(t) >= \int_{-\infty}^{+\infty} g(t + t_0)\delta(t)dt = g(t_0) \end{array} \tag{B.6}$$

$$H(s) = \tilde{Y}_\delta(s) \tag{B.7}$$

The time domain response $y_\delta(t)$ is known as Impulse Response Function (IRF), and is represented by $h(t)$.

Considering the Dirac's δ property, shown in equation B.6, the input $u(t)$ can be written according to equation B.8.

$$u(t) = \int_{-\infty}^{+\infty} u(\tau)\delta(t - \tau)d\tau \cong \sum_{q=-\infty}^{+\infty} u(\tau_q)\delta(t - \tau_q)\Delta\tau_q \tag{B.8}$$

In the same manner, the system response can be written as the equation B.9.

$$y(t) \cong \sum_{q=-\infty}^{+\infty} u(\tau_q)\Delta\tau_q y_{\delta(t-\tau_q)}(t) \cong \sum_{q=-\infty}^{+\infty} u(\tau_q)h(t - \tau_q)\Delta\tau_q \tag{B.9}$$

Writing the equation B.9 in differential form, equation B.10 is found. This result shows that in time domain, the output of linear, time-invariant systems due to arbitrary excitations, can be found by the convolution between the input and the IRF.

$$y(t) = \int_{-\infty}^{+\infty} u(\tau)h(t - \tau)d\tau = u(t) * h(t) \tag{B.10}$$

Equation B.10 can be written in matrix form, resulting in equation B.11.

$$\underset{\sim}{y}(t) = \boldsymbol{H}(t) * \underline{u}(t) \tag{B.11}$$

Thus, in Laplace domain the system's dynamic is represented by the transfer function matrix $\tilde{\boldsymbol{H}}(s)$ and in time domain, the system's dynamic is represented by the IRF matrix $\boldsymbol{H}(t)$.

B.3 Frequency Response Function

By considering an harmonic input as per equation B.12, the system response in Laplace domain is given by B.13.

$$u(t) = u_o sin(\Omega t) \tag{B.12}$$

$$\tilde{Y}_i(s) = \frac{B_1}{s - p_1} + \frac{B_2}{s - p_2} + ... + \frac{B_n}{s - p_n} + \frac{B_{n+1}}{s - \Omega i} + \frac{B_{n+2}}{s + \Omega i} \tag{B.13}$$

The terms B_{n+1} and B_{n+2} can be calculated through equations B.14 and B.15.

$$B_{n+1} = \lim_{s \to \Omega i} \tilde{Y}_i(s)(s - \Omega i) = H(\Omega i)\frac{u_0}{2i} \tag{B.14}$$

$$B_{n+2} = \lim_{s \to -\Omega i} \tilde{Y}_i(s)(s + \Omega i) = H(-\Omega i)\frac{u_0}{-2i} \tag{B.15}$$

Considering a system with all poles possessing negative real part, for a time $t = T$, high enough, the system will present a steady state response given by B.16.

$$y_{ss}(t) = B_{n+1}e^{\Omega i t} + B_{n+2}e^{-\Omega i t} = u_0 \parallel H(\Omega i) \parallel sin(\Omega t + \phi(\Omega) \tag{B.16}$$

This leads to the definition of Frequency Response Function (FRF), given by $H(\Omega i)$, that have the physical meaning of representing the steady state relation between an output and an harmonic input.

The FRF $H(\Omega i)$ is closely related to the transfer function $H(s)$ and also contains the information about system's dynamic, but in opposition to the transfer function, the FRF can be experimentally observed.

B.4 Continuous State Space Model

The concept of the state of a dynamic system refers to a minimum set of variables, $x_i(t)$, $i = 1 : N$ known as state variables, that fully describe the system and its response to any given set of inputs (ROWELL [54]).

For state determined systems, the knowledgment of state variables at initial time t_0, together with the inputs progression from t_0 to t, is enough to predict the behavior of system in this time interval.

The state space representation, have the general formulation given by equation B.17, where $\underset{\sim}{x}$ is the state vector and $\underset{\sim}{u}$ is the input vector.

$$\dot{\underset{\sim}{x}} = f(\underset{\sim}{x}, \underset{\sim}{u}) \tag{B.17}$$

Describing the state and input variables near an equilibrium point, called operational point, of the evaluated dynamical system, as per equations B.18 and B.19, and expanding $f(\underset{\sim}{x}, \underset{\sim}{u})$ in Taylor series (neglecting the second order terms), leads to the equation B.20. This procedure is a linearization of the dynamical system, near the operational point.

$$\underset{\sim}{x} = \underset{\sim}{x}_{op} + \underset{\sim}{\xi} \tag{B.18}$$

$$\underset{\sim}{u} = \underset{\sim}{u}_{op} + \Delta\underset{\sim}{u} \tag{B.19}$$

$$f(\underset{\sim}{x}, \underset{\sim}{u}) \approx f(\underset{\sim}{x}_{op}, \underset{\sim}{u}_{op}) + \left[\frac{\partial f}{\partial \underset{\sim}{x}}\bigg|_{\underset{\sim}{x}_{op}, \underset{\sim}{u}_{op}}\right]\underset{\sim}{\xi} + \left[\frac{\partial f}{\partial \underset{\sim}{u}}\bigg|_{\underset{\sim}{x}_{op}, \underset{\sim}{u}_{op}}\right]\Delta\underset{\sim}{u} \tag{B.20}$$

Considering equation B.21, adopting a null value to $f(\underset{\sim}{x}_{op}, \underset{\sim}{u}_{op})$, and combining equations B.17, B.20 and B.21 leads to equation B.22, that is the general representation of state space for linear models, where $\boldsymbol{A}$ is known as state matrix and $\boldsymbol{B}$ is known as input matrix.

$$\frac{\partial \underset{\sim}{x}}{\partial t} = \frac{\partial \underset{\sim}{x}_{op}}{\partial t} + \dot{\varepsilon} = \dot{\varepsilon} \tag{B.21}$$

$$\frac{\partial \underset{\sim}{\xi}}{\partial t} = \left[\frac{\partial f}{\partial \underset{\sim}{x}}\bigg|_{\underset{\sim}{x}_{op}, \underset{\sim}{u}_{op}}\right]\underset{\sim}{\xi} + \left[\frac{\partial f}{\partial \underset{\sim}{u}}\bigg|_{\underset{\sim}{x}_{op}, \underset{\sim}{u}_{op}}\right]\Delta\underset{\sim}{u} = \boldsymbol{A}\underset{\sim}{\xi} + \boldsymbol{B}\Delta\underset{\sim}{u} \tag{B.22}$$

It is important to highlight that, there is no unique set of state variables that describe any given system; many different sets of variables may be selected to yield a complete system description. However, for a given system the order (N) is unique (ROWELL [54]).

Regarding a linear rotordynamic system, with general motion equation given by A.2, a suitable definition of states x_1 and x_2 is given by equations B.23.

$$\begin{aligned} \underset{\sim}{x}_1 &= \underset{\sim}{z} \\ \underset{\sim}{x}_2 &= \dot{\underset{\sim}{z}} = \dot{\underset{\sim}{x}}_1 \end{aligned} \tag{B.23}$$

Thus, from A.2 and B.23, the vector $\dot{x}_2$ is given by equation B.24.

$$\dot{\underset{\sim}{x}}_2 = \boldsymbol{M}^{-1}\{\underset{\sim}{u} - [\boldsymbol{C} + \boldsymbol{G}]\dot{\underset{\sim}{z}} - \boldsymbol{K}\underset{\sim}{z}\} \tag{B.24}$$

Defining the state vector according to equation B.25 and combining B.23 and B.24 to write the movement equation using the general representation for linear models, leads to B.26.

$$x = \begin{bmatrix} \underset{\sim}{x}_1 \\ \underset{\sim}{x}_2 \end{bmatrix} \tag{B.25}$$

$$\dot{\underset{\sim}{x}} = \begin{bmatrix} \dot{\underset{\sim}{x}}_1 \\ \dot{\underset{\sim}{x}}_2 \end{bmatrix} = \boldsymbol{A}\underset{\sim}{x} + \boldsymbol{B}\underset{\sim}{u} = \begin{bmatrix} \boldsymbol{0} & \boldsymbol{I} \\ -\boldsymbol{M}^{-1}\boldsymbol{K} & -\boldsymbol{M}^{-1}[\boldsymbol{C} + \boldsymbol{G}] \end{bmatrix} \begin{bmatrix} \underset{\sim}{x}_1 \\ \underset{\sim}{x}_2 \end{bmatrix} + \begin{bmatrix} \boldsymbol{0} \\ \boldsymbol{M}^{-1} \end{bmatrix} \underset{\sim}{u} \tag{B.26}$$

For this system, the order N is equal to $2n$, where n is the amount of degrees of freedom.

It must be taken into account, that the behavior of a general system is seen through observable variables. Thus, defining a vector $\underset{\sim}{y}$ of observable variables, it takes the general form of equation B.27.

$$\underset{\sim}{y} = g(\underset{\sim}{\varepsilon}) \tag{B.27}$$

A rotordynamic system is observed through measurements of displacement, velocity or acceleration. Thus, considering linearity and taking equation B.24 into account, the observable variable vector for a rotordynamic system is given by equation B.28.

$$\underset{\sim}{y} = \mathbb{C}_{\boldsymbol{d}}\underset{\sim}{z} + \mathbb{C}_{\boldsymbol{v}}\dot{\underset{\sim}{z}} + \mathbb{C}_{\boldsymbol{a}}\boldsymbol{M}^{-1}\{\underset{\sim}{u} - [\boldsymbol{C} + \boldsymbol{G}]\dot{\underset{\sim}{z}} - \boldsymbol{K}\underset{\sim}{z}\} \tag{B.28}$$

The matrices $\mathbb{C}_d$, $\mathbb{C}_v$ and $\mathbb{C}_a$, reflects the observation of displacement, velocity and acceleration, respectively. These matrices are formed by zeros, except in the elements of diagonal, at lines corresponding to the observed degrees of freedom.

Rewriting equation B.28 in matrix form leads to B.29.

$$\underset{\sim}{y} = \left[\mathbb{C}_{\boldsymbol{d}} - \mathbb{C}_{\boldsymbol{a}}\boldsymbol{M}^{-1}\boldsymbol{K} \qquad \mathbb{C}_{\boldsymbol{v}} - \mathbb{C}_{\boldsymbol{a}}\boldsymbol{M}^{-1}[\boldsymbol{C} + \boldsymbol{G}]\right]\underset{\sim}{x} + \left[\mathbb{C}_{\boldsymbol{a}}\boldsymbol{M}^{-1}\right]\underset{\sim}{u} = \mathbb{C}\underset{\sim}{x} + \boldsymbol{D}\underset{\sim}{u} \tag{B.29}$$

The equations B.26 and B.29 are the formulation of state space for linear rotor-

dynamic systems.

B.5 Continuous State Space: Free and Forced Response Analysis

Considering free vibration, the state space formulation for linear, time-invariant systems take the form of equation B.30.

$$\begin{aligned} \dot{\underset{\sim}{x}} &= \boldsymbol{A}\underset{\sim}{x} \\ \underset{\sim}{y} &= \mathbb{C}\underset{\sim}{x} \end{aligned} \tag{B.30}$$

Its solution has the exponential form given by equation B.31, leading to the eigenvalues and eigenvectors problem shown in equation B.32.

$$\underset{\sim}{x}(t) = \underset{\sim}{X}e^{\lambda t} \tag{B.31}$$

$$\boldsymbol{A}\underset{\sim}{X} = \lambda\underset{\sim}{X} \tag{B.32}$$

The eigenvalues contain information about the damping, damped natural frequencies and natural frequency, that can be extracted using equations B.33, B.34 and B.35 respectively .

$$\xi_i = \sqrt{\frac{1}{\left(\frac{imag(\lambda_i)}{real(\lambda_i)}\right)^2 + 1}} \tag{B.33}$$

$$\omega_{d_i} = imag(\lambda_i) \tag{B.34}$$

$$\omega_{n_i} = \frac{-real(\lambda_i)}{\xi_i} \tag{B.35}$$

The free response can be written as a linear combination of the eigenvectors, according to equation B.36, where q_i is the modal coordinate responsible to define the influence of mode i^{th}, in the free response.

$$\underset{\sim}{x}(t) = \sum_{i=1}^{2n} \underset{\sim}{X}_i e^{\lambda_i t} q_i \tag{B.36}$$

The modal coordinates assume different values, depending on the initial conditions applied.

Once A is a real, nonsymmetric matrix, the resulting eigenvectors does not have the property of orthogonality in relation to A, but solving the eigenproblem for A^T,

(equation B.37) the so called left eigenvectors arises and the right eigenvectors X and left eigenvectors Y are orthogonal with respect to A, as shown in equation B.38.

$$\boldsymbol{A}^T \underset{\sim}{Y} = \lambda \underset{\sim}{Y} \tag{B.37}$$

$$\underset{\sim}{Y}_i^T \boldsymbol{A} \underset{\sim}{X}_j = 0, \qquad for \qquad \lambda_i \neq \lambda_j \tag{B.38}$$

Considering the eigenvectors normalized according to equations B.39 and B.40, after multiplying both sides of equation B.36 by $\underset{\sim}{Y}_j^T$, we found the values of the modal coordinates as per equation B.41.

$$\underset{\sim}{Y}_i^T \underset{\sim}{X}_i = 1 \tag{B.39}$$

$$\underset{\sim}{Y}_i^T \boldsymbol{A} \underset{\sim}{X}_i = \lambda_i \tag{B.40}$$

$$q_i = \underset{\sim}{Y}_i^T \underset{\sim}{x}(0) \tag{B.41}$$

Thus, the free response to non zero initial conditions is given by B.42, where Λ is a diagonal matrix composed by the λ_i elements.

$$\underset{\sim}{x}(t) = \boldsymbol{X} e^{\boldsymbol{\Lambda} t} \boldsymbol{Y}^T \underset{\sim}{x}(0) = e^{\boldsymbol{A} t} \underset{\sim}{x}(0) \tag{B.42}$$

Regarding forced response, the general solution of the linear, time-invariant, state space model is given by equation B.43 (MEIROVITCH [55]).

$$\underset{\sim}{x}(t) = e^{\boldsymbol{A} t} \underset{\sim}{x}(0) + \int_0^t e^{\boldsymbol{A}(t-\tau)} \boldsymbol{B} \underset{\sim}{u}(\tau)\, \mathrm{d}\tau. \tag{B.43}$$

A detailed demonstration of the equations of present section is given in MEIROVITCH [55].

B.6 Matrix Transfer Function Based on State Space Model

Considering null initial conditions ($\underset{\sim}{x}(0) = 0$), by applying Laplace transform to equations B.26 and B.29, equations B.44 and B.45 are found.

$$s \tilde{\underset{\sim}{X}}(s) = \boldsymbol{A} \tilde{\underset{\sim}{X}}(s) + \boldsymbol{B} \tilde{\underset{\sim}{U}}(s) \tag{B.44}$$

$$\tilde{\underset{\sim}{Y}}(s) = \mathbb{C}\tilde{\underset{\sim}{X}}(s) + \boldsymbol{D}\tilde{\underset{\sim}{U}}(s) \tag{B.45}$$

Combining equations B.44 and B.45, equation B.46 is found.

$$\tilde{\underset{\sim}{Y}}(s) = \mathbb{C}[s\boldsymbol{I} - \boldsymbol{A}]^{-1}\boldsymbol{B}\tilde{\underset{\sim}{U}}(s) + \boldsymbol{D}\tilde{\underset{\sim}{U}}(s) \tag{B.46}$$

From equations B.1 and B.46, the matrix transfer function can be found in terms of the linear, time invariant, continuous state space matrices, as per B.47.

$$\boldsymbol{H}(s) = \mathbb{C}[s\boldsymbol{I} - \boldsymbol{A}]^{-1}\boldsymbol{B} + \boldsymbol{D} \tag{B.47}$$

Once, $[s\boldsymbol{I} - \boldsymbol{A}]^{-1}$ is given by B.48 (where the numerator is given by B.49), the term $det(s\boldsymbol{I} - \boldsymbol{A})$ is present in the denominator of all the matrix transfer function elements. This means that each element of matrix transfer function contains the information of the system's poles.

$$[s\boldsymbol{I} - \boldsymbol{A}]^{-1} = \frac{Coef[s\boldsymbol{I} - \boldsymbol{A}]}{det(s\boldsymbol{I} - \boldsymbol{A})} \tag{B.48}$$

$$Coef(\chi)_{ij} = (-1)^{i+j} det(\chi - excluding\ row_i\ and\ column_j) \tag{B.49}$$

Moreover, by comparing the term $det(s\boldsymbol{I} - \boldsymbol{A})$ with the eigenproblem shown in equation B.32, it is clear that the poles of the matrix transfer function are equal to the eigenvalues found in the Continuous State Space Model.

Expanding $[s\boldsymbol{I} - \boldsymbol{A}]^{-1}$ and performing a spectral decomposition of all powers of A in this expansion, as shown in B.50, allows one to write the matrix transfer function in terms of the eigenvectors and eigenvalues, as per equation B.51.

$$[s\boldsymbol{I}-\boldsymbol{A}]^{-1} = \frac{1}{s}\left\{\boldsymbol{I}+\frac{\boldsymbol{A}}{s}+\frac{\boldsymbol{A}^2}{s^2}+...+\frac{\boldsymbol{A}^k}{s^k}\right\} = \boldsymbol{X}\frac{1}{s}\left\{I+\frac{\boldsymbol{\Lambda}}{s}+\frac{\boldsymbol{\Lambda}^2}{s^2}+...+\frac{\boldsymbol{\Lambda}^k}{s^k}\right\}\boldsymbol{X}^{-1} \tag{B.50}$$

$$\boldsymbol{H}(s) = \mathbb{C}\boldsymbol{X}\begin{bmatrix} \frac{1}{s-\lambda_1} & & \\ & \ddots & \\ & & \frac{1}{s-\lambda_n} \end{bmatrix}\boldsymbol{X}^{-1}\boldsymbol{B} + \boldsymbol{D} \tag{B.51}$$

B.7 Discrete State Space Modeling

Assuming sampling in discrete time ($t = kT$), with sampling time T, the equation B.43 can be rewritten as B.52.

$$\underset{\sim}{x}(kT) = e^{\boldsymbol{A}kT}\underset{\sim}{x}(0) + \int_0^{kT} e^{\boldsymbol{A}(kT-\tau)}\boldsymbol{B}\underset{\sim}{u}(\tau)\,\mathrm{d}\tau. \tag{B.52}$$

Assuming that the time sampling T is small enough to consider that the input $u(t)$ is constant over the time interval from kT to $kT+T$, it can be shown that the state variables at future time, can be described by the equation B.53 (see MEIROVITCH [55] for a detailed description), where the discrete state and input matrix are given by B.54 and B.55.

$$\underset{\sim}{x}(k+1) = \boldsymbol{A_d}\underset{\sim}{x}(k) + \boldsymbol{B_d}\underset{\sim}{u}(k) \tag{B.53}$$

$$\boldsymbol{A_d} = e^{\boldsymbol{A}T} \cong I + T\boldsymbol{A} + \frac{T^2}{2!}\boldsymbol{A}^2 + \frac{T^3}{3!}\boldsymbol{A}^3 + \frac{T^4}{4!}\boldsymbol{A}^4 + ... + \frac{T^n}{n!}\boldsymbol{A}^n \tag{B.54}$$

$$\boldsymbol{B_d} = \boldsymbol{A}^{-1}(e^{\boldsymbol{A}T} - I)\boldsymbol{B} \cong T\left(I + \frac{T}{2!}\boldsymbol{A} + \frac{T^2}{3!}\boldsymbol{A}^2 + ... + \frac{T^{n-1}}{n!}\boldsymbol{A}^{n-1}\right)\boldsymbol{B} \tag{B.55}$$

Combining the discrete state space formulation (B.53), with the observable variables equation B.29, and substituting the discrete state variables and inputs of past times into equation B.53, from the initial time until the present, results in equation B.56, where $\boldsymbol{Y_{m_i}}$ is known as Markov parameters.

$$\underset{\sim}{y}(k) = \sum_{i=1}^{k} \mathbb{C}\boldsymbol{A_d}^{i-1}\boldsymbol{B_d}\underset{\sim}{u}(k-1) = \sum_{i=1}^{k} Y_{m_i}\underset{\sim}{u}(k-1) \tag{B.56}$$

B.8 ARMA and AR models

A common representation model often applied in signal identification is the difference equation known as ARMA model given by B.57, where $u(n)$ is the system input and y(n) is the system response at time nT.

$$y(n) = \sum_{k=1}^{s_1} a_k y(n-k) + \sum_{k=1}^{s_2} b_k u(n-k) + \epsilon \tag{B.57}$$

The coefficients a_k are the auto-regressive (AR) part of model and the coefficients b_k are the moving average part of model (MA).

This equation can be expanded to take into account Multiple-Input and Multiple-Outputs, by replacing the coefficients a_k and b_k by matrices $\boldsymbol{A_k}$ and $\boldsymbol{B_k}$, as per equation B.58.

$$\underset{\sim}{y}(n) = \sum_{k=1}^{s_1} \boldsymbol{A_k}\underset{\sim}{y}(n-k) + \sum_{k=1}^{s_2} \boldsymbol{B_k}\underset{\sim}{u}(n-k) + \epsilon \iff \underset{\sim}{y}(n) - \sum_{k=1}^{s_1} \boldsymbol{A_k}\underset{\sim}{y}(n-k) = \sum_{k=1}^{s_2} \boldsymbol{B_k}\underset{\sim}{u}(n-k) + \epsilon \tag{B.58}$$

The MA part of this equation represents the statistics and the external forces acting on the system, whereas the AR part represents the system's physical properties [1].

Regarding free decays, the MA part of this model can be settled to zero, leading to the auto-regressive model.

By defining the vector $\underset{\sim}{y_d}$ as per equation B.59 and the companion matrix A_c by equation B.60, the AR model can be rewriten by equation B.61, thus the eigenvalues and eigenvectors of companion matrix are the discrete eigenvalues and eigenvectors of the analyzed system (see [1]).

$$\underset{\sim}{y_d} = \begin{bmatrix} \underset{\sim}{y}(n-s+1) \\ \vdots \\ \underset{\sim}{y}(n-1) \\ \underset{\sim}{y}(n) \end{bmatrix} \tag{B.59}$$

$$\boldsymbol{A_c} = \begin{bmatrix} \boldsymbol{0} & \boldsymbol{I} & \boldsymbol{0} & \boldsymbol{0} \\ \vdots & 0 & \ddots & \vdots \\ \boldsymbol{0} & \vdots & & \boldsymbol{I} \\ \boldsymbol{A_s} & \boldsymbol{A_{s-1}} & \cdots & \boldsymbol{A_1} \end{bmatrix} \tag{B.60}$$

$$A_c \underset{\sim}{y_d}(n) = \underset{\sim}{y_d}(n+1) \tag{B.61}$$

To find the AR matrices, a procedure called Poly-Reference Time Domain proposed by VOLD *et al.* [12] starts by forming a Hankel matrix with the free decays response, as per equation B.62 and a block Hankel matrix with only a single block row as per equation B.63, and solving the overdetermined system of equation B.64 by least squares or singular value decomposition, where A is the last row of companion matrix A_c.

$$\boldsymbol{H_1} = \begin{bmatrix} \underset{\sim}{y}(1) & \underset{\sim}{y}(2) & \cdots & \underset{\sim}{y}(N-s) \\ \underset{\sim}{y}(2) & \underset{\sim}{y}(3) & \cdots & \underset{\sim}{y}(N-(s-1)) \\ \vdots & \vdots & \ddots & \vdots \\ \underset{\sim}{y}(s) & \underset{\sim}{y}(s+1) & & \underset{\sim}{y}(N-1) \end{bmatrix} \tag{B.62}$$

$$\boldsymbol{H_2} = \begin{bmatrix} \underset{\sim}{y}(s+1) & \underset{\sim}{y}(s+2) & \cdots & \underset{\sim}{y}(N) \end{bmatrix} \tag{B.63}$$

$$\boldsymbol{AH_1} = \boldsymbol{H_2} \tag{B.64}$$

This allows to build the companion matrix and the eigenproblem of this matrix reveals the modal parameters of the system by the AR method.